First Search for Heavy Neutral Leptons with IceCube DeepCore

Dissertation
zur Erlangung des akademischen Grades
doctor rerum naturalium
(Dr. rer. nat.)

im Fach: Physik
Spezialisierung: Experimentalphysik

eingereicht an der
Mathematisch-Naturwissenschaftlichen Fakultät
der Humboldt-Universität zu Berlin

von
Leander Fischer M. Sc.
geboren am 24. Oktober 1992
in Heidelberg

Präsidentin der Humboldt-Universität zu Berlin
Prof. Dr. Julia von Blumenthal

Dekanin der Mathematisch-Naturwissenschaftlichen Fakultät
Prof. Dr. Caren Tischendorf

Colophon
This document was typeset with the help of KOMA-Script and LaTeX using the open-source kaobook template class.

The source code of this thesis is available at:
https://github.com/LeanderFischer/phd_thesis

Foreword

Before diving into the scientific content of my work, I would like to give some editorial remarks to smoothen the reading experience. Throughout the thesis, acronyms and names of experiments are introduced in *italic font*, the first time they are mentioned, but are used in normal font from then on. The same goes for software packages, which are initially mentioned in SMALL CAPS FONT.

One of the key features of the kaobok template - the big margin - is put to good use to house tables, figures, and additional notes, but also to highlight selected references. Of course, all references are listed in their full extent in the bibliography at the end, but additionally, some (but not necessarily all) of them will be highlighted in the margin next to where they appear to allow for an uninterrupted flow of reading.

For brevity, physical quantities will be given in natural units, but the mathematical derivations will be written out in full detail including $\hbar$ and c.

Abstract

The observation of neutrino oscillations has established that neutrinos have non-zero masses. This phenomenon is not explained by the standard model of particle physics, but one viable explanation to this dilemma is the existence of heavy neutral leptons in the form of right-handed neutrinos. Depending on their mass and coupling to standard model neutrinos, these particles could also play an important role in solving additional unexplained observations such as dark matter and the baryon asymmetry of the universe. This work presents the first search for heavy neutral leptons with the IceCube Neutrino Observatory. The standard three flavor neutrino model is extended by adding a fourth GeV-scale mass state and allowing mixing with the tau neutrino through the mixing parameter $|U_{\tau 4}|^2$. Three heavy neutral lepton mass values, m_4, of 0.3 GeV, 0.6 GeV, and 1.0 GeV are tested using ten years of data, collected between 2011 and 2021, resulting in constraints for the mixing parameter of $|U_{\tau 4}|^2 < 0.19$ ($m_4 = 0.3$ GeV), $|U_{\tau 4}|^2 < 0.36$ ($m_4 = 0.6$ GeV), and $|U_{\tau 4}|^2 < 0.40$ ($m_4 = 1.0$ GeV) at 90 % confidence level. No significant signal of heavy neutral leptons is observed for any of the tested masses. This first analysis lays the fundamental groundwork for future searches for heavy neutral leptons in IceCube.

Zusammenfassung

The observation of neutrino oscillations has established that neutrinos have non-zero masses. This phenomenon is not explained by the *standard model (SM)* of particle physics, but one viable explanation to this dilemma is the existence of *heavy neutral leptons (HNLs)* in the form of right-handed neutrinos. Depending on their mass and coupling to SM neutrinos, these particles could also play an important role in solving additional unexplained observations such as *dark matter (DM)* and the *baryon asymmetry of the universe (BAU)*. This work presents the first search for HNLs with the IceCube Neutrino Observatory. The standard three flavor neutrino model is extended by adding a fourth GeV-scale mass state and allowing mixing with the tau neutrino through the mixing parameter $|U_{\tau 4}|^2$. Three HNL mass values, m_4, of 0.3 GeV, 0.6 GeV, and 1.0 GeV are tested using ten years of data, collected between 2011 and 2021, resulting in constraints for the mixing parameter of $|U_{\tau 4}|^2 < 0.19$ ($m_4 = 0.3$ GeV), $|U_{\tau 4}|^2 < 0.36$ ($m_4 = 0.6$ GeV), and $|U_{\tau 4}|^2 < 0.40$ ($m_4 = 1.0$ GeV) at 90 % confidence level. No significant signal of HNLs is observed for any of the tested masses. This first analysis lays the fundamental groundwork for future searches for HNLs in IceCube.

Contents

1 Introduction

The neutrino was postulated in 1930 by Wolfgang Pauli [1], in order to explain the observed continuous energy spectrum of electrons originating from beta decays. In 1956, Cowan and Reines confirmed this prediction of a neutral, light particle through the measurement of the electron neutrino via the inverse beta decay [2]. With the discovery of the muon neutrino in 1962 [3], and the observation of tau neutrino interactions in 2001 [4], the current three-flavor neutrino picture of the standard model was established. In this description, neutrinos are purely left-handed chiral particles that only interact via the weak force and are predicted to be massless.

[1]: Pauli (1978), "Dear radioactive ladies and gentlemen"

[2]: Cowan et al. (1956), "Detection of the Free Neutrino: a Confirmation"

[3]: Danby et al. (1962), "Observation of High-Energy Neutrino Reactions and the Existence of Two Kinds of Neutrinos"

[4]: Kodama et al. (2001), "Observation of tau neutrino interactions"

[5]: Davis et al. (1968), "Search for Neutrinos from the Sun"

However, experimental observations of neutrino flavor transitions started to appear in the 1960s [5], which can only be explained by the mixing between different neutrino states and the existence of non-zero mass differences. This means that at least two of the three neutrinos must have a non-zero mass. Extending the standard model to describe the three neutrino flavor eigenstates as a superposition of three neutrino mass eigenstates, allows the description of the observed phenomenon of neutrino oscillations. To date, a variety of experiments are observing neutrino oscillations and have measured the neutrino mixing parameters and the mass differences with high precision. But the origin of the neutrino masses remains unknown.

A possible resolution to this problem is the existence of right-handed neutrinos and additional heavy mass states. Through a small mixing with the standard model neutrinos, these could explain the observed neutrino masses and their small magnitude. With masses $\gg$eV they are called heavy neutral leptons and could also play an important role in explaining further problems such as the baryon asymmetry of the universe or serve as dark matter candidates. While they are almost sterile, the small mixing to the standard model neutrinos allows them to participate in weak interactions, which makes experimental searches for these particles possible.

This work presents the first search for heavy neutral leptons using atmospheric neutrinos. The data is collected by the IceCube Neutrino Observatory, which is a cubic-kilometer Cherenkov neutrino detector that was constructed between 2006 and 2010 at the geographic South Pole [6]. It consists of 5160 optical sensors attached to 86 strings, drilled vertically into the Antarctic glacial ice to a maximum depth of ~2500 m. Neutrinos are detected via the Cherenkov light that is emitted by secondary particles produced in neutrino-nucleon scattering interactions in the ice.

[6]: Aartsen et al. (2017), "The IceCube Neutrino Observatory: instrumentation and online systems"

For this search, the standard three flavor neutrino model is extended by adding a fourth GeV-scale mass state and allowing mixing with the third lepton generation through the mixing parameter $|U_{\tau 4}|^2$. The strength of this mixing is tested using atmospheric neutrinos as a source flux. Muon neutrinos that oscillated into tau neutrinos would produce heavy neutral leptons through neutral current interactions, which then decay back to standard model particles. Both production and decay may deposit light in the detector, leading to a unique signature of two cascades at low energies.

A thorough investigation of this unique low-energy double-cascade signature of heavy neutral leptons in IceCube is performed. A benchmark reconstruction performance is estimated using a well established IceCube reconstruction tool, after optimizing it for low-energy double-cascade events. The limitations of the detector to observe these events are identified, and their origins are discussed. Since identifying the low-energy double-cascade signature proved to be very challenging, an analysis is performed by searching for the shape imprint of events from heavy neutral leptons on top of the standard model neutrino sample. The measurement is performed through a binned, maximum likelihood fit, comparing the observed data to the expected events from atmospheric neutrinos and heavy neutral leptons. Three discrete heavy neutral lepton mass values, m_4, of 0.3 GeV, 0.6 GeV, and 1.0 GeV are tested using ten years of data, collected between 2011 and 2021. The fits constrain the mixing parameter to $|U_{\tau 4}|^2 < 0.19$ ($m_4 = 0.3\,\text{GeV}$), $|U_{\tau 4}|^2 < 0.36$ ($m_4 = 0.6\,\text{GeV}$), and $|U_{\tau 4}|^2 < 0.40$ ($m_4 = 1.0\,\text{GeV}$) at 90 % confidence level. No significant signal of heavy neutral leptons is observed for any of the tested masses, and the best fit mixing values obtained are consistent with the null hypothesis of no mixing. This first analysis lays the fundamental groundwork for future searches for heavy neutral leptons in IceCube.

The author was involved in several projects, which are not directly related to the main analysis presented in this thesis. In close collaboration with a former colleague, a novel method to treat detector uncertainty effects in IceCube was developed. It was documented in a few author paper, and is now one of the default methods to incorporate detector uncertainties in atmospheric neutrino analyses in IceCube. This method will also be used in the main analysis of this thesis. Throughout the last years, the author was strongly involved in updating and maintaining the open source analysis framework PISA, which is used in many analyses using the IceCube atmospheric neutrino sample.

This thesis is structured as follows. After introducing the standard model and the extensions to include heavy neutral leptons in Chapter 2, the IceCube Neutrino Observatory and its detection principle are described in Chapter 3. Chapter 4 explains two avenues to simulate the heavy neutral lepton signal in IceCube. A model-independent event generator was developed exclusively by the author, to benchmark the reconstruction performance and cross-check the model-dependent simulation. For the latter, a skeletal structure was constructed by collaborators, before the author took over and implemented the full model-dependent simulation chain, continuously optimizing and testing it, before producing and processing the full samples for the main analysis. Both the study of the performance of IceCube to reconstruct and identify heavy neutral lepton events presented in Chapter 5, and the main analysis discussed in Chapter 6 were developed and performed independently and are original work of the author.

Standard Model Neutrinos and Beyond

2

2.1 The Standard Model

The *standard model (SM)* of particle physics is a Yang-Mills theory [7] providing very accurate predictions of weak, strong, and *electromagnetic (EM)* interactions. It is a relativistic quantum field theory that relies on gauge invariance, where all matter is made up of fermions, which are divided into quarks and leptons. Bosons describe the interactions between the fermions that have to fulfil the overall symmetry of the theory.

[7]: Yang et al. (1954), "Conservation of Isotopic Spin and Isotopic Gauge Invariance"

The initial idea of the theory is associated with the works of Weinberg [8], Glashow [9], and Salam [10], that proposed a unified description of EM and weak interactions as a theory of a spontaneously broken SU(2) x U(1) symmetry for leptons, predicting a neutral massive vector boson Z^0, a massive charged vector boson $W^{\pm}$, and a massless photon γ as the gauge bosons. The Higgs mechanism [11], describing the breaking of the symmetry, predicts the existence of an additional scalar particle, the Higgs boson, giving the $W^{\pm}$ and Z^0 bosons their mass. The Higgs boson was discovered in 2012 at the LHC [12, 13].

[8]: Weinberg (1967), "A Model of Leptons"
[9]: Glashow (1961), "Partial-symmetries of weak interactions"

[11]: Higgs (1964), "Broken symmetries, massless particles and gauge fields"

Gell-Mann and Zweig proposed the quark model in 1964 [14, 15], which was completed by the discovery of non-abelian gauge theories [16] to form the SU(3) symmetry of the strong interaction called *quantum chromodynamics (QCD)*. QCD describes the interaction between quarks and gluons which completed the full picture of the SM in the mid-1970s. Together with the electroweak theory, the SM is a $SU(3)_C$ x $SU(2)_L$ x $U(1)_Y$ local gauge symmetry, with the conserved quantities *color* (C), *left-handed chirality* (L), and *weak hypercharge* (Y).

[14]: Gell-Mann (1964), "A Schematic Model of Baryons and Mesons"
[15]: Zweig (1964), "An SU(3) model for strong interaction symmetry and its breaking. Version 2"

In the following, the basic properties of neutrinos in the SM are described, following the derivations of [17, 18].

[17]: Giunti et al. (2007), *Fundamentals of Neutrino Physics and Astrophysics*
[18]: Schwartz (2013), *Quantum Field Theory and the Standard Model*

2.1.1 Fundamental Fields

Fermions in the SM are Weyl fields with either *left-handed (LH)* or *right-handed (RH)* chirality, meaning they are eigenvectors of the chirality operator γ_5 with $\gamma_5 \psi_{R/L} = \pm \psi_{R/L}$. Only LH particles transform under $SU(2)_L$. The Higgs field is a complex scalar field, a doublet of $SU(2)_L$, which is responsible for the spontaneous symmetry breaking of $SU(2)_L$ x $U(1)_Y$ to $U(1)_{EM}$. Local gauge transformations of the fields are given by

$$\psi \rightarrow e^{ig\theta^a(x)T^a}\psi \,, \tag{2.1}$$

where g is the coupling constant, $\theta^a(x)$ are the parameters of the transformation, and T^a are the generators of the group, with a counting them. The number of bosons is dependent on the generators of the symmetry groups, while the strength is defined by the coupling constants. There are eight massless gluons corresponding to the generators of the $SU(3)_C$ group. These mediate the strong force which conserves color charge. The W_1, W_2, W_3, and

B boson fields of the SU(2)$_L$ x U(1)$_Y$ group are mixed into the massive bosons through spontaneous symmetry breaking as

$$W^{\pm} = \frac{1}{\sqrt{2}}(W_1 \mp iW_2) \tag{2.2}$$

and

$$Z^0 = \cos\theta_W W_3 - \sin\theta_W B \ , \tag{2.3}$$

with θ_W being the *Weinberg angle*. The massless photon field is given by

$$A = \sin\theta_W W_3 + \cos\theta_W B \tag{2.4}$$

and its conserved quantity is the EM charge Q, which depends on the weak hypercharge, Y, and the third component of the weak isospin, T_3, as $Q = T_3 + Y/2$.

	Type			Q
quarks	u	c	t	+2/3
	d	s	b	-1/3
leptons	ν_e	ν_μ	ν_τ	0
	e	μ	τ	-1

Table 2.1: Fermions in the Standard Model. Shown are all three generations of quarks and leptons with their electric charge Q.

Fermions are divided into six quarks and six leptons, which are listed in Table 2.1. The quarks interact vie the weak, the strong, and the EM force, and they are always found in bound form as baryons or mesons. Leptons do not participate in the strong interaction and only the electrically charged leptons are massive and are effected by the EM force, while neutrinos only interact via the weak force and are predicted to be massless in this original form of the SM. Each charged lepton has an associated neutrino, which it interacts with in charged-current weak interactions, that will be explained in more detail in Section 2.1.4. For the massive fermion a LH and a RH component exist (e_L, e_R), while the neutrinos only have a LH component (ν_{eL}). Both LH fields of one generation form a doublet under SU(2)$_L$, $L_L = (\nu_{eL}, e_L)^T$, while the RH fields are singlets under SU(2)$_L$, e_R.

2.1.2 Electroweak Symmetry Breaking

To elaborate the process of spontaneous symmetry breaking through which the gauge bosons of the weak interaction acquire their masses, the Lagrangian of the Higgs field is considered as

$$\mathcal{L}_{\text{Higgs}} = (D_\mu \Phi^\dagger)(D^\mu \Phi) - \lambda\left(\Phi^\dagger\Phi - \frac{v^2}{2}\right)^2 \ , \tag{2.5}$$

with parameters λ and v, where λ is assumed to be positive. Φ is the Higgs doublet, which is defined as

$$\Phi = \begin{pmatrix} \Phi^+ \\ \Phi^0 \end{pmatrix} \ , \tag{2.6}$$

with the charged component Φ^+ and the neutral component Φ^0. The covariant derivative is given by

$$D_\mu = \partial_\mu - ig_2\frac{\sigma^i}{2}W_\mu^i - \frac{1}{2}ig_1 B_\mu \ , \tag{2.7}$$

with the Pauli matrices σ^i and the gauge boson fields W_μ^i and B_μ of the SU(2)$_L$ and U(1)$_Y$ groups, respectively. The coupling constants g_2 and g_1 are the respective coupling constants which are related to the Weinberg angle as $\tan\theta_W = \frac{g_1}{g_2}$. The Higgs potential has a non-zero *vacuum expectation value*

(vev) at the minimum of the potential at $\Phi^\dagger\Phi = \frac{v^2}{2}$. Since the vacuum is electrically neutral, it can only come from a neutral component of the Higgs doublet as

$$\Phi_{\text{vev}} = \frac{1}{\sqrt{2}}\begin{pmatrix}0\\ v\end{pmatrix}. \tag{2.8}$$

2.1.3 Fermion Masses

The mass term for charged fermions with spin-1/2 is given by

$$\mathscr{L}_{\text{Dirac}} = m(\bar{\Psi}_R\Psi_L - \bar{\Psi}_L\Psi_R)\,, \tag{2.9}$$

composed of the product of LH and RH Weyl spinors $\Psi_{L/R}$. This term is not invariant under SU(2)$_L$ x U(1)$_Y$ gauge transformations, but adding a Yukawa term

$$\mathscr{L}_{\text{Yukawa}} = -Y^e\bar{L}_L\Phi e_R + h.c.\,, \tag{2.10}$$

coupling the fermion fields, e_R, to the Higgs field, Φ, recovers the invariance and gives the fermions their masses. Here, Y^e is the Yukawa coupling constant and $\bar{L}_L$ is the SU(2)$_L$ doublet. With the vev, this results in the mass term for the charged leptons and down-type quarks of the form $-m_e(\bar{e}_L e_R + \bar{e}_R e_L)$ with $m_e = \frac{Y^e v}{\sqrt{2}}$. With $\tilde{\Phi} = i\sigma_2\Phi^*$, a similar Yukawa term can be written as $-Y^u\bar{L}_L\tilde{\Phi}u_R + h.c.$, which leads to the masses of the up-type quark fields u_R.

2.1.4 Leptonic Weak Interactions after Symmetry Breaking

After the spontaneous symmetry breaking, the leptonic part of the electroweak Lagrangian can be written as

$$\begin{aligned}\mathscr{L}^{\ell}_{\text{EW}} = {}& \frac{g}{\sqrt{2}}W^+\sum_{\alpha=e,\mu,\tau}\bar{\nu}_\alpha\gamma^\mu P_L\ell_\alpha + \frac{g}{4c_w}Z \\ & \times\left\{\sum_{\alpha=e,\mu,\tau}\bar{\nu}_\alpha\gamma^\mu P_L\nu_\alpha + \sum_\alpha\bar{\ell}_\alpha\gamma^\mu\left[2s_w^2P_R - (1-2s_w^2)P_L\right]\ell_\alpha\right\} + h.c.\,,\end{aligned} \tag{2.11}$$

where $c_w \equiv \cos\theta_w$, $s_w \equiv \sin\theta_w$, P_L and P_R are the left and right projectors, respectively, while ν_α and ℓ_α, are the neutrino and charged lepton weak eigenstates. The W^+ and Z^0 bosons are the massive gauge bosons of the weak interaction. The large boson masses $m_W \sim 80\,\text{GeV}$ and $m_Z \sim 90\,\text{GeV}$ result in a short range of the force of about 1×10^{-18} m. Interactions carried out by the $W^\pm$ bosons are called *charged current (CC)* interactions, as they propagate a charge, therefore changing the interacting lepton to its charged/neutral counterpart. *Neutral current (NC)* interactions are those mediated by the Z^0 boson, where no charge is transferred. NC interactions couple neutrinos to neutrinos and charged leptons to charged leptons, but not to each other. The Feynman diagrams for CC and NC interactions are shown in Figure 2.1.

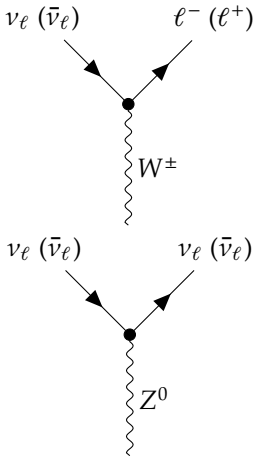

Figure 2.1: Feynman diagrams of charged-current (top) and neutral-current (bottom) neutrino/antineutrino weak interactions, modified from [19].

2.2 Beyond the Standard Model

The fundamentals of the SM described above **are not** enough to explain all observed phenomena. The SM is unable to account for gravity, as it

is incompatible with general relativity. Similarly, it fails to explain some cosmological observations like *dark matter (DM)*, and the matter-antimatter asymmetry in the universe. But most importantly, the SM does not predict neutrinos to have mass, which on the contrary is experimentally proven by to observation of neutrino oscillations, so some extension to the SM is needed to complete the full picture.

The standard cosmological model ΛCDM [20], includes a non-baryonic matter species referred to as *cold dark matter (CDM)* that is responsible for the observed large-scale structure of the universe and accounts for 84.4 % of the total matter density in the universe [21]. Despite its effects being observed at several cosmological scales, from the size of small galaxies [22] to the size of galaxy clusters [23], the nature of CDM is still unknown.

[20]: Deruelle et al. (2018), *Relativity in Modern Physics*

[21]: Workman et al. (2022), "Review of Particle Physics"

[22]: Simon (2019), "The Faintest Dwarf Galaxies"

[23]: Allen et al. (2011), "Cosmological Parameters from Observations of Galaxy Clusters"

ΛCDM also assumes that equal amounts of matter and anti-matter were produced in the early universe. However, the universe today is dominantly made up of matter. This *baryon asymmetry of the universe (BAU)* can be measured by the difference between the number densities of baryons and anti-baryons normalized to the number density of photons as

$$\eta_B = \frac{n_B - n_{\bar{B}}}{n_\gamma} \,, \tag{2.12}$$

where n_B, $n_{\bar{B}}$, and n_γ are the number densities of baryons, anti-baryons, and photons, respectively. Baryons are the dominant component with η_B being observed to be at the order of 10^{-9} [21]. Leptogenesis and EW baryogenesis are scenarios that could explain this phenomenon, where the former could be realized by the existence of heavy RH neutrinos [24].

[24]: Fukugita et al. (1986), "Barygenesis without grand unification"

The observation of neutrino flavor conversions and neutrino oscillations in a multitude of experiments [5, 25, 26] is the strongest evidence for physics *beyond the standard model (BSM)* measured in laboratories to date. The observation that neutrinos change their flavor while they propagate through space can only be explained, if at least two neutrinos have a non-zero mass. From those measurements we know the mass differences are very small as compared to the lepton masses, but neither their existence, nor their smallness is predicted by the SM. There are upper limits on the sum of all neutrino masses from cosmological observations at 1.2 eV [27] [28] and at 0.8 eV from the KATRIN experiment [29]. Adding RH neutrino states to the theory could explain the origin of the observed non-zero neutrino masses and could be tested for by searching for corresponding signatures in experiments.

[5]: Davis et al. (1968), "Search for Neutrinos from the Sun"

[25]: Fukuda et al. (1998), "Evidence for Oscillation of Atmospheric Neutrinos"

[26]: Ahmad et al. (2002), "Direct Evidence for Neutrino Flavor Transformation from Neutral-Current Interactions in the Sudbury Neutrino Observatory"

[28]: Aghanim et al. (2020), "Planck2018 results: VI. Cosmological parameters"

[29]: Aker et al. (2022), "Direct neutrino-mass measurement with sub-electronvolt sensitivity"

2.2.1 Mass Mechanisms

Since there are no RH neutrinos in the SM, the mass mechanism described in Section 2.1.3, which couples the Higgs field to the combination of LH and RH Weyl fields, predicts the LH neutrinos to be massless. From experimental observations it is known that at least two of the three neutrino generations need to have a non-zero mass. Assuming the existence of RH neutrinos fields, ν_R, one way of producing the neutrino masses is by adding a Yukawa coupling term similar to the one for up-type quarks mentioned in Section 2.1.3, to write the full Yukawa Lagrangian as

$$\mathscr{L}_{\text{Yukawa}} = -Y^e_{ij} \bar{L}^i_L \Phi e^j_R - Y^\nu_{ij} \bar{L}^i_L \tilde{\Phi} \nu^j_R + h.c. \,, \tag{2.13}$$

with indices i, j running over the three generations of leptons, e, μ, and τ, and Y^e and Y^ν being the Yukawa coupling matrices. Diagonalizing the Yukawa coupling matrices through unitary transformations U^e and U^ν leads to the **Dirac mass term** in the mass basis as

$$\mathscr{L}^{\text{mass}}_{\text{Dirac}} = \frac{v}{\sqrt{2}} \left(\bar{e}_L M_e e_R - \bar{\nu}_L M_\nu \nu_R \right) \ , \tag{2.14}$$

where M_e and M_ν are the diagonal mass matrices of leptons and neutrinos, respectively. A purely Dirac mass term would not explain the smallness of the neutrino masses in a straightforward way. Only fine-tuning the Yukawa coupling constants to small values would lead to small neutrino masses.

An additional way of generating neutrino masses is by adding a Majorana mass term of the form

$$\mathscr{L}_{\text{Majorana}} = -\frac{1}{2} M_{ij} (\nu_R^i)^c \nu_R^j + h.c. \ , \tag{2.15}$$

with M_{ij} being the Majorana mass matrix and the indices i, j running over all n_R RH neutrino generations. The superscript c denotes the charge conjugate field. Combining the charge conjugated RH neutrino fields with the LH neutrino fields as

$$\boldsymbol{N} = \begin{pmatrix} \boldsymbol{\nu}_L \\ \boldsymbol{\nu}_R^c \end{pmatrix} , \tag{2.16}$$

with $\boldsymbol{\nu}_R$ containing the n_R RH fields. The full neutrino mass Lagrangian is then given by the combined **Dirac and Majorana mass term** as

$$\mathscr{L}^{\text{mass},\nu}_{\text{Dirac+Majorana}} = \frac{1}{2} \boldsymbol{N}^T \hat{C} M^{\text{D+M}} \boldsymbol{N} + h.c. \ , \tag{2.17}$$

and the mass matrix is given by

$$M^{\text{D+M}} = \begin{pmatrix} 0 & (M^D)^T \\ M^D & M^R \end{pmatrix} . \tag{2.18}$$

On top of explaining the origin of neutrino masses itself, a combined Dirac and Majorana mass term could also solve the question of their smallness. If the mass of the RH neutrinos is very large, the masses of the active neutrino flavors are suppressed, which is known as *see-saw mechanism*.

Depending on the neutrino mass generation mechanism, they are either Dirac or Majorana particles. In the Dirac case, the mass Lagrangian *conserves lepton number (LNC)*, while in the Majorana case, the mass Lagrangian *violates lepton number (LNV)* by two units. Majorana neutrinos satisfy the condition $\nu = \nu^c = \mathscr{C} \bar{\nu}^T$, where $\mathscr{C}$ is the charge conjugation operator. They are effectively indistinguishable from their antiparticles. Whether neutrinos are Majorana or Dirac particles another unsolved question in the neutrino sector.

2.2.2 Minimal Extensions and the νMSM

So far we have described neutrinos in their flavor eigenstates, which are relevant for weak interactions, where the three weak flavor states ν_e, ν_μ, and ν_τ are related to the charged leptons they interact with in CC interactions. In order to *just* explain the three oscillating flavor eigenstates, three mass states are needed, which are related to the flavor eigenstates by the unitary,

3x3 *Pontecorvo-Maki-Nakagawa-Sakata (PMNS)* mixing matrix U, where the flavor states are a superposition of the mass states as

$$|\nu_\alpha\rangle = \sum_k U^*_{\alpha k} |\nu_k\rangle \ , \tag{2.19}$$

with the weak flavor states $|\nu_\alpha\rangle$, $\alpha = e, \mu, \tau$, and the mass states $|\nu_k\rangle$ with $k = 1, 2, 3$. In its generic form the PMNS matrix is given by

$$U = \begin{pmatrix} U_{e1} & U_{e2} & U_{e3} \\ U_{\mu 1} & U_{\mu 2} & U_{\mu 3} \\ U_{\tau 1} & U_{\tau 2} & U_{\tau 3} \end{pmatrix} , \tag{2.20}$$

which will be the basis for the discussion of neutrino oscillations in Section 2.3.2.

However, this is not enough to explain the neutrino masses observed in oscillation experiments. The most minimal model required to give rise to two non-zero active neutrino masses, is an additional two RH neutrinos, assuming the mass of the lightest SM neutrino is zero. If the additional neutrino states have masses $\gg$eV they are referred to as *heavy neutral leptons (HNLs)*, which are almost sterile, with a small mass mixing with the active neutrinos.

[30]: Asaka et al. (2005), "The nuMSM, dark matter and neutrino masses"
[31]: Asaka et al. (2005), "The νMSM, dark matter and baryon asymmetry of the universe"

But the SM also fails to explain additional observations of physics beyond the standard model (BAU, DM), which could be solved by the *neutrino minimal standard model (νMSM)* [30, 31]. In the νMSM, three RH neutrinos are added, where two of them are heavy, to explain the observed neutrino masses and oscillations, and a third one is light and serves as a DM candidate. The DM production occurs in this model through a mixing between the sterile state and the active neutrinos, with a large lepton asymmetry, while the BAU is generated through processes that do not conserve the fermion number [32, 33]. The mixing between mass and flavor eigenstates is then described by an extended 6x6 mixing matrix as

[32]: Rubakov et al. (1996), "Electroweak baryon number nonconservation in the early universe and in high-energy collisions"
[33]: Canetti et al. (2013), "Sterile Neutrinos as the Origin of Dark and Baryonic Matter"

$$\begin{pmatrix} \nu_e \\ \nu_\mu \\ \nu_\tau \\ N_1 \\ N_2 \\ N_3 \end{pmatrix} = \begin{pmatrix} U_{e1} & U_{e2} & U_{e3} & U_{e4} & U_{e5} & U_{e6} \\ U_{\mu 1} & U_{\mu 2} & U_{\mu 3} & U_{\mu 4} & U_{\mu 5} & U_{\mu 6} \\ U_{\tau 1} & U_{\tau 2} & U_{\tau 3} & U_{\tau 4} & U_{\tau 5} & U_{\tau 6} \\ U_{N_1 1} & U_{N_1 2} & U_{N_1 3} & U_{N_1 4} & U_{N_1 5} & U_{N_1 6} \\ U_{N_2 1} & U_{N_2 2} & U_{N_2 3} & U_{N_2 4} & U_{N_2 5} & U_{N_2 6} \\ U_{N_3 1} & U_{N_3 2} & U_{N_3 3} & U_{N_3 4} & U_{N_3 5} & U_{N_3 6} \end{pmatrix} \begin{pmatrix} \nu_1 \\ \nu_2 \\ \nu_3 \\ \nu_4 \\ \nu_5 \\ \nu_6 \end{pmatrix} , \tag{2.21}$$

where N_i and ν_{i+3} ($i \in 1, 2, 3$) are the sterile flavor states and the additional RH mass states, respectively. In the νMSM, the two heavy RH neutrinos generate the active neutrino masses through the type I seesaw mechanism [34–38]. This refers to a model, where the HNLs are assumed to be SM scalars and get their mass trough coupling to the Higgs as in Section 2.2.1. Naturally, more complex theories also exist, but are beyond the scope of this thesis and will not be discussed further.

[34]: Minkowski (1977), "$\mu \to e\ \gamma$ at a rate of one out of 10^9 muon decays?"
[35]: Yanagida (1980), "Horizontal Symmetry and Masses of Neutrinos"
[36]: Glashow (1980), "The Future of Elementary Particle Physics"
[37]: Gell-Mann et al. (1979), "Complex Spinors and Unified Theories"
[38]: Mohapatra et al. (1980), "Neutrino Mass and Spontaneous Parity Nonconservation"

With this extension, the leptonic part of the EW Lagrangian from Equation

2.11 now reads

$$\mathscr{L}^{\ell}_{\text{ext.EW}} = \frac{g}{\sqrt{2}} W^{+} \sum_{\alpha} \sum_{i} U^{*}_{\alpha i} \bar{\nu}_i \gamma^{\mu} P_L \ell_{\alpha} + \frac{g}{4 c_w} Z \times \left\{ \sum_{i,j} C_{ij} \bar{\nu}_i \gamma^{\mu} P_L \nu_j + \sum_{\alpha} \bar{\ell}_{\alpha} \gamma^{\mu} \left[2 s_w^2 P_R - (1 - 2 s_w^2) P_L \right] \ell_{\alpha} \right\} + h.c. \,, \tag{2.22}$$

with

$$C_{ij} \equiv \sum_{\alpha} U^{*}_{\alpha i} U_{\alpha j} \,, \tag{2.23}$$

and the indices α and i now summing over all $(3 + n)$ flavor and mass states, respectively. If only mixing between one SM flavor, α, and one RH neutrino mass state, i, is non-zero $C_{ii} = |U_{\alpha i}|^2 \neq 0$, coupling terms of the form

$$\mathscr{L}^{\ell}_{\text{ext.EW}} \supset \frac{g}{\sqrt{2}} W^{+} |U_{\alpha i}|^2 \bar{\nu}_i \gamma^{\mu} P_L \ell_{\alpha} \,, \tag{2.24}$$

and

$$\mathscr{L}^{\ell}_{\text{ext.EW}} \supset \frac{g}{4 c_w} Z |U_{\alpha i}|^2 \bar{\nu}_i \gamma^{\mu} P_L \nu_i + h.c. \,, \tag{2.25}$$

are present. Those are the CC and NC interactions between the HNL and the SM neutrinos, which are the basis for the searches for HNLs in experiments, as will be discussed in the following.

2.2.3 Observational Avenues for Right-Handed Neutrinos

If the RH neutrinos have masses at the eV scale, they can be observed through distortion effects in measurements of neutrino oscillation experiments. Several analyses looking for these so-called light sterile neutrinos exist in *IceCube*, where [39] is using atmospheric neutrinos in the higher energy range of 500 GeV to 10 000 GeV and [19] is using the lower energy region of 6 GeV to 156 GeV. The latter work includes a detailed description of the expected oscillation effects and the various anomalies observed in oscillation experiments that could be explained by the existence of a light sterile neutrino, which is not covered in this work.

[39]: Aartsen et al. (2020), "eV-Scale Sterile Neutrino Search Using Eight Years of Atmospheric Muon Neutrino Data from the IceCube Neutrino Observatory"

[19]: Trettin (2023), "Search for eV-scale sterile neutrinos with IceCube DeepCore"

Here, the focus will be on heavy RH neutrinos, interchangeably also called heavy sterile neutrinos, or HNLs. A defining property is that they are too massive to be produced in oscillations and to be observed as distortions thereof. Several ways to observe HNLs are possible through direct production and decay experiments. Most of the existing searches assume the minimal model, where only one coupling between the new mass states and the SM neutrinos is non-zero, and the coupling is just through mass mixing in a type I seesaw scenario, but more complex scenarios are of course also possible and might produce various additional signatures.

In general, the constraints discussed in the following are based on models, where only the coupling between the HNL and one SM flavor is non-zero. While this is the straight forward approach to test the mixing parameters individually, this might make the constraints stronger than they would be in a more complex scenario, where the HNLs couple to more than one SM flavor as was shown in [40] for collider bounds.

[40]: Tastet et al. (2021), "Reinterpreting the ATLAS bounds on heavy neutral leptons in a realistic neutrino oscillation model"

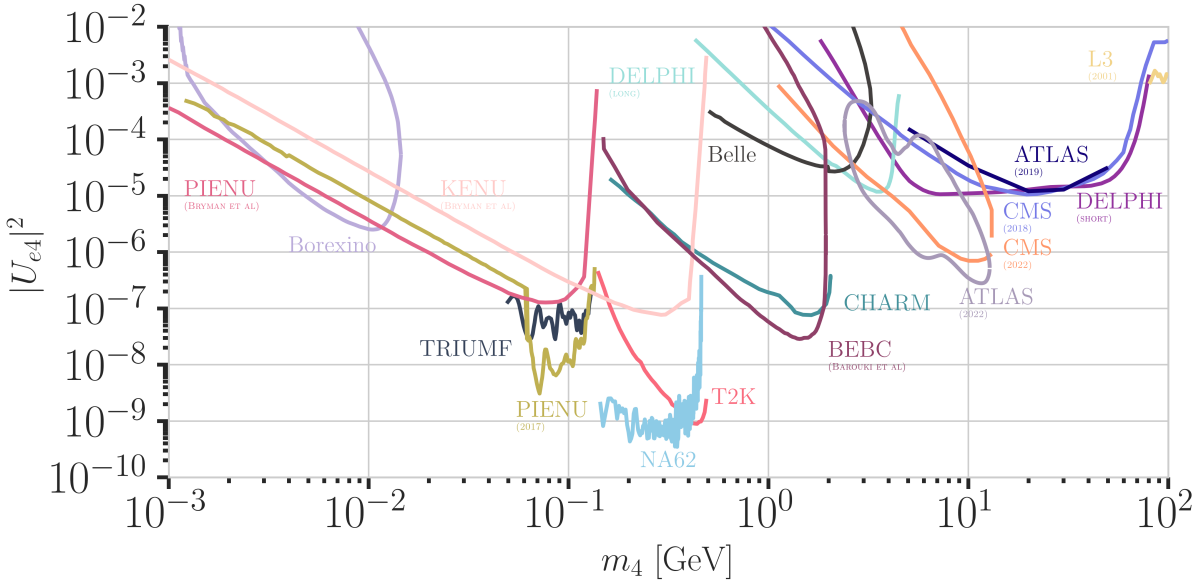

Figure 2.2: Current leading $|U_{e4}|^2 - m_4$ upper limits from PIENU [41, 42], BOREXINO [43], KENU [41], TRIUMF [44], NA62 [45], T2K [46], DELPHI [47], BEBC [48], Belle [49], L3 [50], CHARM [51], ATLAS [52, 53], CMS [54, 55], and NuTeV [56]. Modified from [57].

Extracted Beamline Searches

Protons interacting with a target or a beam dump can produce pions, kaons, and heavy-quark hadrons, whose subsequent decays would also produce HNLs. Depending on the HNL lifetime in the specific model, the mass of the HNLs produced in beam dump experiments would be between 1 MeV and 4 GeV and they could decay at distances across several orders of magnitude. Experiments along the extracted beamline, which are using a spectrometer with particle identification, can search for unique decay signatures at displaced vertices. Example signatures[1] are $\nu_4 \to l_\alpha \pi^+$, $\nu_4 \to \nu_\alpha l_\beta^+ l_\beta^-$, or $\nu_4 \to \nu_\alpha \pi^0$ (or other neutral mesons) that cannot be explained by SM neutrinos. Here, ν_α and l_α are the SM neutrino and charged lepton of flavor $\alpha \in \{e, \mu, \tau\}$, which is defined by the allowed HNL coupling. l_β^- / l_β^+ is a charged lepton/antilepton pair of any flavor $\beta \in \{e, \mu, \tau\}$. Depending on the decay channel, a specific mixing can be probed. The other way of searching for HNLs with these interactions is to look for peaks in the missing mass spectrum, measured around the production vertex at the target, which is usually not possible for beam dumps, as the beam dump region is not calorimetrically instrumented. The HNL searches were pioneered by experiments at extracted beamlines, with *PS191* [58] and *CHARM* [51] establishing upper limits on $|U_{e4}|^2$, $|U_{\mu 4}|^2$, and combinations of them, at masses from 10 MeV to 500 MeV at orders of 10^{-3} to 10^{-6}. Since then, there has been a large activity of searches for HNLs at extracted beamlines and at the lower mass end, the strongest bounds on $|U_{e4}|^2$ are set by *PIENU* [41] at $\sim 10^{-4}$ around 2 MeV, and at the higher mass end, the strongest bounds are set by *NA62* [45], reaching down to $\sim 10^{-9}$ at 0.3 GeV. For $|U_{\mu 4}|^2$, the strongest bounds up to 10 GeV are set by *PSI* [59] at $\sim 10^{-5}$, and reach down to $\sim 10^{-9}$ at 0.3 GeV, by *BNL-E949* [60]. The current strongest bounds on $|U_{e4}|^2$ and $|U_{\mu 4}|^2$ are shown in Figure 2.2 and Figure 2.3, where bounds from other type of experiments are also presented. Those will be discussed in the following.

1: The explicit channels and their decay width calculations used in this thesis are explained in detail in Section 4.2.1.

[58]: Bernardi et al. (1986), "Search for Neutrino Decay"

[51]: Bergsma et al. (1983), "A Search for Decays of Heavy Neutrinos"

[41]: Bryman et al. (2019), "Constraints on Sterile Neutrinos in the MeV to GeV Mass Range"

[45]: Parkinson et al. (2022), "Search for heavy neutral lepton production at the NA62 experiment"

[59]: Daum et al. (1987), "Search for Admixtures of Massive Neutrinos in the Decay $\pi^+ \to \mu^+$ Neutrino"

[60]: Artamonov et al. (2015), "Search for heavy neutrinos in $K^+ \to \mu^+ \nu_H$ decays"

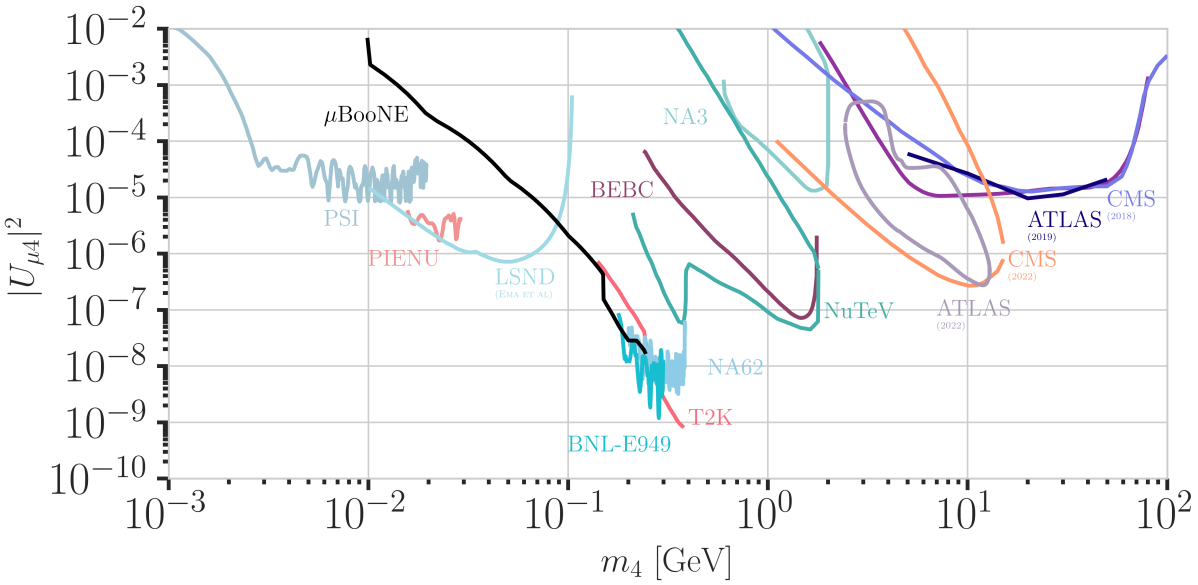

Figure 2.3: Current leading $|U_{\mu 4}|^2 - m_4$ upper limits from PSI [59], μBooNE [64], PIENU [41], LSND [65], BNL-E949 [60], NA62 [45], T2K [46], BEBC [66], ATLAS [52, 53], CMS [54, 55], NuTeV [56], and NA3 [67]. Modified from [57].

Especially noteworthy are the results of analyses probing the mixing with the third lepton generation, $|U_{\tau 4}|^2$, from *NOMAD* [61] and reinterpretations of the CHARM results and the BEBC results in the context of the mixing $|U_{\tau 4}|^2$, where the latter places the most stringent limits from 10^{-3} to 10^{-6} in the 0.1 GeV to 2 GeV range [48, 62, 63]. In Figure 2.4 the current strongest bounds on $|U_{\tau 4}|^2$ are shown.

[61]: Astier et al. (2001), "Search for heavy neutrinos mixing with tau neutrinos"

[48]: Barouki et al. (2022), "Blast from the past II: Constraints on heavy neutral leptons from the BEBC WA66 beam dump experiment"

[62]: Orloff et al. (2002), "Limits on the mixing of tau neutrino to heavy neutrinos"

[63]: Boiarska et al. (2021), "Constraints from the CHARM experiment on heavy neutral leptons with tau mixing"

Collider Searches

So far, collider searches have been conducted at the *large electron positron collider (LEP)* and at the *large hadron collider (LHC)* in proton-proton mode. Strongest results are from the *ATLAS* and *CMS* experiments, which are nearly hermetic, general purpose detectors around the interaction point, and from the *DELPHI* and the *LHCb* experiments, which are forward detectors that can be used to search for new particles in decays of heavy particles. In the minimal model, HNLs in the GeV mass range can be produced through mass mixing in decays of heavy mesons, tau leptons, Z/W bosons, H bosons, or top quarks originating from the collisions. Depending on the Dirac or Majorana nature of the HNL, they can decay to LNC or LNV channels.

Using prompt and displaced decays of the HNL, both ATLAS and CMS have set constraints on $|U_{e4}|^2$ and $|U_{\mu 4}|^2$ at the level of 10^{-4} to 10^{-6} in the mass range between 1 GeV to 100 GeV [53, 55] [52, 54]. The LHCb experiment has HNL search results at HNL masses below and above the W boson mass, where the low mass searches are using the decay channel $B^- \to \pi^+\mu^-\mu^-$, setting limits at the 10^{-3} level for $|U_{\mu 4}|^2$ in the mass range of 0.5 GeV to 3.5 GeV [68]. At high masses, the $W^+ \to \mu^-\mu^{\pm}$jet channel is used to set limits at the order of 10^{-3} to 10^{-2} for $|U_{\mu 4}|^2$ in the mass range of 5 GeV to 50 GeV in the LNC channel and at the order of 10^{-4} to 10^{-3} in the LNV channel [69]. Using hadronic Z^0 decays, searches for short- and long-lived HNLs have been conducted with the DELPHI detector setting upper limits

[53]: Aad et al. (2023), "Search for Heavy Neutral Leptons in Decays of W Bosons Using a Dilepton Displaced Vertex in $\sqrt{s}$ = 13TeV pp Collisions with the ATLAS Detector"

[55]: Tumasyan et al. (2022), "Search for long-lived heavy neutral leptons with displaced vertices in proton-proton collisions at $\sqrt{s}$ =13 TeV"

[68]: Shuve et al. (2016), "Revision of the LHCb Limit on Majorana Neutrinos"

[69]: Aaij et al. (2021), "Search for heavy neutral leptons in $W^+ \to \mu^+\mu^{\pm}$jet decays"

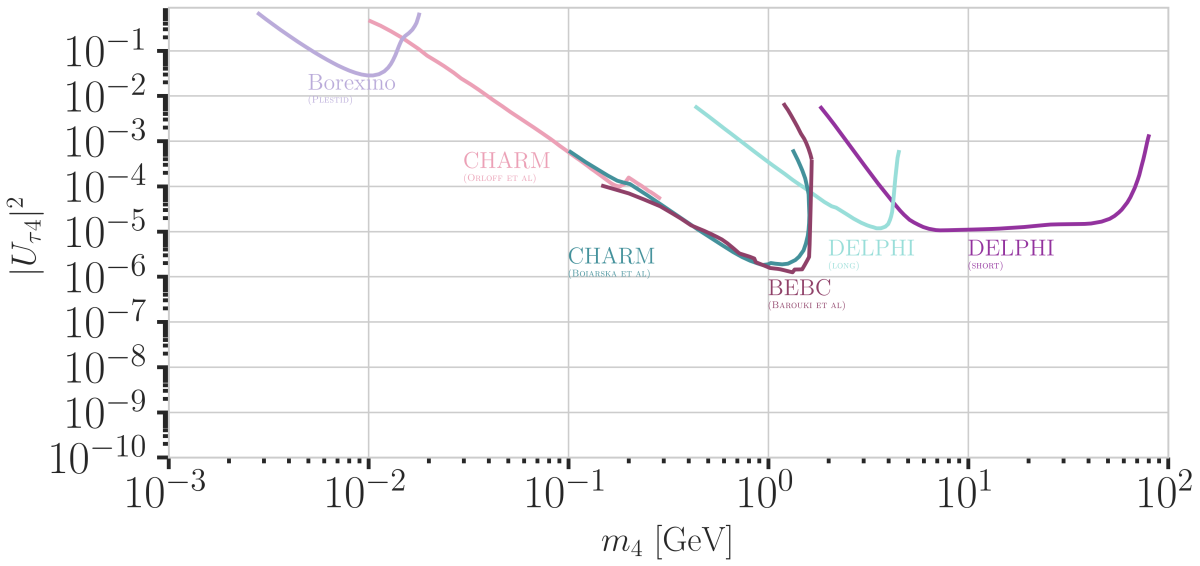

Figure 2.4: Current leading $|U_{\tau 4}|^2 - m_4$ upper limits from BOREXINO [70], CHARM [62, 63], DELPHI [47], and BEBC [48]. Modified from [57].

of the order of 10^{-5} for mixing to any SM flavor in the mass range from 3.5 GeV to 50 GeV [47].

[47]: Abreu et al. (1997), "Search for neutral heavy leptons produced in Z decays"

Nuclear Decays Measurements

A novel approach of searching for irregularities in energy-momentum conservation measurements in nuclear reactions might be a viable way of searching for HNLs, as they could be interpreted as constraints on $|U_{e4}|^2$ and m_4.

Kinks in **beta decay** spectra would show up at $Q - m_4c^2$, where the HNL mass, m_4, can be measured between the lower energy detection threshold and the energy released in the decay, which is called Q value. Analyses using the tritium decay, with $Q = 18.6$ keV, are planned in *KATRIN* citeKATRIN:2001ttj and *TRISTAN* [71] in the 1 keV to 18 keV range. Their projected statistical limits are around 10^{-7} for $|U_{e4}|^2$, but will require further detector upgrades [71]. A first result from KATRIN measurements during commissioning sets limits at the order of 10^{-2} to 10^{-3} in the mass range of 0.1 keV to 1.6 keV [72]. *DUNE* is planning to measure the ionization charge of atmospheric argon decays, with $Q = 565$ keV, to probe $|U_{e4}|^2$ at in the 20 keV to 450 keV mass range. The projected sensitivity is at the 10^{-5} level, and might improve to 10^{-7} with additional detector improvements [73].

[71]: Mertens et al. (2019), "A novel detector system for KATRIN to search for keV-scale sterile neutrinos"

[72]: Aker et al. (2023), "Search for keV-scale sterile neutrinos with the first KATRIN data"

[73]: Abi et al. (2020), "Deep Underground Neutrino Experiment (DUNE), Far Detector Technical Design Report, Volume II: DUNE Physics"

To test for the existence of HNLs using **electron capture** measurements, total energy-momentum reconstruction of all non-neutrino final states is needed. Electron capture is a pure two-body decay process, where the recoiling atom and the electron neutrino are the only final state particles, but additional energy is carried away by the de-excitation x-ray or auger electron. The energy-momentum conservation can be probed by measuring the atom and the associated de-excitation products. The mixing $|U_{e4}|^2$ can be probed by looking for a separated non-zero missing mass peak. The *BeEST* experiment has set limits at the 10^{-4} level in the 100 keV to 850 keV mass range, using

berillium-7, which has a Q value of 862 keV. After planned upgrades to the experiment, the sensitivity is expected to improve to the 10^{-7} level [74].

[74]: Friedrich et al. (2021), "Limits on the Existence of sub-MeV Sterile Neutrinos from the Decay of ^{7}Be in Superconducting Quantum Sensors"

Reactor searches up to 12 MeV in mass are possible at short baseline experiments using commercial or research reactors, which are a strong source of electron antineutrinos and could therefore also produce HNLs if $|U_{e4}|^2$ is non-zero. Visible decay channels at these energies are $\nu_4 \rightarrow \nu_e e^+ e^-$, $\nu_4 \rightarrow \nu\gamma$, and $\nu_4 \rightarrow \nu\gamma\gamma$, where the first dominates. The first analysis in this field, reports limits at the 10^{-4} level in the 2 MeV to 7 MeV mass range [75].

[75]: Hagner et al. (1995), "Experimental search for the neutrino decay v3+vj+e++e- and limits on neutrino mixing"

Atmospheric and Solar Neutrinos

Natural sources of neutrinos are provided up to 20 MeV by the sun and up to 100s of GeV by neutrino production in the atmosphere. Both fluxes contain all flavors of neutrinos, due to mixing and oscillations, and can therefore be used to directly probe the mixings with ν_e, ν_μ, and ν_τ. Depending on the HNL mass and the strength of the mixing, which both govern the decay length, different signatures can be used to experimentally access large regions of the HNL parameter space. The strength of the mixing determines the total rate of HNL events, which is additionally affected by whether solely the minimal mass mixing is assumed, or also more complicated mixing scenarios, like the dipole portal, are considered.

So far, only very few analyses exist, which are performed by the experimental collaborations themselves. Several external theoretical groups have predicted the expected sensitivities to HNLs, produced from solar or atmospheric neutrinos, based on various coupling scenarios and decay lengths. A selection of the potential analyses will be discussed in the following.

For very long-lived particles, **production inside the sun** can be used as a source to search for HNLs in detectors on earth. This will only allow production through non-zero $|U_{e4}|^2$, because the initial solar neutrino flux is only ν_e. By searching for HNL decays to a SM neutrino and an electron positron pair $\nu_4 \rightarrow \nu_e e^+ e^-$ and comparing to the expected inter planetary positron flux, *Borexino* has placed the strongest limits on the mixing $|U_{e4}|^2$ at the order of 10^{-5} in the few MeV mass range [43].

[43]: Bellini et al. (2013), "New limits on heavy sterile neutrino mixing in B8 decay obtained with the Borexino detector"

For HNL decay length scales of the order of the Earth's diameter, HNL **up-scattering outside the detector** is possible, where a neutrino from the solar or the atmospheric neutrino flux scatters in the Earth and transfers some kinetic energy to the HNL, which can later decay inside the detector. For HNL masses below 18 MeV produced from solar neutrinos, limits were derived using the Borexino data for purely tau coupling through mass mixing [70] and for all flavor coupling through the dipole portal [76]. At similar decay length scales, the HNL could also be produced directly in the atmosphere, but neither this channel, nor the production anywhere in the Earth from atmospheric neutrinos has been investigated yet.

[70]: Plestid (2021), "Luminous solar neutrinos I: Dipole portals"

[76]: Plestid (2021), "Luminous solar neutrinos II: Mass-mixing portals"

If the HNL decay lengths are sufficiently short, **production and decay in the detector** can happen and the observation of two vertices could be used to constrain the mixing parameters. In principle, this could be possible with any neutrino flavor produced in the sun or the atmosphere, but so far only theoretical studies have been performed for mass-mixing and dipole-portal couplings for the atmospheric neutrino detector IceCube [77] [78] and *Super-K*, *Hyper-K*, and Dune [79, 80]. Due to the high complexity of these

[78]: Coloma (2019), "Icecube/DeepCore tests for novel explanations of the MiniBooNE anomaly"

[79]: Atkinson et al. (2022), "Heavy Neutrino Searches through Double-Bang Events at Super-Kamiokande, DUNE, and Hyper-Kamiokande"

[80]: Coloma et al. (2021), "GeV-scale neutrinos: interactions with mesons and DUNE sensitivity"

experiments, several simplified assumptions were made in the studies, which might not hold in reality, and the results should be taken with caution. For reliable sensitivity estimates and limits the collaborations should perform their own analyses.

2.3 Atmospheric Neutrinos as Source of Heavy Neutral Leptons

This work focuses on the search for HNLs using atmospheric neutrinos as source for the production and decay inside the IceCube detector. The following sections will give a brief overview of the production of neutrinos in the atmosphere and the oscillations they undergo, before discussing the expected signatures of HNLs in the detector.

2.3.1 Production of Neutrinos in the Atmosphere

The analysis performed in this work is based on the sample of neutrinos observed in IceCube DeepCore at energies below 100 GeV. At these energies, the flux exclusively originates in the Earth's atmosphere. Highly relativistic cosmic rays (protons and heavier nuclei [81]) interact in the upper atmosphere, producing showers of secondary particles. Neutrinos are produced in decays of charged pions and kaons (π and K mesons) present in those showers, where the dominant contribution comes from the decay chain

$$\begin{aligned} \pi^{\pm} &\rightarrow \mu^{\pm} + \nu_{\mu}(\bar{\nu}_{\mu}) \,, \\ \mu^{\pm} &\rightarrow e^{\pm} + \bar{\nu}_{\mu}(\nu_{\mu}) + \nu_{e}(\bar{\nu}_{e}) \,, \end{aligned} \tag{2.26}$$

where muon neutrinos ν_{μ} and muons $\mu^{\pm}$ are produced in the first decay and both electron and muon neutrinos $\nu_{e/\mu}$ are produced in the second decay. Atmospheric muons, which are also produced in these decays, are the main background component for IceCube DeepCore analyses.

The different atmospheric flux components are shown in Figure 2.5 (left), for a much broader energy range than relevant for this work. Both neutrinos and antineutrino fluxes are shown for electron and muon neutrinos and all fluxes are the directionally averaged expectation calculated at the South Pole. Muon neutrinos are dominating the flux and from Equation 2.26 the naive

[81]: Tanabashi et al. (2018), "Review of Particle Physics"

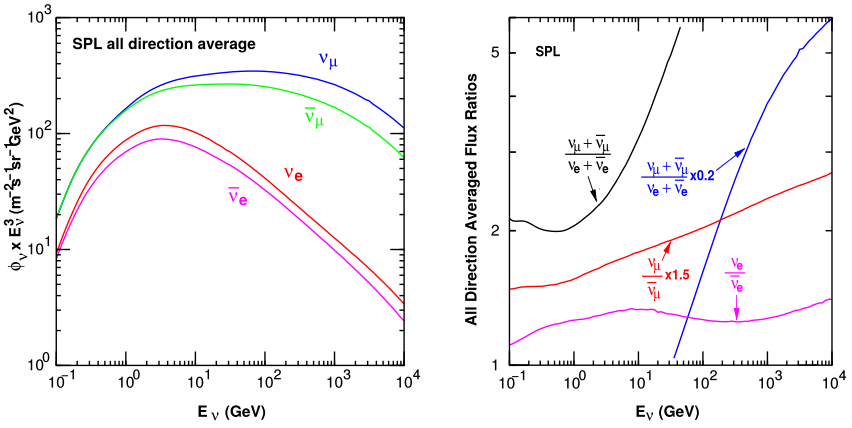

Figure 2.5: The atmospheric fluxes of different neutrino flavors as a function of energy (left) and the ratios between muon neutrinos and electron neutrinos as well as the ratios between neutrinos and antineutrinos for both those flavors (right). Results from the calculations performed for the geographic South Pole, taken from [82].

assumption would be that the ratio between muon and electron neutrinos is $(\nu_\mu + \bar{\nu}_\mu)/(\nu_e + \bar{\nu}_e) = 2$. This is roughly true at energies below 1 GeV, where all muons decay in flight, but at larger energies muons can reach the detector before decaying, which increases the ratio to approximately 10:1 at around 100 GeV. Additionally, kaon decays start to contribute which also increases the number of muons and muon neutrinos. The increasing ratio can be seen in Figure 2.5 (right), which also shows the ratio between neutrinos and antineutrinos for both flavors.

Charged mesons heavier than the tau can also be produced in cosmic ray interactions. Their decays to tau neutrinos or direct production of taus in cosmic ray interactions lead to the production of tau neutrinos. At the energies relevant for this work however, the resulting tau neutrino flux is negligible as compared to the muon neutrino flux [83] and is not considered in the analysis.

[83]: Fedynitch et al. (2015), "Calculation of conventional and prompt lepton fluxes at very high energy"

2.3.2 Neutrino Oscillations

Describing neutrinos in their mass states as introduced in Section 2.2.2 is crucial to understanding their propagation through space and time and to explaining neutrino oscillations. Oscillations mean that a neutrino changes from its initial flavor, that it was produced with, to another flavor and back after traveling a certain distance.

The neutrino propagation in vacuum can be expressed by applying a plane wave approach, where the mass eigenstates evolve as

$$|\nu_k(t)\rangle = e^{-iE_k t/\hbar} |\nu_k\rangle \ . \tag{2.27}$$

The energy of the mass eigenstate $|\nu_k\rangle$ is $E_k = \sqrt{\vec{p}^2c^2 + m_k^2c^4}$, with momentum, $\vec{p}$, mass, m_k, $\hbar$ is the reduced Planck constant, and c is the speed of light in vacuum. A neutrino is produced as a flavor eigenstate $|\nu_\alpha\rangle$ in a CC weak interaction, but its propagation happens as the individual mass states it is composed of. The probability of finding the neutrino with initial flavor $|\nu_\alpha\rangle$ in the flavor state $\left|\nu_\beta\right\rangle$ after the time t is calculated as

$$P_{\nu_\alpha \to \nu_\beta}(t) = \left| \left\langle \nu_\beta | \nu_\alpha(t) \middle| \nu_\beta | \nu_\alpha(t) \right\rangle \right|^2 , \tag{2.28}$$

[84]: Dirac (1927), "The Quantum Theory of the Emission and Absorption of Radiation"

by applying Fermi's Golden Rule [84], which defines the transition rate from one eigenstate to another by the strength of the coupling between them. This coupling strength is the square of the matrix element and using the fact that the mixing matrix is unitary ($U^{-1} = U^\dagger$) to describe the mass eigenstates as flavor eigenstates, we find the time evolution of the flavor state $|\nu_\alpha(t)\rangle$, which can be inserted into Equation 2.28 to find the probability as

$$P_{\nu_\alpha \to \nu_\beta}(t) = \sum_{j,k} U^*_{\beta j} U_{\alpha j} U_{\beta k} U^*_{\alpha k} e^{-i(E_k - E_j)t/\hbar} \ . \tag{2.29}$$

The indices j and k run over the mass eigenstates.

We can approximate the energy as

$$E_k \approx E + \frac{c^4 m_k^2}{2E} \quad \longrightarrow \quad E_k - E_j \approx \frac{c^4 \Delta m_{kj}^2}{2E} \ , \tag{2.30}$$

for very small masses compared to the kinetic energy $E \gg m_k c^2$. Here, $\Delta m^2_{kj} = m^2_k - m^2_j$ is the mass-squared splitting between states k and j, and E is the energy of the wavepacket to be detected (flavor eigenstate). Replacing the time in Equation 2.29 by the distance traveled by relativistic neutrinos $t \approx L/c$ we get

$$\begin{aligned} P_{\nu_\alpha \to \nu_\beta}(t) = \delta_{\alpha\beta} - 4 \sum_{j>k} \mathbf{Re}(U^*_{\beta j} U_{\alpha j} U_{\beta k} U^*_{\alpha k}) \sin^2\left(\frac{c^3 \Delta m^2_{kj}}{4E\hbar} L\right) \\ +2 \sum_{j>k} \mathbf{Im}(U^*_{\beta j} U_{\alpha j} U_{\beta k} U^*_{\alpha k}) \sin^2\left(\frac{c^3 \Delta m^2_{kj}}{4E\hbar} L\right), \end{aligned} \tag{2.31}$$

which is called the survival probability if $\alpha = \beta$, and the transition probability if $\alpha \neq \beta$. Once again, this probability is only non-zero if there are neutrino mass eigenstates with masses greater than zero. Additionally, there must be a mass-squared difference Δm^2 and non-zero mixing between the states. Since we assumed propagation in vacuum in Equation 2.27, the transition and survival probabilities correspond to vacuum mixing.

[81]: Tanabashi et al. (2018), "Review of Particle Physics"

The mixing matrix can be parameterized as [81]

$$U = \begin{pmatrix} 1 & 0 & 0 \\ 0 & c_{23} & s_{23} \\ 0 & -s_{23} & c_{23} \end{pmatrix} \begin{pmatrix} c_{13} & 0 & s_{13} e^{-i\delta_{CP}} \\ 0 & 1 & 0 \\ -s_{13} e^{i\delta_{CP}} & 0 & c_{13} \end{pmatrix} \begin{pmatrix} c_{12} & s_{12} & 0 \\ -s_{12} & c_{12} & 0 \\ 0 & 0 & 1 \end{pmatrix}, \tag{2.32}$$

where $c_{ij} = \cos\theta_{ij}$ and $s_{ij} = \sin\theta_{ij}$ are cosine and sine of the mixing angle θ_{ij}, that defines the strength of the mixing between the mass eigenstates i and j, and δ_{CP} is the neutrino *charge-parity (CP)* violating phase. Experiments are sensitive to different mixing parameters, depending on the observed energy range, neutrino flavor, and the distance between the source and the detector L, commonly referred to as *baseline*. To be able to resolve oscillations the argument

$$\frac{\Delta m^2 L}{4E} \tag{2.33}$$

should be at the order of 1. This divides experiments into ones that are sensitive to very slow oscillations from $\Delta m^2_{21} \approx \mathcal{O}(10^{-5}\text{eV}^2)$ and ones that are sensitive to faster oscillations from $\Delta m^2_{31} \approx \mathcal{O}(10^{-3}\text{eV}^2)$. Relevant for this work are the parameters that can be measured at the earths surface using atmospheric neutrinos, which are Δm^2_{31}, θ_{23}, and θ_{13}, because the flux is primarily composed of muon neutrinos and antineutrinos. Applying the parameterization from Equation 2.32 to Equation 2.31 and using the fact that θ_{13} is small and θ_{12} is close to $\pi/4$, the survival probability of muon neutrinos can be approximated as

$$\begin{aligned} P_{\nu_\mu \to \nu_\mu} &\simeq 1 - 4|U_{\mu 3}|^2 (1 - |U_{\mu 3}|^2) \sin^2\left(\frac{\Delta m^2_{31} L}{4E}\right) \\ &\simeq 1 - \sin^2\left(2\theta_{23}\right) \sin^2\left(\frac{\Delta m^2_{31} L}{4E}\right), \end{aligned} \tag{2.34}$$

while the tau neutrino appearance probability is

$$\begin{aligned} P_{\nu_\mu \to \nu_\tau} &\simeq 4|U_{\mu 3}|^2 |U_{\tau 3}|^2 \sin^2\left(\frac{\Delta m^2_{31} L}{4E}\right) \\ &\simeq \sin^2\left(2\theta_{23}\right) \sin^2\left(\frac{\Delta m^2_{31} L}{4E}\right). \end{aligned} \tag{2.35}$$

Parameter	Global Fit
θ_{12} [°]	$33.41^{+0.75}_{-0.72}$
θ_{13} [°]	$8.54^{+0.11}_{-0.12}$
θ_{23} [°]	$49.1^{+1.0}_{-1.3}$
Δm^2_{21} [10^{-5}eV^2]	$7.41^{+0.21}_{-0.20}$
Δm^2_{31} [10^{-3}eV^2]	$2.511^{+0.028}_{-0.027}$
δ_{CP} [°]	197^{+42}_{-25}

Table 2.2: Results from the latest global fit of neutrino mixing parameters from [85].

The latest global fit [85] of all the parameters is shown in Table 2.2.

[85]: Esteban et al. (2020), "The fate of hints: updated global analysis of three-flavor neutrino oscillations"

2.3.3 Neutrino Interactions with Nuclei

The neutrino detection principle of IceCube DeepCore is explained in Chapter 3 and relies on the weak interaction processes between neutrinos and the nuclei of the Antarctic glacial ice. At neutrino energies above 5 GeV, the cross-sections are dominated by ***deep inelastic scattering (DIS)***, where the neutrino is energetic enough to resolve the underlying structure of the nucleons and interact with one of the composing quarks individually. As a result the nucleon breaks and a shower of hadronic secondary particles is produced. Depending on the type of interaction, the neutrino either remains in the final state for NC interactions or is converted into its charged lepton counterpart for CC interactions. The CC DIS interactions have the form

$$\begin{aligned} \nu_\alpha + N &\rightarrow l_\alpha^- + X \ , \\ \bar{\nu}_\alpha + N &\rightarrow l_\alpha^+ + X \ , \end{aligned} \tag{2.36}$$

where $\nu_\alpha / \bar{\nu}_\alpha$ and l_α^- / l_α^+ are the neutrino/antineutrino and its corresponding lepton/antilepton for $\alpha = e, \mu, \tau$. N is the nucleon and X stands for any set of final state hadrons. The NC DIS interactions are

$$\begin{aligned} \nu_\alpha + N &\rightarrow \nu_\alpha + X \text{ and} \\ \bar{\nu}_\alpha + N &\rightarrow \bar{\nu}_\alpha + X \ . \end{aligned} \tag{2.37}$$

DIS interactions have a roughly linear energy dependent cross-section above ~20 GeV and are well measured and easy to theoretically calculate. They are the primary interaction channel for neutrinos detected with IceCube. Figure 2.6 shows the Feynman diagrams for both processes.

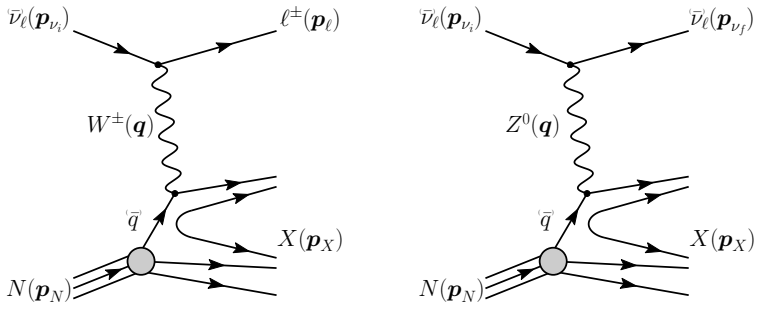

Figure 2.6: Feynman diagrams for deep inelastic scattering of a neutrino with a nucleon via charged-current (left) and neutral current (right) interactions. $\boldsymbol{p}_{\nu_i}$, $\boldsymbol{p}_N$ and $\boldsymbol{p}_{\nu_f}$, $\boldsymbol{p}_l$, $\boldsymbol{p}_N$ are the input and output four-momenta, while $\boldsymbol{q}$ is the momentum transfer. Taken from [86].

At energies below 5 GeV, ***quasi-elastic scattering (QE)*** and ***resonant scattering (RES)*** become important. At these energies the neutrinos interact with the approximately point-like nucleons, without breaking them up in the process. RES describes the process of a neutrino scattering off a nucleon producing an excited state of the nucleon in addition to a charged lepton. It is the dominant process from 1.5 GeV to 5 GeV for neutrinos and from 1.5 GeV to 8 GeV for antineutrinos. Below 1.5 GeV QE is the dominant process, where protons are converted to neutrons in antineutrino interactions and vice-versa for neutrino interactions. Additionally, a charged lepton corresponding to the neutrino/antineutrino flavor is produced. The cross-sections of QE and RES scattering processes are not linear in energy and the transition region from QE/RES to DIS is poorly understood. The total cross-sections and their

composition is shown in Figure 2.7. It can be seen that the interaction cross-sections are very small at the order of 10^{-38} cm^2. This is the reason why very large volume detectors are required to measure atmospheric neutrinos with sufficient statistics to perform precision measurements of their properties.

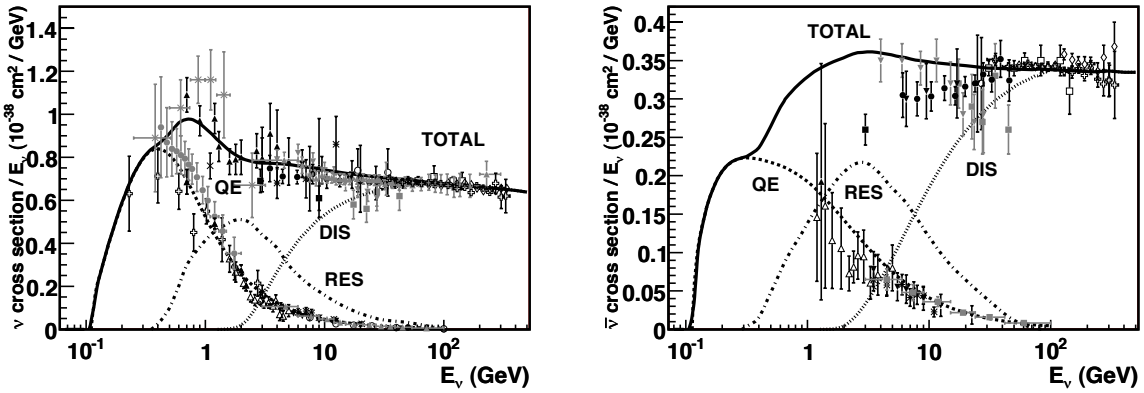

Figure 2.7: Total neutrino (left) and antineutrino (right) per nucleon cross-section divided by neutrino energy plotted against energy. The three main scattering processes quasi-elastic scattering (QE), resonant scattering (RES), and deep-inelastic scattering (DIS) are shown. Taken from [87].

2.3.4 Heavy Neutral Lepton Production and Decay

For the search conducted in this work, both production and decay of the HNL are assumed to happen inside the detector, therefore probing decay length ranges at the scale of the detector size, which is below 1000 m. Since the mixing with the first two generations of leptons is already strongly constrained as was discussed in Section 2.3, only the mixing with the tau neutrino will be considered in the following. Due to the effect of oscillations, described in Section 2.3.2, the initial atmospheric muon neutrino flux provides a sizable tau neutrino flux at the detector.

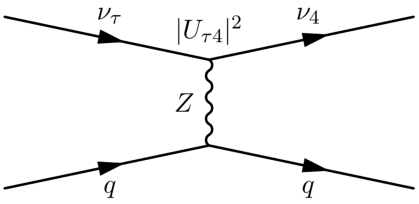

Figure 2.8: Feynman diagram of the HNL production. The heavy mass state is produced in the up-scattering of a tau neutrino.

For a non-zero $|U_{\tau 4}|^2$, the HNL can be produced through **up-scattering in the ice**. An incoming tau neutrinos scatters on an ice nucleus and transfers some of its kinetic energy to the heavy neutrino. The Feynman diagram of this process is shown in Figure 2.8. The custom NC cross-sections calculated for this purpose are explained in more detail in Section 4.2.1, but are similar to the SM tau neutrino NC cross-sections, with a reduction, scaling with the mixing $|U_{\tau 4}|^2$, and energy dependent reductions, due to kinematic constraints because of the heavy neutrino mass. The scattering process produces a hadronic cascade, which will produce light in the detector.

After a certain distance, the HNL will **decay in the ice**, where the possible decay channels considered in this work and the underlying, explicit calculations are discussed in Section 4.2.1. The decay can be a CC or NC and both purely leptonic and leptonic+mesonic modes are possible. The

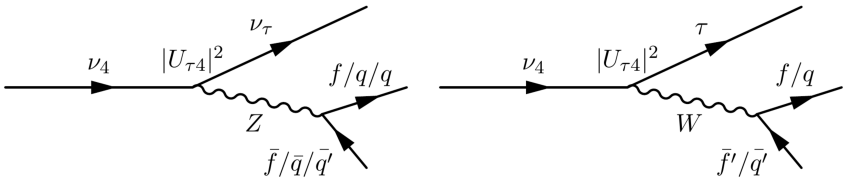

Figure 2.9: Feynman diagram of the HNL decay. The heavy mass state can decay through neutral current interaction (left) into a tau neutrino and a charged lepton or quark pair, or through charged current interaction (right) into a tau lepton and a charged lepton or quark.

Feynman diagrams of the decays can be seen in Figure 2.9. Only the mass range relevant for this work is presented and mixing with $\nu_{e/\mu}$ is assumed to be negligible. Depending on the decay channel, an electromagnetic or a hadronic cascade is produced, while some energy is carried away by the invisible neutrino. The decay length of the HNL is defined by its proper lifetime[2], which is given by

$$\tau_{\text{proper}} = \frac{\hbar}{\Gamma_{\text{total}}(m_4) \cdot |U_{\tau 4}|^2} \,, \tag{2.38}$$

where $\hbar$ is the reduced Planck constant, $\Gamma_{\text{total}}(m_4)$ is the total decay width of the HNL for the given mass, and $|U_{\tau 4}|^2$ is the mixing with the tau neutrino. The total decay width is the sum of the partial decay widths for all possible decay channels. The mean lab frame decay length is then given by

$$L_{\text{decay}} = \gamma v \tau_{\text{proper}} \,, \tag{2.39}$$

where γ is the Lorentz factor of the HNL, defined by the kinetic energy. This will be further discussed in Section 4.2.1. Figure 2.10 shows the mean decay length for an example mass of $m_4 = 0.6\,\text{GeV}$ and several mixing values.

2: A particle decay time follows an exponential distribution, with mean lifetime given by the proper lifetime. The proper lifetime is the lifetime in the rest frame of the particle.

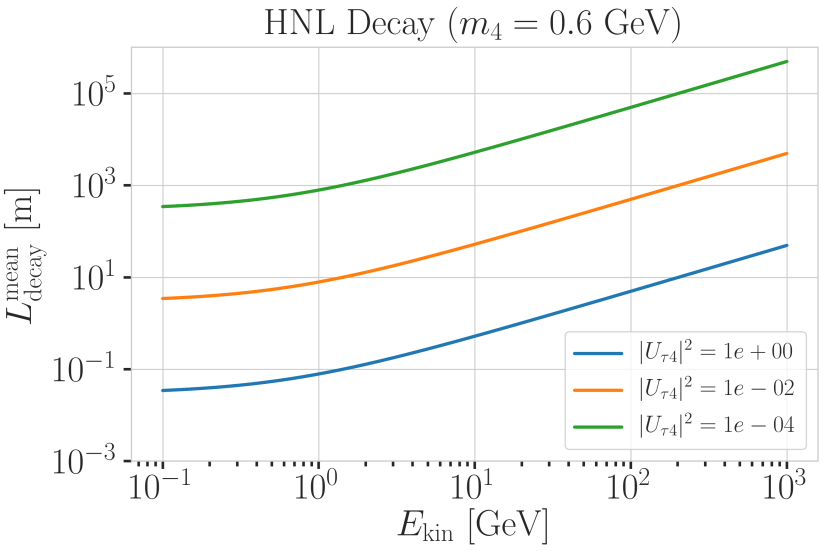

Figure 2.10: Theoretical mean decay length of the HNL for a mass of 0.6 GeV and different mixing values.

The IceCube Neutrino Observatory

3

The IceCube Neutrino Observatory [6] is a cubic-kilometer, ice-Cherenkov detector located at the geographic South Pole. IceCube utilizes the Antarctic glacial ice as detector medium to observe neutrinos by measuring the Cherenkov light produced from secondary charged particles. It was deployed between 2006 and 2011 and has been taking data since the installation of the first modules. The primary goal of IceCube is the observation of astrophysical neutrinos as a telescope, but it can also be used to study fundamental particle physics properties using the same astrophysical neutrinos, and by measuring atmospheric neutrinos as well as studying cosmic rays.

3.1 Detector Components

[6]: Aartsen et al. (2017), "The IceCube Neutrino Observatory: instrumentation and online systems"

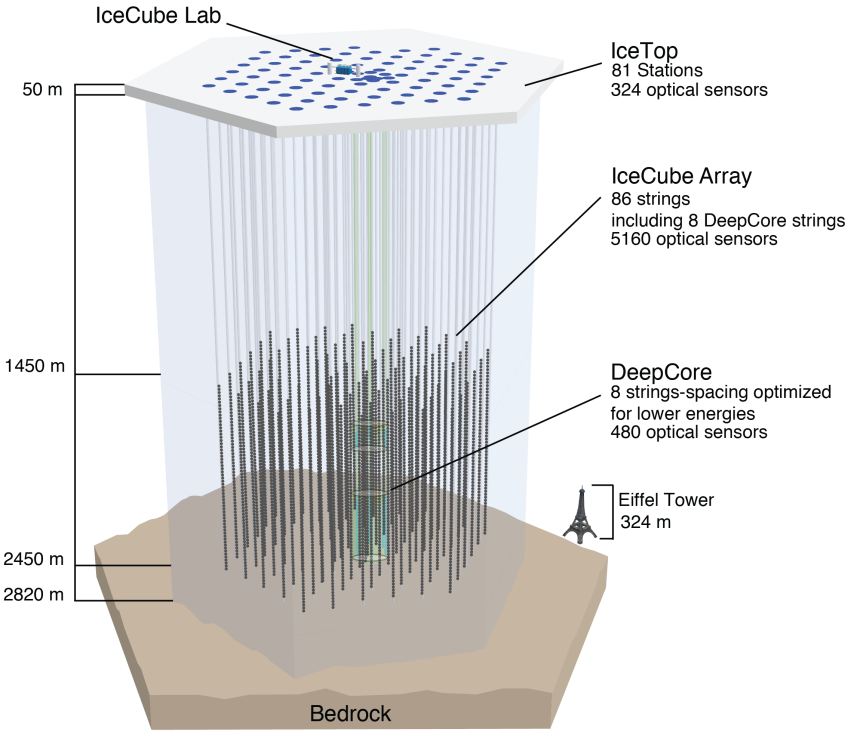

Figure 3.1: Overview of the IceCube detector showing the in-ice main- and sub-array IceCube and DeepCore, IceTop, and the IceCube Laboratory. From [6].

The full IceCube detector array consists of 86 vertical, in-ice strings and 81 surface stations as shown in Figure 3.1. The in-ice part is composed of 60 optical modules per string deployed at depths of 1450 m - 2450 m below the ice, while the surface stations of the cosmic air-shower array, *IceTop*, are ice-filled tanks. The surface stations and the majority of the strings are arranged in a hexagonal grid with the operations building, the *IceCube Laboratory* (ICL), central to the grid on the surface. A top view of the hexagonal arrangement is shown in Figure 3.4. The in-ice array is designed to detect neutrinos in the energy range from GeV to PeV.

3.1.1 Digital Optical Modules and the Antarctic Ice

The IceCube detection medium is the Antarctic glacial ice itself, which was formed over 100 000 years by accumulation of snow that was subsequently compressed by its own weight to form a dense crystal structure [88]. As a result of this formation process, the optical properties primarily change with depth. Cherenkov light propagating through the ice is subject to scattering and absorption, which are the two most important ice properties for the detection of neutrinos. Within the detector volume the absorption length ranges from 100 m - 400 m, while the scattering length lies between 20 m and 100 m [89]. The absorption length is the distance at which the survival probability of the light is reduced to $1/e$ of its original value, while the scattering length is defined as the average distance between scatters. In the antarctic ice, they are correlated, with the absorption length being roughly four times the scattering length [90]. The vertical distribution of the inverse absorption length can be seen in Figure 3.2, where one dominant feature is the *dust layer* between 2000 m and 2100 m depth. This region has a higher concentration of dust particles that were deposited in a period of high volcanic activity, which leads to bad optical properties in form of larger scattering and absorption [89].

[88]: Price et al. (2000), "Age vs depth of glacial ice at South Pole"

[89]: Ackermann et al. (2006), "Optical properties of deep glacial ice at the South Pole"

[90]: Abbasi et al. (2022), "In-situ estimation of ice crystal properties at the South Pole using LED calibration data from the IceCube Neutrino Observatory"

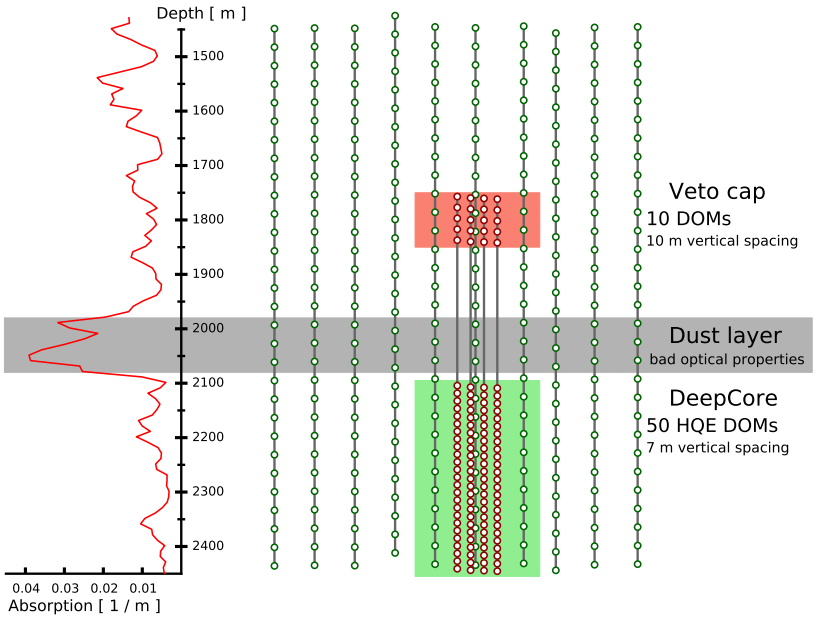

Figure 3.2: Side view of IceCube and DeepCore showing the depth inverse of the absorption length (left panel) and the DOM positions around the dust layer.

The ice is instrumented by 5160 optical sensors called *digital optical modules* (DOMs) [91], which can detect the Cherenkov light produced by charged particles traveling through the ice. Each DOM is made of a spherical glass housing, containing a downward-facing *photomultiplier tube (PMT)*, the mainboard with control, readout, and processing-electronics, and a LED flasherboard for calibration purposes. The design and the individual components of a DOM can be seen in Figure 3.3.

[91]: Abbasi et al. (2009), "The IceCube data acquisition system: Signal capture, digitization, and timestamping"

The majority of PMTs are the 10 " Hamamatsu R7081-02, which have a bialkali photocathode and are sensitive to wavelengths in the range of 300 nm to 650 nm, with a peak quantum efficiency of 25 % at 390 nm [6]. The average dark count rate during operation in the ice is ~300 Hz. The DOM electronics measure the PMT voltage and control the gain. At a voltage crossing of the equivalent to 0.25 PE the waveform readout is activated [91]. Only when

[6]: Aartsen et al. (2017), "The IceCube Neutrino Observatory: instrumentation and online systems"

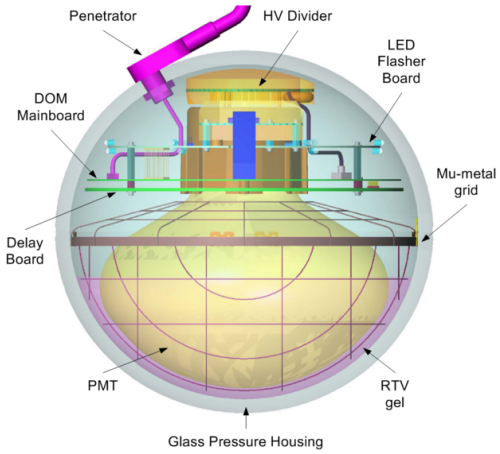

Figure 3.3: Design and components of a digital optical module (DOM) [91]

either one of the nearest or next to nearest DOMs above or below also sees a voltage crossing within a 1 µs time window [1], the voltages are digitized and sent to the ICL. Through the application of a waveform unfolding algorithm, called *WaveDeform* [92], the waveforms are compressed, and the results are the reconstructed times and charges of the photo-electrons. This is the basis for all further IceCube data processing.

1: This is referred to as a *hard local coincidence (HLC)* [91].

[92]: Aartsen et al. (2014), "Energy Reconstruction Methods in the IceCube Neutrino Telescope"

The PMT is covered with a mu-metal grid (made from wire mesh), shielding the photocathode from Earth's magnetic field, and it is optically coupled to the glass sphere by RTV silicone gel. The glass sphere is a pressure vessel, designed to withstand both the constant ice pressure and the temporary pressure during the refreezing process of the water in the drill hole during deployment (peaking at around 690 bar). The sphere is held by a harness that connects the DOMs along a string and also guides the cable for power supply and communication beside them.

The flasher-board controls 12 LEDs that produce optical pulses with a wavelength of 405 nm [6]. The LEDs can be pulsed separately or in combination with variable output levels and pulse lengths. Using the known information of the light source positions and times this can be used for in-situ calibration of the detector by measuring absorption and scattering properties of the ice. Calibrating the absolute efficiency of the DOMs itself is more accurately done using minimum ionizing muons [93, 94], since the total amplitude of the LED light is not well known.

[6]: Aartsen et al. (2017), "The IceCube Neutrino Observatory: instrumentation and online systems"

[93]: Feintzeig (2014), "Searches for Point-like Sources of Astrophysical Neutrinos with the IceCube Neutrino Observatory"
[94]: Kulacz (2019), "In Situ Measurement of the IceCube DOM Efficiency Factor Using Atmospheric Minimum Ionizing Muons"

3.1.2 IceCube Main-Array

The 78 strings that are arranged in a hexagonal pattern from the main part of the in-ice array, which is called *IceCube*. With a ~125 m horizontal spacing between the strings and a ~17 m vertical spacing between DOMs, IceCube has a lower energy detection threshold of around 100 GeV. IceCube was designed to detect high energy neutrinos of astrophysical origin.

The coordinate system that is used in IceCube is centered at 46500'E, 52200'N at an elevation of 883.9 m [6]. Per definition, it is a right-handed coordinate system where the y-axis points along the Prime Meridian (Grid North) towards Greenwich, UK, and the x-axis points 90° clockwise from the y-axis (Grid East). The z-axis is normal to the ice surface, pointing upwards. For

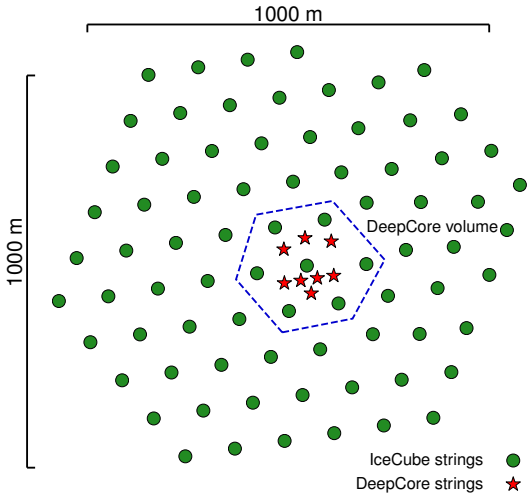

Figure 3.4: Top view of the IceCube array.

IceCube analyses, depth is defined as the distance along the z axis from the ice surface, fixed at an elevation of 2832 m.

3.1.3 DeepCore Sub-Array

[95]: Abbasi et al. (2012), "The design and performance of IceCube DeepCore"

The additional 8 strings form a denser sub-array of IceCube called *DeepCore* [95]. It is located at the bottom-center of the in-ice array and its *fiducial volume* also includes the 7 surrounding IceCube strings as shown in Figure 3.4. The strings in this region have a closer average horizontal distance of about 70 m. The lower 50 DeepCore DOMs on each string are placed in the region of clear ice below the dust layer between 2100 m to 2450 m depth, where their vertical spacing is ~7 m. The remaining 10 modules on each string are placed above the dust layer to be used as veto against atmospheric muons as can be seen in Figure 3.2. Additionally, the DeepCore DOMs are equipped with higher quantum efficiency PMTs[2]. The combination of the denser spacing, the high quantum efficiency modules, and the most favorable ice properties below the dust layer leads to a lower energy detection threshold of around 5 GeV, allowing the more efficient observation of atmospheric neutrinos. This lower threshold enables measurements of neutrino oscillations and many other BSM studies such as dark matter searches, measurements of non-standard interactions, and searches for sterile neutrinos [95].

2: At 400 nm they are 35 % more efficient than the IceCube PMTs [95].

3.2 Particle Propagation in Ice

Neutrinos interacting in the ice via DIS produce muons, electromagnetic showers, and hadronic showers, depending on their flavor and the interaction type. The particles produced in those processes mainly lose their energy through *ionization*, *bremsstrahlung*, *pair production*, and the *photo-nuclear interaction*. Electrically charged particles also emit Cherenkov light when traveling through the ice, which is the main observable in IceCube, but only contributes a small amount to the total energy loss.

3.2.1 Cherenkov Effect

The detection principle of IceCube DeepCore is based on the observation of Cherenkov photons that are emitted by the charged secondary particles produced in the neutrino interactions that were introduced in Section 2.3.3. The Cherenkov effect was first observed by Pavel Cherenkov in 1934 [96] and occurs when the charged particle travels faster than the phase velocity of light, therefore polarizing the medium. Upon de-excitation the molecules emit the received energy as photons in a spherical wavefront. Since the particle moves past this wavefront, the superposition of the spherical light emissions forms a cone, which is shown in blue in the bottom panel of Figure 3.5.

[96]: Cherenkov (1937), "Visible Radiation Produced by Electrons Moving in a Medium with Velocities Exceeding that of Light"

Using trigonometry, the angle θ_c at which the Cherenkov light is emitted can be calculated as

$$\theta_c = \arccos\left(\frac{1}{\beta n}\right), \tag{3.1}$$

where $\beta = v/c_{\text{vacuum}}$ is the velocity of the particle in units of the speed of light, and n is the refractive index of the medium that defines the speed of light in the medium $c = c_{\text{vacuum}} * n$. When the particle velocity is close to the speed of light, the equation holds and the angle is only dependent on the refractive index of the medium. For ice, the refractive index is $n \approx 1.3$ and as a result $\theta_c \approx 41°$ [97].

The frequency of the emission depends on the charge z and the wavelength-dependent index of refraction $n(\omega)$ and is given by the Frank-Tamm formula [98, 99]

$$\frac{d^2N}{dxd\lambda} = \frac{2\pi\alpha z^2}{\lambda^2}\left(1 - \frac{1}{\beta^2 n(\omega)^2}\right), \tag{3.2}$$

with $\alpha \approx 1/137$ the fine structure constant, λ the wavelength of the emitted light, and x the path length traversed by the particle. Relativistic particles in ice produce roughly 250 photons per cm in the wavelength range of 300 nm - 500 nm [100].

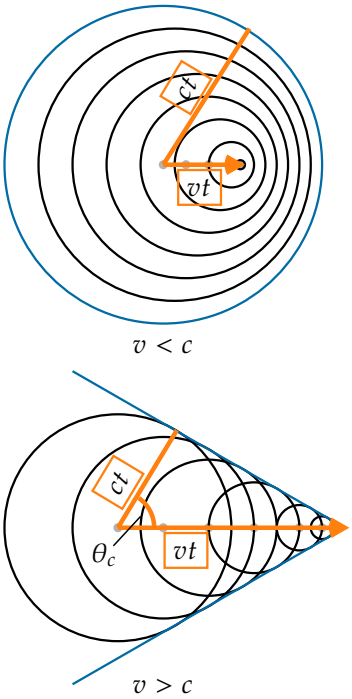

Figure 3.5: Schematic depiction of the spherical light front produced by a particle traveling slower than the speed of light in the medium (top) and the formation of the Cherenkov light front produced by a charged particle traveling faster than the speed of light in the medium (bottom). The speed of light in the medium is c, v is the speed of the particle, and t is the time that has passed. Blue is the resulting wavefront, while the black circles are spherically emitted light at each position and the orange arrows show the direction of the particle.

3.2.2 Energy Losses

Even though relativistic, charged particles traveling through matter produce Cherenkov radiation, their energy is mainly lost through other processes that are dependent on the particle type and energy. The exact principles of energy loss for the different types can broadly be categorized into the three groups: quasi-continuous energy loss by muons, electromagnetic cascades, and hadronic cascades.

Muons

Muons lose their energy by ionization, bremsstrahlung, pair production, and the photo-nuclear effect. The energy loss by ionization is the dominant process for muons above 1 GeV and has a weak energy dependence given by [21]

$$\left\langle -\frac{\mathrm{d}E}{\mathrm{d}x} \right\rangle = a_I(E) + b_R(E) \cdot E\,, \tag{3.3}$$

where E is the energy, and $a_I(E)$ and $b_R(E) \cdot E$ are the energy loss by ionization and the combined radiative losses, respectively. In the energy range relevant

[98]: Frank et al. (1937), "Coherent visible radiation from fast electrons passing through matter"
[99]: Tamm (1991), "Radiation Emitted by Uniformly Moving Electrons"

for this work (below 100 GeV), the parameters a_I and b_R only depend very weakly on energy and can be approximated by constants. The energy loss is then given by

$$\left\langle -\frac{\mathrm{d}E}{\mathrm{d}x} \right\rangle = a + b \cdot E \ . \tag{3.4}$$

Based on this description, there is a critical energy which divides the regimes where ionization and radiative losses dominate. The critical energy is given by $E_{\text{crit}} = a/b$ and for muons in ice it is ~713 GeV (using $a \approx 2.59\,\text{MeVcm}^{-1}$ and $b \approx 3.63 \times 10^{-6}\,\text{cm}^{-1}$ [101]). Since the energy range of interest is well below this critical energy, the range of a muon can easily be related to its energy by

[101]: Chirkin et al. (2004), "Propagating leptons through matter with Muon Monte Carlo (MMC)"

$$\langle L \rangle = \frac{E_0}{a} \ . \tag{3.5}$$

Measuring the length of a muon track therefore allows for an estimation of its energy if the full track is contained within the instrumented volume of IceCube. Using the given numbers, a 30 GeV muon travels ~116 m, which is well within the instrumented volume of IceCube, which spans across distances of up to 1000 m. This approximate treatment does not take into account the stochastic nature of some energy losses. Bremsstrahlung and photo-nuclear interactions for example rarely occur, but when they do, they deposit a large portion of energy. A thorough investigation of the energy losses of muons in ice can be found in [102].

[102]: Raedel (2012), "Simulation Studies of the Cherenkov Light Yield from Relativistic Particles in High-Energy Neutrino Telescopes with Geant4"

Electromagnetic Showers

Photons as well as electrons and positrons are produced either directly in neutrino interactions or in secondary particle interactions. Above a critical energy E_c, they lose their energy through repeated pair production and bremsstrahlung emission forming an expanding, electromagnetic shower profile. The particles' energy reduces with every interaction and their number increases until they fall below the critical energy where ionization and excitation of surrounding atoms become the dominant energy loss processes for electrons and positrons. For photons the remaining energy is lost through the Compton effect and the photoelectric effect [21]. Below the critical energy no new shower particles are produced.

[21]: Workman et al. (2022), "Review of Particle Physics"

Electromagnetic cascades can be characterized by the radiation length, X_0, after which electrons/positrons reduced their energy to $1/e$ of their initial energy. For photons, it is equivalent to 7/9 of the mean free path of pair production. The critical energy for ice is $E_c \approx 78$ MeV, with a radiation length of $X_0 \approx 39.3$ cm [81].

[81]: Tanabashi et al. (2018), "Review of Particle Physics"

The radiation length governs the longitudinal shower profile and using $t = x/X_0$, the shower intensity can be described by a gamma distribution [21] [103]

[103]: Longo et al. (1975), "Monte Carlo Calculation of Photon Initiated Electromagnetic Showers in Lead Glass"

$$\frac{dE}{dt} = E_0 b \frac{(bt)^{a-1} e^{-bt}}{\Gamma(a)} \ , \tag{3.6}$$

where a and b are parameters that have to be estimated from experiment, and E_0 is the initial shower energy. Based on the work from [102], performed with GEANT4 [104], the parameters for electromagnetic showers in ice are

[104]: Agostinelli et al. (2003), "Geant4—a simulation toolkit"

$$e^- : \; a \approx 2.01 + 1.45 \log_{10}(E_0/\text{GeV}),\, b \approx 0.63 \,, \tag{3.7a}$$
$$e^+ : \; a \approx 2.00 + 1.46 \log_{10}(E_0/\text{GeV}),\, b \approx 0.63 \,, \tag{3.7b}$$
$$\gamma : \; a \approx 2.84 + 1.34 \log_{10}(E_0/\text{GeV}),\, b \approx 0.65 \,. \tag{3.7c}$$

The maximum of the shower is at $t_{max} = (a-1)/b$ and the Cherenkov emission of the charged particles produced in the shower is peaked around the Cherenkov angle. Figure 3.6 shows the angular shower profile of an EM shower from an electron, which peaks sharply around the Cherenkov angle.

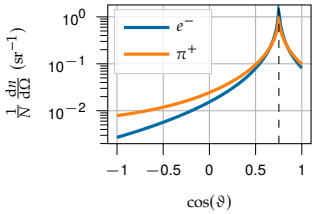

Figure 3.6: Angular Cherenkov emission profile of an EM shower (e^-) and a hadronic cascade (π^+), taken from [19], based on the parameterizations from [102].

[105]: Gabriel et al. (1994), "Energy dependence of hadronic activity"

Hadronic Showers

In DIS interactions, a cascade is always produced by the hadrons coming from the target nucleus that is breaking apart. The cascade is a result of secondary particles produced in strong interactions between the hadrons and the traversed matter. The charged particles produced in the shower will emit Cherenkov radiation, while neutral particles will be invisible to the detector. There is also an electromagnetic component of the shower, for example, due to the decay of neutral pions into photons. Hadronic showers of the same energy as electromagnetic showers have larger fluctuations in energy deposition and shape, since they depend on the produced particle types. Hadrons also have a higher energy threshold for Cherenkov light production, because of their higher mass. Based on [102] [105], the visible electromagnetic fraction of hadronic showers can be parameterized as

$$F(E_0) = \frac{T_{\text{hadron}}}{T_{\text{EM}}} = 1 - (1 - f_0)\left(\frac{E_0}{E_s}\right)^{-m} \,, \tag{3.8}$$

where $T_{\text{hadron/EM}}$ is the total track length of a hadronic/electromagnetic shower with the same energy, f_0 is the ratio of hadronic and electromagnetic light yield, E_0 is the initial energy, and E_s is an energy scale. The parameter m is a free model parameter. The ratio $F(E_0)$ increases with energy, but is always smaller than 1. The variance of this distribution is given by

$$\sigma_F(E_0) = \sigma_0 \log(E_0)^{-\gamma} \,. \tag{3.9}$$

The parameters m, E_s, and f_0 were estimated by fitting the model to the results of Geant4 simulations. Cherenkov light from hadronic showers also peaks around the Cherenkov angle, but the angular distribution is more smeared out, due to the variations in particle type and their energy depositions. This can be seen in Figure 3.6, where the angular emission profile of a shower from a π^+ is shown as an example for a hadronic shower.

3.3 Event Morphologies

The event morphologies produced by particles detected in IceCube are combinations of the three energy loss types described in Section 3.2.2, e.g. *cascades* from electromagnetic and hadronic showers and elongated *tracks* from muons traveling through the detector. Table 3.1 gives an overview of the possible event signatures from standard model interactions. The unique double-cascade signature of the HNL, introduced in Section 2.3.4 is not listed again in the table.

Table 3.1: IceCube low energy event signatures, their underlying interaction type, and the particles that produce them. Also shown are the secondary particles produced in the interactions. Black dashed lines represent neutrinos, green lines muons, orange line leptons, and blue and red lines are particles in electromagnetic and hadronic cascades, respectively. Adapted from [86].

Interaction	Secondary particles	Signature
CC $\overset{(-)}{\nu}_\mu$	 $\mu^\pm$ track	Track-only
	 $\mu^\pm$ track and hadrons	Cascade + track
CC $\overset{(-)}{\nu}_\tau$	 $\tau^\pm$ decaying into $\mu^\pm$ (~17% BR), hadrons	
	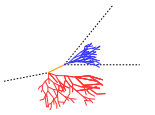 $\tau^\pm$ decaying into $e^\pm$ or hadrons (~83% BR)	
CC $\overset{(-)}{\nu}_e$	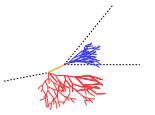 $e^\pm$, hadrons	Cascade-only
NC $\overset{(-)}{\nu}_\ell$	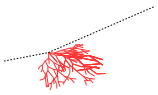 hadrons	

Neutrino interactions are observed as cascades, tracks, or a combination of both, depending on the initial flavor and the interaction type for the specific event.

In ν_μ-CC interactions, a muon is produced in addition to a hadronic shower. If the interaction happens outside the detector, but the muon passes through the detector, this will create a track-like signature. The same happens if the interaction happens inside, but the energy transfer to the nucleus is small ($y \approx 0$). At energies relevant for this work, tracks have length at the same order of the distance between DOMs, so they can be observed as such.

If the interaction happens inside the detector and the energy transfer to the hadronic part of the shower is larger, it will create a cascade with a track leaving it. A similar signature is observed after a ν_τ-CC interaction, in which a tau is produced that later decays into a muon, with a branching ratio of 17 %. In those cases the muon usually has a lower energy and the track will be fainter and harder to observe.

The other 83 % of ν_τ-CC interactions produce a tau that decays into an electron or hadrons, leaving a cascade-only signature through the electromagnetic or hadronic shower. All ν_e-CC interactions produce pure cascades, since the electron quickly loses its energy in an electromagnetic shower. In all ν - NC interactions, the produced neutrino escapes and only the hadronic shower is observable. Since the size of the cascades at the energy range of interest is smaller than the spacing of the DOMs, they are approximately observed as point-like, spherical light sources. This is just an approximation, though, and some asymmetry remains in the light profile, which can be used to reconstruct the direction of the incoming neutrino.

Atmospheric muons also produce pure track-like signatures, similar to ν_μ-CC interactions happening outside the detector. They are one of the main backgrounds for analyses using atmospheric neutrinos and are therefore the target of many filter steps described in Section 5.1.1.

Monte Carlo Event Generation and Detector Simulation

4

Like many analyses in IceCube, this work is based on MC simulations. The initial step for all particle (non-noise) simulation is the generation of events from selected initial distributions and fluxes. Events are the primary particle and all particles produced in the interaction with the ice. The particles are then propagated through the ice, producing Cherenkov photons, which are propagated further until they reach a DOM or are absorbed in the ice. If they hit a DOM the detector response is simulated. Splitting the simulation steps has the advantage of reusing the outputs of for example the generation step to propagate the particles with different ice model, in order to estimate the systematic impacts of uncertainties of the ice properties. A similar approach can be taken for varying detector response, before starting the event selection. Through this a more efficient (reduced) use of computing resources can be achieved.

The central part of this thesis is the HNL signal simulation itself. Since this is the first search for HNLs with IceCube DeepCore, there was no prior knowledge of the number of events expected per year nor of the performance in terms of reconstruction and classification accuracy. This chapter describes the first HNL event generation developed for IceCube DeepCore. Two avenues of generation were pursued in parallel. A collection of model-independent samples is explained in Section 4.1. They were used for performance benchmarking and for cross-checks to validate the physically accurate, model-dependent event generation, which is described in Section 4.2. The event generation for SM background events is briefly described in Section 4.3, followed by the detector response simulation in Section 4.4.

4.1 Model-Independent Heavy Neutral Lepton Event Generation

To investigate the potential of IceCube to detect HNLs by identifying the unique double-cascade morphology explained in Section 2.3.4, a model-independent double-cascade generator was developed, where the kinematics of each cascade can be controlled directly. Using this generator, several simulation samples were produced to investigate the performance of IceCube DeepCore to detect low-energy double-cascades, dependent on their properties. All samples are produced using a collection of custom generator functions [106] that place two EM cascade vertices with variable energy and direction at configurable locations in the detector.

4.1.1 Simplistic Samples

To investigate the best-case and the worst-case double-cascade event scenarios, two samples are produced in the DeepCore volume: straight up-going events ($\cos(\theta) = -1$) that are centered on a string and horizontal events ($\cos(\theta) = 0$). The first sample is used to investigate one of the most promising scenarios to detect a double-cascade, where both cascade centers are

located on a DeepCore string and the directions are directly up-going. One of the DeepCore strings was randomly chosen as the x-y coordinate for this sample. As already mentioned in Section 3.1.3, DeepCore strings have higher quantum efficiency DOMs and a denser vertical spacing, making them better to detect low-energy events that produce little light. To produce the events, the x, y position of the cascades is fixed to the center of the string while the z positions are each sampled uniformly along the axis of the string. Note that this will therefore not produce a uniform length distribution between the cascades. The positions are defined in the IceCube coordinate system that was introduced in Section 3.1.2. The energies are sampled uniformly between 0.0 GeV and 60.0 GeV, to generously cover the region where $\nu_\mu \rightarrow \nu_\tau$ appearance is maximized. The time of the lower cascade is set to $t_0 = 0.0$ ns and for the upper one to $t_1 = L/c$, assuming the HNL travels at the speed of light, c. Figure 4.1 shows the resulting energy distributions and the decay length distribution, where it can be seen how the uniform cascade energies sum into a non-uniform total energy, and the decay length distribution is also non-uniform due to the uniform z sampling of both cascades, which sets the distance between them.

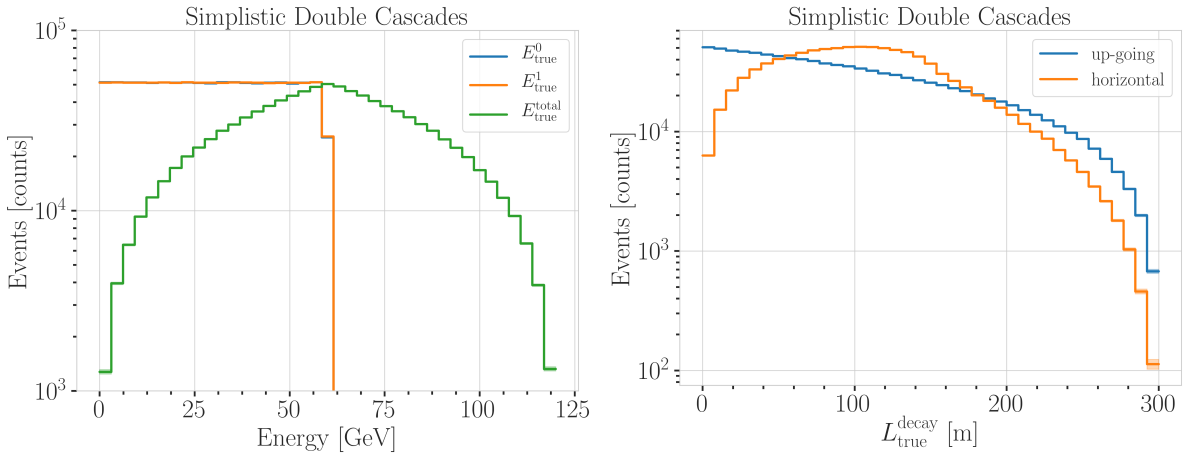

Figure 4.1: Generation level distributions of the simplistic simulation samples. Cascade and total energies (left) and decay lengths (right) of both samples are shown. The energy distributions are identical for both samples and therefore only shown once.

The second sample is used to investigate the worst-case scenario of horizontal events, where the spacing between DOMs is much larger. The cascades are placed uniformly on a circle with radius of $r = 150$ m centered in DeepCore at the depth of $z = -330$ m. The direction is always horizontal and azimuth is defined by the connecting vector of both cascade positions. The energies are again sampled uniformly between 0.0 GeV and 60.0 GeV. The specific sampling distributions/values for the cascades are listed in Table 4.1, for both samples, and for completeness, all distributions are shown in Figure A.2.

4.1.2 Realistic Sample

To thoroughly investigate the potential of IceCube DeepCore to detect double-cascade events, a more realistic simulation sample is produced that aims to be as close as possible to the expected signal simulation, while still allowing additional freedom to control the double-cascade kinematics.

Sample	Variable	Distribution	Range/Value
Up-going			
	energy	uniform	0.0 GeV to 60.0 GeV
	zenith	fixed	180.0°
	azimuth	fixed	0.0°
	x, y position	fixed	(41.6, 35.49) m
	z position	uniform	−480.0 m to −180.0 m
Horizontal			
	energy	uniform	0.0 GeV to 60.0 GeV
	zenith	fixed	90.0°
	azimuth	uniform	0.0° to 360.0°
	x, y position	uniform (circle)	c=(46.29, -34.88) m, r=150.0 m
	z position	fixed	−330.0 m

Table 4.1: Generation level sampling distributions and ranges/values of up-going and horizontal model-independent sample.

This sample is particularly useful for validating the model-dependent HNL simulation described in Section 4.2.

For this purpose the total energy is sampled from an E^{-2} power law, mimicking the energy spectrum of the primary neutrinos as stated in Section 4.3.1. The total energy is divided into two parts, by assigning a fraction between 0 % and 100 % to one cascade and the remaining part to the other cascade. This is a generic approximation of the realistic process, and chosen such that the whole sample covers various cases of energy distributions between the two cascades. The decay length is sampled from an exponential distribution, as expected for a particle decay. The resulting energy distributions and the decay length distribution are shown in Figure 4.2, where it can be seen that the individual cascade energies can be very small, due to splitting the total energy, and the decay lengths spans across several orders of magnitude.

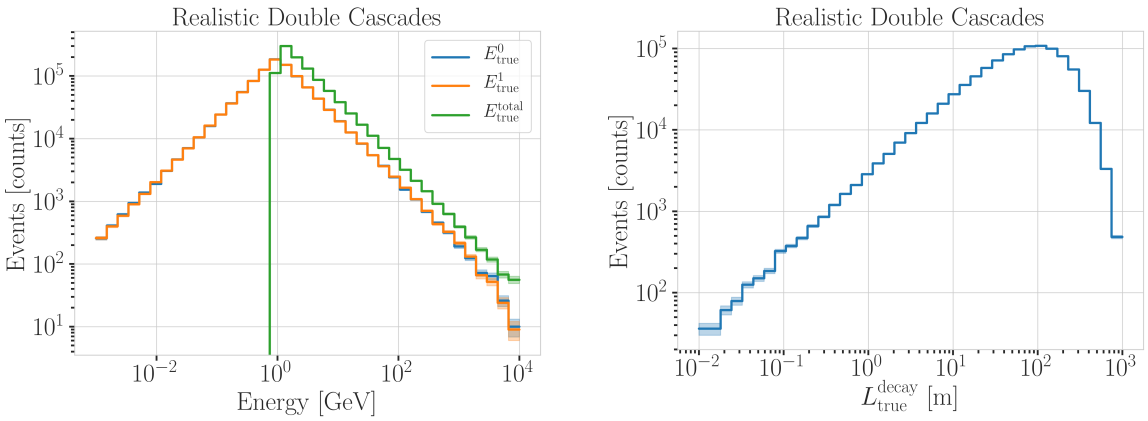

Figure 4.2: Generation level distributions of the realistic sample. Shown are the individual cascade energies and total energy (left) and decay lengths (right). It can be seen how the cascade energies can get very small, and the decay length follows a more realistic distribution spanning across several orders of magnitude.

To efficiently generate events in a way that produces distributions similar to what would be observed with DeepCore, one of the cascade positions is sampled inside the DeepCore volume by choosing its coordinates uniformly on a cylinder that is centered in DeepCore. This is similar to a trigger condition of one cascade always being inside the DeepCore fiducial volume. Choosing the direction of the event by sampling zenith and azimuth uniformly between 70° and 180° and 0° and 360°, respectively, the position of the other cascade can be inferred for a given decay length. This is done by assuming a travel speed of c, and choosing whether the cascade position that was sampled

is the first cascade or the second cascade with a 50 % chance. The zenith angle is chosen between straight up-going (zenith of 180°) and slightly down-going from above the horizon (70°) to mimic an event selection that reduces atmospheric muons by rejecting events coming from above the horizon, but still incorporates some down-going events. All distributions are shown in Figure A.2, and the sampling distributions/values are listed in Table 4.2.

Table 4.2: Generation level sampling distributions and ranges/values of the realistic model-independent simulation.

Variable	Distribution	Range/Value
energy (total)	power law E^{-2}	1 GeV to 1000 GeV
decay length	exponential $e^{-0.01L}$	0 m to 1000 m
zenith	uniform	70° to 180°
azimuth	uniform	0° to 360°
x, y (one cascade)	uniform (circle)	c=(46.29, -34.88) m, r=150 m
z (one cascade)	uniform	−480.0 m to −180.0 m

4.2 Model-Dependent Heavy Neutral Lepton Event Generation

To estimate the HNL event expectation in IceCube DeepCore, depending on the specific model parameters, a generator was developed that is based on the HNL theory introduced in Section 2.3. For this work, only the interaction with the τ-sector was taken into account ($|U^2_{\alpha 4}| = 0, \alpha = e, \mu$), which reduces the physics parameters of interest and relevant for the generation to the fourth heavy lepton mass, m_4, and the mixing, $|U^2_{\tau 4}|$.

Due to the very low interaction rate of neutrinos, which are the source of HNL production, the event generation is performed in a way that forces every event to interact in a chosen sampling volume. The weight of each event is then calculated as the inverse of the simulated neutrino fluence

$$w_{\text{gen}} = \frac{1}{F_{\text{sim}}} \frac{1}{N_{\text{sim}}} , \tag{4.1}$$

where F_{sim} is the number of neutrino events per energy, time, area, and solid angle, and N_{sim} is the number of simulated events. If this weight is multiplied by the livetime and the theoretically expected neutrino flux for a given physical model, it results in the number of expected events in the detector for this particular MC event.

The generator uses a customized *LeptonInjector (LI)* version to create the events and *LeptonWeighter (LW)* to weight them [107]. The modified LI and the essential components needed for the HNL simulation are described in the next sections, followed by the description of the weighting scheme and the sampling distributions chosen for the generation.

[107]: Abbasi et al. (2021), "LeptonInjector and LeptonWeighter: A neutrino event generator and weighter for neutrino observatories"

4.2.1 Custom LeptonInjector

In its standard version, the LI generator produces neutrino interactions by injecting a lepton and a hadronic cascade at the interaction vertex of the neutrino, where the lepton is the charged (neutral) particle produced in a CC (NC) interaction and the cascade is the hadronic cascade from the nucleus that is breaking apart. The hadronic cascade is stored as a specific

object of type *Hadrons*, which triggers the correct simulation of the shower development in the following simulation steps. Below 30 GeV the individual hadrons are simulated using GEANT4 [104] while for higher energies an analytical approximation from [100] is used. The main differences to an EM cascade is that part of the energy will not be observed, because it goes into neutral particles, and that the spatial development of the shower is different as discussed in Section 3.2.2. Both objects are injected with the same (x, y, z, t) coordinates and the kinematics are sampled from the differential and total cross-sections that are one of the inputs to LI.

[104]: Agostinelli et al. (2003), "Geant4—a simulation toolkit"

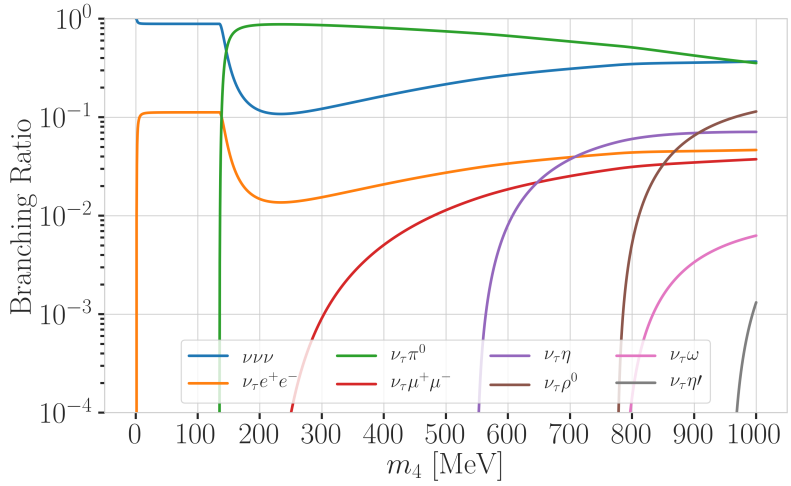

Figure 4.3: Branching ratios of the HNL within the mass range considered in this work, only considering $|U_{\tau 4}^2| \neq 0$, calculated based on the results from [80].

In the modified version, the SM lepton at the interaction vertex is replaced by the new HNL particle, where the interaction cross-sections are replaced by custom, mass dependentg HNL cross-sections. The HNL is forced to decay after a chosen distance[1] to produce secondary SM particles, where the decay mode is chosen with a probability given by the mass dependent branching ratios from the kinematically accessible decay modes shown in Figure 4.3. The cross-section and decay width calculations were implemented for this purpose and will be explained in more detail in the following. Another addition to LI is that the decay products of the HNL are also stored. These HNL daughter particles form the second cascade, not as a single hadronic cascade object, but as the explicit particles forming the shower. They are injected with the correctly displaced position and delayed time from the interaction vertex, given the HNL decay length. The kinematics of the two-body decays are computed analytically, while the 3-body decay kinematics are calculated with MADGRAPH4 (v3.4.0) [108], which will also be explained further below. Independent of the number of particles in the final state of the HNL decay, the kinematics are calculated/simulated at rest and then boosted along the HNL momentum.

1: The explicit sampling distributions and ranges can be found in Section 4.2.2.

Muons produced in those decays are propagated using PROPOSAL [109], also simulating their Cherenkov light output. The shower development of gamma rays, electrons, and positrons below 100 MeV is simulated using Geant4 and for higher energies the analytical approximation is used again [100].

[109]: Koehne et al. (2013), "PROPOSAL: A tool for propagation of charged leptons"

The injection is done using the LI *volume mode*, for the uniform injection of the primary particle on a cylindrical volume, adding 50 % of the events with ν_τ and the other half with $\bar{\nu}_\tau$ as primary particle types. The generator takes

the custom double-differential/total cross-section splines described below and the parameters defining the sampling distributions as inputs.

Cross-Sections

The cross-sections are calculated using the NuXSSplMkr [110] software, which is a tool to calculate neutrino cross-sections from *parton distribution functions (PDFs)* and then fit to an N-dimensional tensor-product B-spline surface [111] to produce the splines that can be read and used with LI/LW. The tool was modified to produce the custom HNL cross-sections, where the main modification to calculate the cross-sections for the ν_τ-NC interaction into the new heavy mass state is the addition of a kinematic condition to ensure that there is sufficient energy to produce the heavy mass state. It is the same condition fulfilled for the CC case, where the outgoing charged lepton mass is non-zero. Following [112] (equation 7), the condition

[111]: Whitehorn et al. (2013), "Penalized splines for smooth representation of high-dimensional Monte Carlo datasets"

[112]: Levy (2009), "Cross-section and polarization of neutrino-produced tau's made simple"

$$(1 + x\delta_N)h^2 - (x + \delta_4)h + x\delta_4 \leq 0 \tag{4.2}$$

is implemented for the NC case in the NuXSSplMkr code. Here

$$\delta_4 = \frac{m_4^2}{s - M^2} \,, \tag{4.3}$$

$$\delta_N = \frac{M^2}{s - M^2} \,, \text{and} \tag{4.4}$$

$$h \overset{def}{=} xy + \delta_4 \,, \tag{4.5}$$

with x and y being the Bjorken variables, m_4 and M the mass of the heavy state and the target nucleon, respectively, and s the center of mass energy squared. The custom version was made part of the open source NuXSSplMkr software and can thus be found in [110]. The result of this kinematic condition is that events cannot be produced for combinations of energy, x, y that do not have sufficient energy to produce the outgoing, massive lepton. This results in a reduction of the cross-section towards lower energies, which scales with the assumed mass of the HNL. This effect can be seen in Figure 4.4.

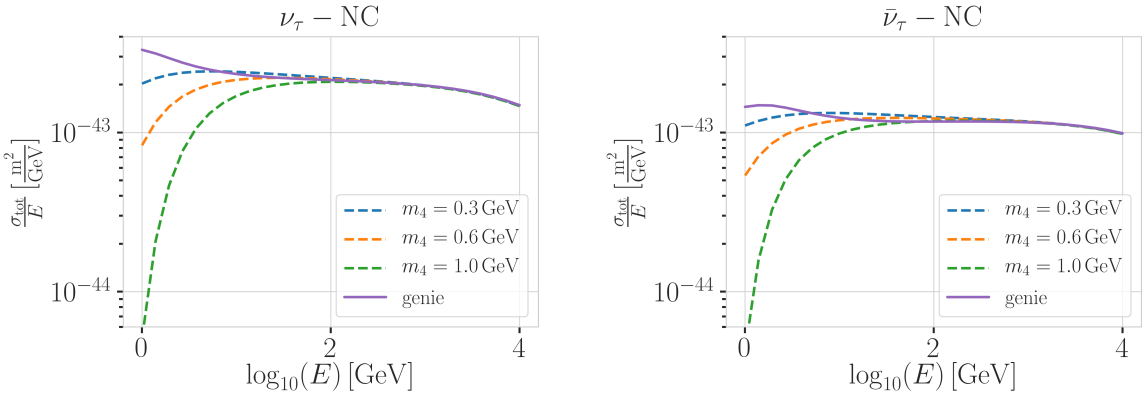

Figure 4.4: Custom HNL total cross-sections for the three target masses compared to the total ($\nu_\tau/\bar{\nu}_\tau$ NC) cross-sections used for SM neutrino simulation production with GENIE.

[113]: Glück et al. (1998), "Dynamical parton distributions revisited"

The GRV98LO [113] PDFs were added to the cross-section spline maker and

used to create the HNL cross-sections for consistency with the neutrino simulation. The double-differential ($d^2\sigma/dxdy$) and total (σ) cross-sections were produced for the chosen target HNL masses and then splined in energy, x, and y for $d^2\sigma/dxdy$, and in energy for σ. Figure 4.4 shows the total cross-sections that were produced compared to the cross-section used for the production of the SM $\nu_\tau/\bar{\nu}_\tau$ NC background simulation. They agree above $\sim 200\,\text{GeV}$, where the modification should not have any effect on the cross-sections. This is the desired result of using the identical input PDFs, and confirms that the unmodified cross-sections produced with NuXSSplMkr agree with the GENIE cross-sections.

Decay Channels

The accessible decay channels are dependent on the mass of the HNL and the allowed mixing. For this analysis, where only $|U_{\tau 4}|^2 \neq 0$, the decay channels considered are listed in Table 4.3 and the corresponding branching ratios are shown in Figure 4.3. The individual branching ratio for a specific mass is calculated as $\text{BR}_i(m_4) = \Gamma_i(m_4)/\Gamma_{\text{total}}(m_4)$, where $\Gamma_{\text{total}}(m_4) = \sum \Gamma_i(m_4)$. They can be seen in Figure 4.5, where the individual decay widths Γ_i are shown, which are computed using an implementation of the state-of-the-art calculations from [80]. The formulae for these calculations are explicitly listed in the following.

Channel	Opens
$\nu_4 \longrightarrow \nu_\tau \nu_\alpha \bar{\nu_\alpha}$	0 MeV
$\nu_4 \longrightarrow \nu_\tau e^+ e^-$	1 MeV
$\nu_4 \longrightarrow \nu_\tau \pi^0$	135 MeV
$\nu_4 \longrightarrow \nu_\tau \mu^+ \mu^-$	211 MeV
$\nu_4 \longrightarrow \nu_\tau \eta$	548 MeV
$\nu_4 \longrightarrow \nu_\tau \rho^0$	770 MeV
$\nu_4 \longrightarrow \nu_\tau \omega$	783 MeV
$\nu_4 \longrightarrow \nu_\tau \eta'$	958 MeV

Table 4.3: Possible decay channels of the HNL, considering only $|U_{\tau 4}|^2 \neq 0$, and the mass at which each channel opens.

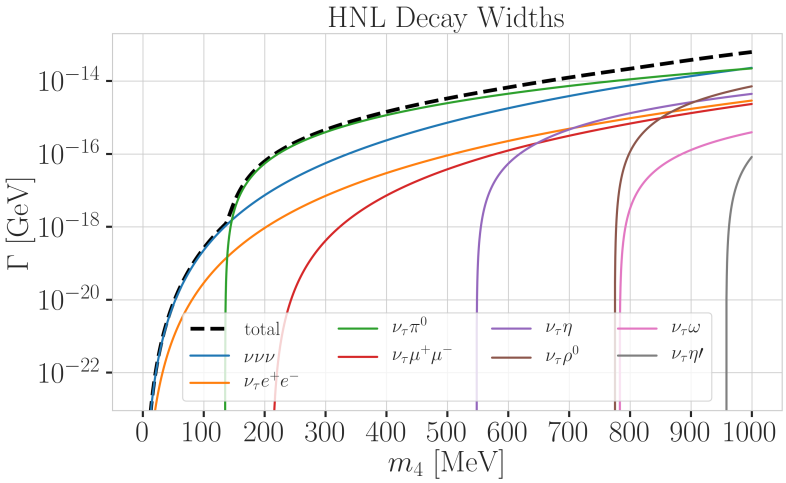

Figure 4.5: Decay widths of the HNL within the mass range considered, calculated based on the results from [80]. Given the existing constraints on $|U_{e4}|^2$ and $|U_{\mu 4}|^2$, we consider that the corresponding decay modes are negligible.

2-Body Decay Widths: The decay to a neutral pseudoscalar meson is

$$\Gamma_{\nu_4 \to \nu_\tau P} = |U_{\tau 4}|^2 \frac{G_F^2 m_4^3}{32\pi} f_P^2 (1 - x_p^2)^2 \,, \tag{4.6}$$

with $x_P = m_P/m_4$ and the *effective decay constants* f_P given by

$$f_{\pi^0} = +0.1300\,\text{GeV}\,, \tag{4.7}$$
$$f_\eta = +0.0816\,\text{GeV}\,, \text{and} \tag{4.8}$$
$$f_{\eta'} = -0.0946\,\text{GeV}\,, \tag{4.9}$$

while the decay to a neutral vector meson is given by

$$\Gamma_{\nu_4 \to \nu_\tau V} = |U_{\tau 4}|^2 \frac{G_F^2 m_4^3}{32\pi} \left(\frac{f_V}{m_V} \right)^2 g_V^2 (1 + 2x_V^2)(1 - x_V^2)^2 \,, \tag{4.10}$$

with $x_V = m_V / m_4$,

$$f_{\rho^0} = 0.171\,\text{GeV}^2 \,, \tag{4.11}$$

$$f_\omega = 0.155\,\text{GeV}^2 \,, \tag{4.12}$$

and

$$g_{\rho^0} = 1 - 2\sin^2\theta_w \,, \tag{4.13}$$

$$g_\omega = \frac{-2\sin^2\theta_w}{3} \,, \tag{4.14}$$

and $\sin^2\theta_w = 0.2229$ [114], where θ_w is the Weinberg angle.

[114]: Tiesinga et al. (2021), "CODATA recommended values of the fundamental physical constants: 2018"

3-Body Decay Widths: The (invisible) decay to three neutrinos, one of flavor τ and two of any flavor α, is

$$\Gamma_{\nu_4 \to \nu_\tau \nu_\alpha \bar{\nu_\alpha}} = |U_{\tau 4}|^2 \frac{G_F^2 m_4^5}{192\pi^3} \,, \tag{4.15}$$

while the decay to two charged leptons (using $x_\alpha = (m_\alpha / m_4)^2$) of the same flavor reads

$$\Gamma_{\nu_4 \to \nu_\tau l_\alpha^+ l_\alpha^-} = |U_{\tau 4}|^2 \frac{G_F^2 m_4^5}{192\pi^3} \left[C_1 f_1(x_\alpha) + C_2 f_2(x_\alpha) \right] \,, \tag{4.16}$$

with the constants defined as

$$C_1 = \frac{1}{4}(1 - 4\sin^2\theta_w + 8\sin^4\theta_w) \,, \tag{4.17}$$

$$C_2 = \frac{1}{2}(-\sin^2\theta_w + 2\sin^4\theta_w) \,, \tag{4.18}$$

the functions as

$$f_1(x_\alpha) = (1-14x_\alpha-2x_\alpha^2-12x_\alpha^3)\sqrt{1-4x_\alpha}+12x_\alpha^2(x_\alpha^2-1)L(x_\alpha) \,, f_2(x_\alpha) = 4[x_\alpha(2+10x_\alpha-12x_\alpha^2)\sqrt{1} \tag{4.19}$$

and

$$L(x) = \ln\left(\frac{1 - 3x_\alpha - (1 - x_\alpha)\sqrt{1 - 4x_\alpha}}{x_\alpha(1 + \sqrt{1 - 4x_\alpha})} \right) . \tag{4.20}$$

Analytical 2-Body Decay Kinematics

[21]: Workman et al. (2022), "Review of Particle Physics"

Following the review of [21], the 4-vector defining the kinematics of a particle is $p = (E, \vec{p})$, with its energy, E, and 3-momentum, $\vec{p}$. Squaring it gives the mass, $p^2 = E^2 - \vec{p}^2 = m^2$, while the velocity is $\vec{\beta} = \vec{p}/E$. If the HNL with mass m_4 decays into two particles with masses m_1 and m_2, their 3-momenta in the rest frame of the HNL are given by

$$|\vec{p}_1| = |\vec{p}_2| = \frac{\lambda^{1/2}(m_4^2, m_1^2, m_2^2)}{2m_4} \,, \tag{4.21}$$

where $\lambda(x, y, z) = x^2 + y^2 + z^2 - 2xy - 2xz - 2yz$. The energy of the particles is then given by

$$E_1 = \frac{m_4^2 + m_1^2 - m_2^2}{2m_4}\,, \tag{4.22}$$

and equivalently for E_2. The 4-vectors of the particle are then boosted to the lab frame, where the HNL is moving with velocity $\vec{\beta}$.

Simulated 3-Body Decay Kinematics

The 3-body decay kinematics cannot be computed analytically, instead, we employ MadGraph4 for this purpose. MadGraph is a tool to simulate particle collisions and decay processes, and is widely used in the high-energy physics community. The 3-body decay kinematics are calculated in the rest frame of the HNL, using decay diagrams calculated with FeynRules 2.0 [115] and the Lagrangians derived in [80] as input. The *Universal FeynRules Output (UFO)* from effective_HeavyN_Majorana_v103 were used for our calculation. For each mass and corresponding decay channels, we produce 10^6 decay kinematic variations in the rest frame and store those. During event generation, we uniformly select one of those events to simulate the decay kinematics of a 3-body decay.

[115]: Alloul et al. (2014), "FeynRules 2.0 - A complete toolbox for tree-level phenomenology"

[80]: Coloma et al. (2021), "GeV-scale neutrinos: interactions with mesons and DUNE sensitivity"

4.2.2 Sampling Distributions

Variable	Distribution	Range/Value
energy	E^{-2}	[2 GeV, 1×10^4 GeV]
zenith	uniform (in $\cos(\theta)$)	[80°, 180°]
azimuth	uniform	[0°, 360°]
vertex x, y	uniform (on circle)	r=600 m
vertex z	uniform	−600 m to 0 m
m_4	fixed	[0.3, 0.6, 1.0] GeV
L_{decay}	L^{-1}	[0.0004, 1000] m

Table 4.4: Generation level sampling distributions and ranges/values of the model-dependent samples.

In principle, the generation level sampling distributions should be chosen such that at the final level of the event selection chain the phase space relevant for the analysis is covered with sufficient statistics to make a reasonable estimate of the event expectation. Initial distributions insufficiently covering the phase space lead to an underestimation of the expected rates, because some of the events that would pass the selection are not produced. This limits the expected analysis potential. Three discrete simulation samples were produced with HNL masses of 0.3 GeV, 0.6 GeV, and 1.0 GeV. The remaining sampling distributions are identical for all samples and are listed in Table 4.4. The target number of events for each sample was 2.5×10^9 at generation to result in sufficient MC statistics at final level. Figure 4.6 shows the true cascade energies, which result from the custom interaction cross-sections and the decays discussed above. Note here that these are the full true energies going into the cascades. For the first cascade some energy goes into invisible particles produced in the hadronic shower development and for the HNL decay, there always is at least one invisible neutrino. Additional sampling distributions can be found in Figure A.3.

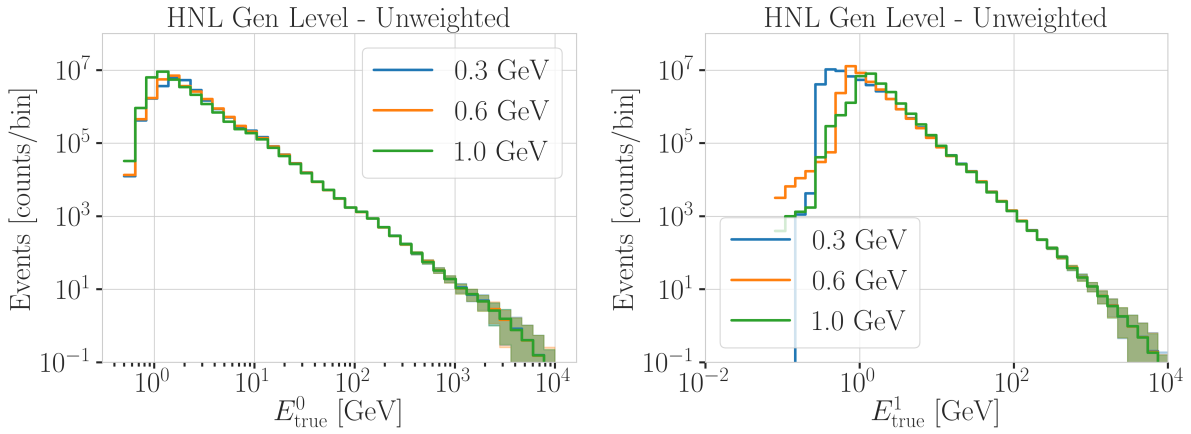

Figure 4.6: Generation level distributions of the model-dependent simulation. Shown are the true energies of both cascades including the energy that goes into invisible particles.

4.2.3 Weighting Scheme

Since the lab frame decay lengths/lifetimes of the events were sampled from an inverse distribution instead of an exponential, as it would be expected from a particle decay, we have to re-weight accordingly to achieve the correct decay length distribution. The re-weighting factor is calculated as the ratio of the probability density functions PDFs of the desired exponential distribution and the inverse distribution that was sampled from as $\frac{\text{PDF}_{\text{exp}}}{\text{PDF}_{\text{inv}}}$.

The inverse distribution in the rest frame of the HNL is given by

$$\text{PDF}_{\text{inv}} = \frac{1}{\tau \cdot (\ln(\tau_{\text{max}}) - \ln(\tau_{\text{min}}))}\,, \tag{4.23}$$

where τ is the rest frame lifetime and $\tau_{\text{min/max}}$ are the minimum and maximum values of the lifetime sampling range. Since the generation range is chosen in the lab frame, the rest frame lifetime range $[\tau_{\text{min}}, \tau_{\text{max}}]$ is defined by the lab frame decay length range $[s_{\text{min}}, s_{\text{max}}]$ as

$$\tau_{\text{min/max}} = \frac{s_{\text{min/max}}}{v \cdot \gamma}. \tag{4.24}$$

Here, the gamma factor is calculated for each event as

$$\gamma = \frac{\sqrt{E^2_{\text{kin}} + m^2_4}}{m_4}\,, \tag{4.25}$$

with the HNL mass, m_4, and its kinetic energy, E_{kin}, while v is the speed of the HNL which is calculated as

$$v = c \cdot \sqrt{1 - \frac{1}{\gamma^2}}\,, \tag{4.26}$$

where c is the speed of light.

The desired exponential distribution of the rest frame lifetime is given by

$$\text{PDF}_{\text{exp}} = \frac{1}{\tau_{\text{proper}}} \cdot e^{\frac{-\tau}{\tau_{\text{proper}}}}\,, \tag{4.27}$$

where τ_{proper} is the proper lifetime of each HNL event that is calculated using the total decay width, Γ_{total}. Since each individual decay width calculation includes a factor of $|U_{\tau 4}|^2$, accounting for the mixing between the HNL and the SM particles, the total decay width includes a scaling factor of ut4. The proper lifetime is then calculated as

$$\tau_{\text{proper}} = \frac{\hbar}{\Gamma_{\text{total}}(m_4)} \,, \tag{4.28}$$

where $\hbar$ is the reduced Planck constant.

This re-weighting factor is then calculated as

$$w_{\text{lifetime}} = \frac{\text{PDF}_{\text{exp}}}{\text{PDF}_{\text{inv}}} = \frac{\Gamma_{\text{total}}(m_4)}{\hbar} \cdot \tau \cdot (\ln(\tau_{\text{max}}) - \ln(\tau_{\text{min}})) \cdot e^{\frac{-\tau}{\tau_{\text{proper}}}} \,. \tag{4.29}$$

Adding a factor of $|U_{\tau 4}|^2$ to account for the mixing at the interaction vertex the total re-weighting factor becomes

$$w_{\text{total}} = |U_{\tau 4}|^2 \cdot w_{\text{lifetime}} \,. \tag{4.30}$$

If this additional weighting factor is multiplied to the generation weight introduced in Section 4.2 (in m^2), the livetime (in s), and the oscillated primary neutrino flux (in $\text{m}^{-2}\text{s}^{-1}$) it results in the number of expected events in the detector for this particular MC event for a specific mixing (and mass). The only required input is therefore the mixing strength $|U_{\tau 4}|^2$, since the mass is fixed for each sample. This re-weighting scheme allows to continuously vary the mixing strength and to estimate the expected event rate, which will be crucial for the analysis performed in Chapter 6.

4.3 Standard Model Event Generation

4.3.1 Neutrinos

The simulation volume is a cylinder centered in DeepCore with radius and height chosen such that all events possibly producing a signal are contained. The different sizes, chosen depending on energy and neutrino flavor, are shown in Table 4.5. The directions of the neutrinos are sampled isotropically and the energies are sampled from an E^{-2} power law. The number of simulated events is chosen such that the livetime is more than 70 years for each flavor. Neutrinos and antineutrinos are simulated with ratios of 70% and 30%, respectively, which is roughly the ratio expected from the atmospheric neutrino flux [82].

[82]: Honda et al. (2015), "Atmospheric neutrino flux calculation using the NRLMSISE-00 atmospheric model"

To simulate the neutrino interaction with the ice, the Genie event generator [116] (version 2.12.8) is used, resulting in the secondary particles and the kinematic and cross-section parameters. The GRV98LO PDFs were used as inputs, and the propagation of the secondary particles and of the shower development is performed identical to the description in Section 4.2.1 and produces the energy losses and event morphologies introduced in Section 3.2.

Table 4.5: Cylinder volumes used for GENIE neutrino simulation generation. Cylinder is always centered in DeepCore at $(x, y, z) = (46.29, -34.88, -330.00)$ m.

Flavor	Energy [GeV]	Radius [m]	Length [m]	Events/File	Files
$\nu_e + \bar{\nu_e}$	1-4	250	500	450000	650
	4-12			100000	
	12-100	350	600		
	100-10000	550	1000	57500	
$\nu_\mu + \bar{\nu_\mu}$	1-5	250	500	408000	1550
	5-80	400	900	440000	
	80-1000	450	1500	57500	
	1000-10000	550		6700	
$\nu_\tau + \bar{\nu_\tau}$	1-4	250	500	1500000	350
	4-10			300000	
	10-50	350	600	375000	
	50-1000	450	800	200000	
	1000-10000	550	1500	26000	

4.3.2 Muons

Atmospheric muons are generated on a cylinder surface enclosing the full IceCube detector array. The cylinder has a height of 1600 m and a radius of 800 m. The energy is sampled from an E^{-3} power law while the other sampling distributions (position, direction) are found from parameterizations based on [117]. This work uses full CORSIKA [118] simulations of muons to tailor the parameterizations, starting from *cosmic ray (CR)* interactions with atmospheric nuclei using the CR flux model from [119] and producing the muons applying the hadronic interaction model SIBYLL 2.1 [120]. After the generation, they are propagated through the ice with PROPOSAL producing photons, treating them exactly like the muons produced in the HNL and neutrino event generation.

[117]: Becherini et al. (2006), "A parameterisation of single and multiple muons in the deep water or ice"

[119]: Gaisser (2012), "Spectrum of cosmic-ray nucleons, kaon production, and the atmospheric muon charge ratio"

[120]: Engel et al. (2017), "The hadronic interaction model Sibyll – past, present and future"

Since the offline processing and selection steps described in Section 5.1.2 and Section 5.4 reduce the muon contamination to an almost negligible level, the statistical uncertainty on the number of expected muon events at the final selection level is large and therefore two separate samples of muon simulation are produced. **A first sample** is used to tune the lower level selection (up to Level 4), therefore including all events resulting from the above described generation. **A second sample** is then produced to estimate the muon contamination at higher levels (above Level 5). It only consists of muon events that pass through a smaller cylinder centered in DeepCore (height of 400 m and radius of 180 m), and additionally rejects events based on a KDE estimated muon density at Level 5 (in energy and zenith). This increased the simulation efficiency at Level 5 significantly, making it feasable to use this sample to estimate the muon contamination at higher levels.

4.4 Detector Simulation

The detector simulation is performed after the event generation, where the initial particles and the resulting photons and secondary particles from their propagation were produced. This part of the simulation chain is applied to all muon and neutrino simulation as well as the HNL signal simulation. The detector simulation can be split into two parts: the propagation of the

photons and the simulation of the detector response (including internal noise).

4.4.1 Photon Propagation

Any photon that was produced in the event generation is individually traced through the ice, simulating scattering and absorption processes. The propagation is done using CLSIM [121] which is an implementation of the *Photon Propagation Code (PPC)* [122] in OpenCL. It is optimized to be run efficiently on GPUs. The ice is modeled as a set of 10 m thick, almost horizontal layers with specific absorption and scattering lengths. The *South Pole ice (SPICE)* model [123] accounts for the layers being tilted by a small amount, due to the uneven surface of the bedrock below the glacier, and the absorption and scattering lengths having a non-uniformity with respect to the azimuth direction. Figure 4.7 shows the values of this model for the different depths, indicating the location of IceCube, DeepCore, and the dust layer.

[122]: Chirkin et al. (2019), "Photon Propagation using GPUs by the IceCube Neutrino Observatory"

[123]: Aartsen et al. (2013), "Measurement of South Pole ice transparency with the IceCube LED calibration system"

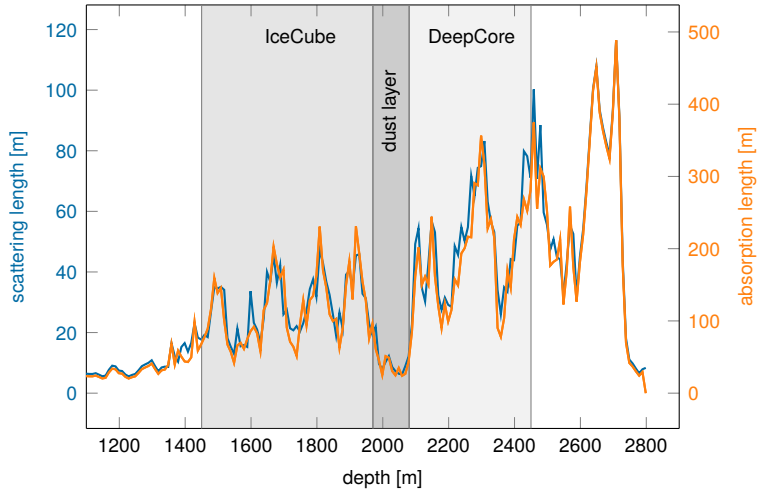

Figure 4.7: Scattering and absorption lengths as a function of depth in the SPICE model used for simulation. Modified from [19].

In an initial step, each photon's absorption length is sampled from an exponential distribution with the expectation value at the current layer's absorption length. The following propagation steps are performed in parallel for all photons. In each of those steps, corresponding to a single scattering event, the photon travels a length that is sampled from an exponential distribution with the expectation value at the scattering length of the current layer and the scattering angle chosen based on a combination of a simplified Mie scattering distribution [124] and a Henyey-Greenstein distribution [90, 125]. The parameters defining the shape of these distributions were calibrated using data from *in-situ* LED calibration runs. These steps are continuously repeated until each photon reaches a DOM or is absorbed[2]. After all photons have been propagated in that manner, the final step is to store the photons that reached a DOM for further processing.

[124]: Mie (1908), "Beiträge zur Optik trüber Medien, speziell kolloidaler Metallösungen"

[90]: Abbasi et al. (2022), "In-situ estimation of ice crystal properties at the South Pole using LED calibration data from the IceCube Neutrino Observatory"

[125]: Henyey et al. (1941), "Diffuse radiation in the Galaxy."

2: A photon is absorbed, when it traveled its full absorption length, sampled in the initial step of the photon propagation.

4.4.2 Detector Responses

The second part of simulating the IceCube detector is the DOM response. For a photon that reaches a DOM, the probability to produce a signal depends on the total efficiency and the angular acceptance of the specific DOM. The

total efficiency includes effects of the DOM glass, PMT quantum and photo-electron collection efficiencies, and it is wavelength dependent. Additionally, there is another angle dependent effect called *hole ice* [126]. This effect is due to varied ice properties resulting from the re-freezing process of the water column inside the borehole after deployment of the string. Accepted photons are converted into a so-called *Monte Carlo photo-electron (MCPE)*. The amount of charge measured for each MCPE is determined by sampling from the *single photo-electron (SPE)* distribution, which was tuned to match the observed distribution in each DOM in an *in-situ* calibration study [127]. Figure 4.8 shows the spread of the distribution measured over all DOMs compared to lab measurements of a specific PMT type. Based on the sampled charges and times of MCPEs, the voltage waveforms for the (two) different readout channels are simulated and passed on to the trigger simulation starting with WaveDeform (see Section 3.1.1).

[126]: Fiedlschuster (2019), "The Effect of Hole Ice on the Propagation and Detection of Light in IceCube"

[127]: Aartsen et al. (2020), "In-situ calibration of the single-photoelectron charge response of the IceCube photomultiplier tubes"

Parameter	Value
Therm. rate λ_{th}	180 Hz
Decay rate λ_{dec}	80 Hz
Decay hits η	8.5
Decay μ	4.3 $\log_{10}$(ns)
Decay σ	1.8 $\log_{10}$(ns)

Table 4.6: Typical parameter values used in the vuvuzela noise simulation. Averaged over all DOMs.

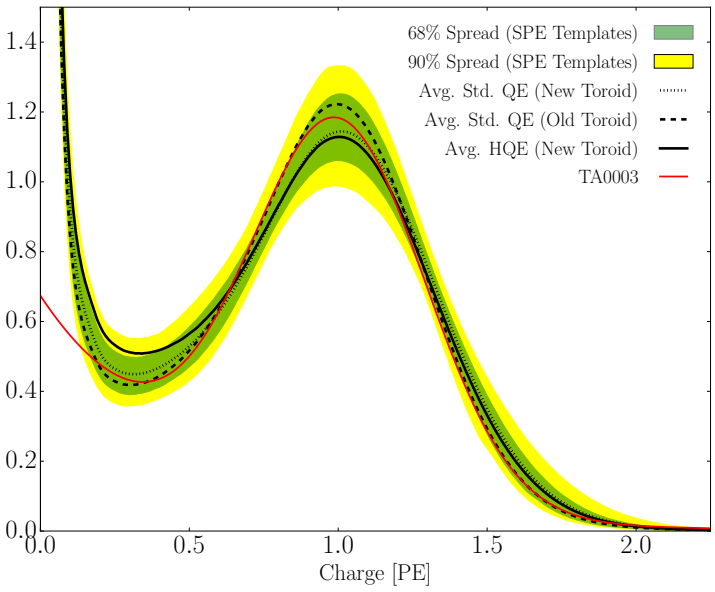

Figure 4.8: Single photo-electron charge distribution shown for a lab measurement in red (TA0003), various hardware configurations in black dashed, dotted, and solid lines, and the 68 % and 90 % spread of the measured charged templates for all DOMs. All curves are normalized to the same area. The figure is taken from [127].

Besides the Cherenkov photons, IceCube also observes photons that are produced in radioactive decays inside the DOMs, both in the glass housing sphere and the PMT glass itself. To simulate this internal noise, the *Vuvuzela* module [128, 129] is used to create additional MCPEs that are fed into the same simulation chain described above. The noise hits are simulated by drawing the times from a constant rate Poisson process and the number of photons from a Poisson distribution. Then the time differences between the individual photons per hit is found, based on a Log-Normal distribution. The simulation is defined by 5 parameters that are calibrated for each DOM individually. Table 4.6 shows the average values for these parameters.

[128]: Larson (2013), "Simulation and Identification of Non-Poissonian Noise Triggers in the IceCube Neutrino Detector"

[129]: Larson (2018), "A Search for Tau Neutrino Appearance with IceCube-DeepCore"

Event Processing and Reconstruction

5

The analysis presented in this thesis is highly dependent on an efficient filtering and event selection to reduce the raw IceCube trigger data to a usable atmospheric neutrino sample. Based on this selection, a precise estimation of both expected SM background and expected BSM signal events can be made using MC simulations. Starting from the PMT output, both data and simulation are processed through the in-ice trigger, the online filter and processing, and the low-energy event selection to produce a neutrino dominated sample. Once the sample is small enough for more sophisticated reconstruction techniques to be feasible to run, the events can be reconstructed with the existing IceCube reconstruction algorithms. At this level it is also possible to test and develop new reconstruction algorithms, without complications due to the large amount of background events from atmospheric muons and noise that are present before the filtering.

After describing the processing and filtering chain in Section 5.1, the development and performance of a dedicated low-energy double-cascade reconstruction algorithm is presented in Section 5.2. Based on the results from this reconstruction, the ability of the detector to observe and identify double-cascades is discussed in Section 5.3. Finally, the state-of-the-art SM neutrino event reconstruction is presented in Section 5.4, which is used to perform the analysis in this thesis.

5.1 Processing

After the detector simulation is performed, all MC and data are processed in exactly the same way. This section explains the trigger and event selection that is applied starting from the raw voltage measured by the PMTs. It is split in different steps that are run inside the ice, at the South Pole, and after the data was transferred to the North[1]. The complexity and computational cost of the processing increases with each step, while the total number of events reduces, making it feasible and reducing the use of computational resources on events that are not of interest for analyses.

1: Since the IceCube detector is at the South Pole, the data storage and processing sites in the Northern Hemisphere are shortly referred to as *the North*.

5.1.1 Trigger and Filter

Before the data can be sent to the North, the initial signal coming from the PMT is a voltage waveform that is digitized (for data) and then information of photon hits are extracted (also for the MC coming from the detector response simulation). The trigger and filter explained here are tailored to select events that pass through the DeepCore volume, while rejecting background events (either from atmospheric muons or from random noise). There are other filters used in IceCube which will not be explained here, since they are not relevant for this work. A full description of the instrumentation and the online systems can be found in [130].

[130]: Aartsen et al. (2017), "The IceCube Neutrino Observatory: Instrumentation and Online Systems"

In-ice Trigger

The trigger is applied inside the DOM in the ice before sending the information to the ICL on the surface. The time dependent voltage curves are captured if a pre-defined threshold value is exceeded. Once the threshold, set to the equivalent of 0.25 PE, is crossed, 6.4 µs of the waveform are coarsely digitized by a *Fast Analog-to-Digital Converter (FADC)* with a sampling rate of 40 MHz. Additionally, the first 427 ns are digitized using an *Analog Transient Waveform Recorder (ATWD)* with a sampling rate of 300 MHz [91], but only if some trigger condition is met, because this readout frequency is too high to be sampled directly and requires some buffering. For DeepCore, the HLC condition already mentioned in Section 3.1.1 has to be met for three DOMs inside the fiducial volume within a time window of 5 µs. If this is the case, all waveforms that crossed the threshold within a 20 µs time window around the trigger are digitized and sent to the ICL for further processing. This trigger is called DeepCore *Simple Multiplicity Trigger 3 (SMT-3)*. The DOM hits that are read out in this process, but do not meet the HLC condition, are called *soft local coincidence (SLC)* hits. The rate of the DeepCore SMT-3 trigger is ~250 Hz [6].

[91]: Abbasi et al. (2009), "The IceCube data acquisition system: Signal capture, digitization, and timestamping"

Online Filter

The digitized waveforms are sent to the ICL, where a further filter is applied *online*[2]. First, the WaveDeform algorithm is run to extract photon arrival times and charge from the waveforms. Next, the DeepCore filter is applied, which is an iterative hit cleaning starting from HLC hits and removing any hits outside a 125 m radius and a 500 ns time window (called *radius-time cleaning (RT-cleaning)*) of the initial hit. This mainly rejects unphysical SLC hits, which are potentially caused by random noise. All following selection steps are done using the resulting cleaned pulses.

2: Where *online* means running on hardware at the South Pole as opposed to *offline* at the IceCube institutions in the Northern Hemisphere.

An additional cut is applied to reject events that are likely to be caused by atmospheric muons. This is done by splitting the hits depending on whether they were inside the DeepCore fiducial volume or outside and then calculating the speed of each hit outside the fiducial volume towards the *center of gravity (COG)* of the hits inside. If one of them has a speed close to the speed of light, the whole event is rejected, because this is a strong indication for a muon event.

As input for the further selection levels, several event properties, such as vertex position and direction, are determined using fast and simple event reconstructions. After the DeepCore online filter is applied, the data rate is about 15 Hz, which can be sent to the North via satellite for further processing.

5.1.2 Event Selection

After the data was sent to the North, the *offline* filters and selections are applied to further reduce the background of atmospheric muons and noise. The selection is split into three levels referred to as *Level 3-5 (L3-L5)*, which bring down the muon rate to ~1 mHz, while the remaining fraction of random noise is below 1 %. The neutrino rate after this level is 2 mHz, making it a neutrino dominated sample. Assuming a HNL mass of 0.6 GeV

and a mixing of 0.1, the expected rate of HNL events after the selection is ~5 µHz. A more detailed investigation of the HNL selection efficiency is presented in Section 5.2.3.

Level 3

At the first offline filtering level, Level 3, one-dimensional thresholds are used to reduce atmospheric muons, pure noise, and coincident muons. This selection is targeting regions where the data/MC agreement is poor, so that more sophisticated *machine learning (ML)* techniques can be applied at later levels. The selection is made using 12 control variables, that are inexpensive to compute for the very large sample at this stage. The variables are related to position, time, and overall number of hits in the event.

Pure noise hits, that are temporally uncorrelated, are cleaned by applying a 300 ns sliding window, requiring the containment of more than 2 hits at its maximum. Additionally, an algorithm is run to check whether the hits show some directionality, accepting them only if they do.

To reduce the amount of muons a series of thresholds is applied using spatial and temporal information. Events that have more than 9 hits observed above −200 m or the first HLC hit above −120 m are rejected as well as events where the fraction of hits in the first 600 ns of the event is above 0.37, ignoring the first two hit DOMs. Additionally, the ratio between hits in the veto region and the DeepCore fiducial volume is required to be below 1.5.

If a muon enters the detector after the data acquisition was already triggered, it causes events that span over a much larger time range. To reduce those coincident events, the time difference between first and last pulse cannot be above 5000 ns. This cut mainly affects a region of very poor data to MC agreement, because coincident events are not simulated at all.

The L3 selection removes 95 % of the atmospheric muons and >99 % of pure noise hits, while keeping >60 % of the neutrino events. The sample now roughly contains muons/neutrinos/noise at a ratio of 100:10:1 with a total rate of ~0.5 Hz.

Level 4

After the total rate was reduced by the simple selection criteria at L3 and the overall agreement between data and MC is established, ML techniques can be applied to further reduce the background. For Level 4, two *Boosted Decision Trees (BDTs)* [131] classifiers are trained to separate neutrino events from atmospheric muons and noise hits, separately. The output of each classifier, a probability score, can be seen in Figure 5.1. The noise filter is applied first and an event passes, if the score is larger than 0.7, reducing the noise hits by a factor of 100, while keeping 96 % of neutrinos. Then the second BDT classifier is applied to reject muons. It was trained partly on unfiltered data, which consists of >99 % atmospheric muons, to reject the data and keeping the neutrinos from the simulation. Rejecting events with a score smaller than 0.65 removes 94 % of atmospheric muons while keeping 87 % of neutrinos. After applying the L4 selection, based on the BDT classifier outputs, the sample is still dominated by atmospheric muons, while the noise rate dropped to below most neutrino types.

[131]: Friedman (2002), "Stochastic gradient boosting"

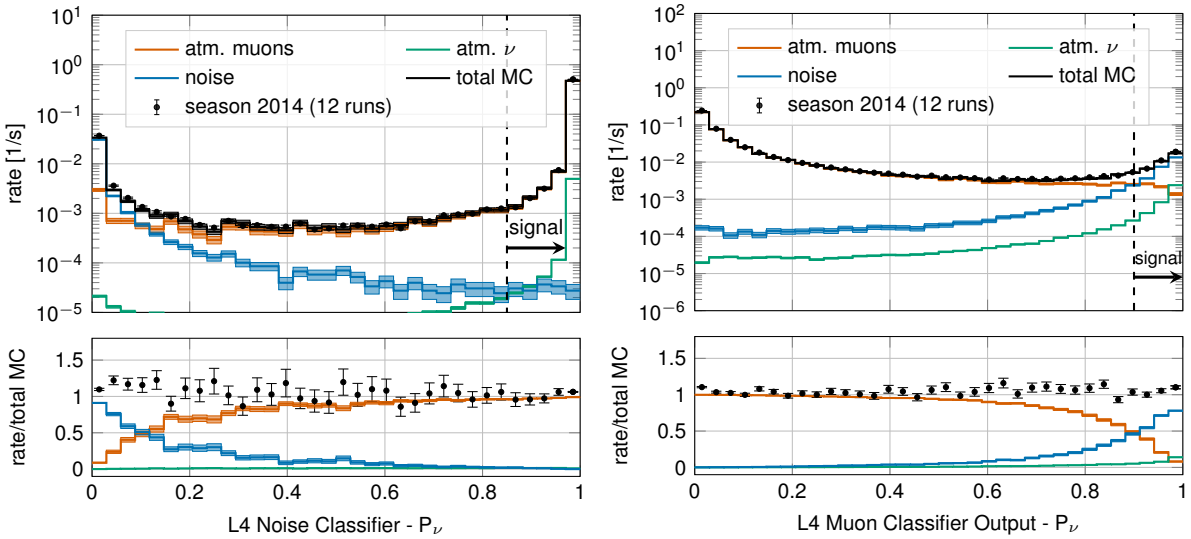

Figure 5.1: Distributions of Level 4 noise classifier output (left) and muon classifier output (right), where larger values indicate more neutrino-like and lower values more noise-like/muon-like. Taken from [132].

Level 5

Level 5 is the final selection level, before event reconstructions are applied. This level aims to reduce the remaining atmospheric muon rate below the rate of neutrinos. Muons not rejected by the earlier levels are those that produced little or no light in the veto regions. One possible reason is that they passed through one of the uninstrumented regions between the strings called *corridors*. To reject those, special corridor selection criteria are applied, which are based on the number of hits the event produced close to a potential corridor it passed through. The potential corridor in questions is identified based on a simple infinite track fit. In addition to the corridor selection, starting containment conditions are applied to reject events that start at the edge of the fiducial volume. Events with more than seven hits in the outermost strings of the detector or those that have a down-going direction in the uppermost region are rejected. This further reduces the fraction of muons by 96 % while keeping 48 % of neutrinos.

5.2 Double-Cascade Reconstruction

In the energy range relevant for this work, around 10s of GeV, the light deposition is very low and only a few DOMs detect photons, making event reconstructions difficult. Existing reconstruction algorithms applied for low-energy atmospheric neutrino events are either assuming a single-cascade hypothesis or a track and cascade hypothesis, which are the two SM morphologies observable at these energies, as was described in Section 3.3. A HNL being produced and decaying inside the IceCube detector however, will produce two cascade-like light depositions. The morphology, spatial separation between the cascades, and their individual properties depend on the model parameters discussed in Section 2.3.4. To investigate the performance of the detector to observe and identify these events, a low-energy double-cascade reconstruction algorithm was developed. It is based on a pre-existing algorithm used to search for double-cascades produced

from high-energy astrophysical tau neutrinos [133] that was established in [134, 135].

[133]: Abbasi et al. (2020), "Measurement of Astrophysical Tau Neutrinos in IceCube's High-Energy Starting Events"
[134]: Hallen (2013), "On the Measurement of High-Energy Tau Neutrinos with IceCube"
[135]: Usner (2018), "Search for Astrophysical Tau-Neutrinos in Six Years of High-Energy Starting Events in the IceCube Detector"

5.2.1 Table-Based Minimum Likelihood Algorithm

The double-cascade reconstruction is relying on a minimum likelihood algorithm, which is the *classical* approach to IceCube event reconstructions, as opposed to ML based methods. It compares the observed light depositions in the detector to the expected light depositions from a given event hypothesis, where the event hypothesis can be constructed from building blocks of single-cascade and track segment expectations. Varying the energies of the track segments and cascade components changes the light expectation and can be used to find the best fit hypothesis to the observed data. A Poissonian likelihood is constructed, which compares the observed photon numbers, n, with their arrival times to the expected light depositions, μ, for a given event hypothesis as

$$\ln(L) = \sum_j \sum_t n_{j,t} \cdot \ln\big(\mu_{j,t}(\Theta) + \rho_{j,t}\big) - (\mu_{j,t}(\Theta) + \rho_{j,t}) - \ln\big(n_{j,t}!\big) \ , \quad (5.1)$$

where ρ are the number of expected photons from noise, Θ are the parameters governing the source hypothesis, and the likelihood is calculated summing over all DOMs, j, splitting observed photons into time bins, t. The light expectations are calculated using look-up tables [111] that contain the results from MC simulations of cascade events or track segments. By varying the parameters defining the event hypothesis, the likelihood of describing the observed light pattern by the expected light depositions is minimized to find the reconstructed event. Algorithms of this kind, used in IceCube, are described in more detail in [92]. For the table production a specific choice of ice model has to be made, while the calibrated DOM information is taken from the measurement itself.

[111]: Whitehorn et al. (2013), "Penalized splines for smooth representation of high-dimensional Monte Carlo datasets"

[92]: Aartsen et al. (2014), "Energy Reconstruction Methods in the IceCube Neutrino Telescope"

Based on the tabulated light expectations for cascades and track segments, various hypotheses describing different event morphologies can be constructed. These are commonly the cascade only or the track and cascade hypotheses. The hypothesis describing the double-cascade signature of the HNL is using two cascades that are separated by a certain distance. The whole hypothesis is defined by 9 parameters and assumes that the two cascades are aligned with each other, which is a safe assumption for strongly forward boosted interactions and because low-energy cascades do not show a strong directionality. The parameters are the position of the first cascade, x, y, z, the direction of both cascades, ϕ, θ, and its time, t, as well as the decay length, L, between the two cascades. Assuming the speed of the HNL to be the speed of light, c, this already defines the full hypothesis, because the time and position of the second cascade are then fully determined by properties of the first cascade and the decay length. Note here, that the HNL particle does not produce any light while traveling, as it is electrically neutral. Since the likelihood only sums over DOMs that have observed photons, the non-observation of light is implicitly used as information and will exclude hypotheses with light expectation in those DOMs. The full 9 parameters describing an event are $\Theta = (x, y, z, t, \theta, \phi, E_0, E_1, L)$. To compute the full likelihood, the term in Equation 5.1, defined for a single event hypothesis, is summed over both cascade contributions, as $\sum_i \ln(L_i)$, with i being the cascade indices.

5.2.2 Optimization for Low Energies

Optimizing the double-cascade reconstruction for low-energy events was done in parallel to the development of the model-dependent simulation generator introduced in Section 4.2. A preliminary sample of HNL events from the model-dependent simulation was used, containing a continuum of masses between 0.1 GeV and 1.0 GeV and lab frame decay lengths sampled uniformly in the range from 5 m to 500 m. Even though this sample is not representative of a physically correct model and therefore not useful to predict the event expectation, it can still be used to optimize the reconstruction. The double-cascade nature of the individual events is present and the evenly spaced decay length distribution is especially useful for the purpose of optimizing the reconstruction.

The simulation is processed up to Level 5 of the selection chain described in Section 5.1.2 and one of the reconstructions from [136] is applied to the events, fitting a cascade and a track and cascade hypothesis. The results from this reconstruction are used as an input for the double-cascade reconstruction, where the position of the vertex, the direction of the event, and its interaction time are used as the input quantities for the first cascade, and the length of the track reconstruction is used as a seed for the distance between the two cascades. Several reconstructions were tested as seeds for the vertex position and the direction, but the choice did not significantly alter the results reported here.

[136]: Abbasi et al. (2022), "Low energy event reconstruction in IceCube DeepCore"

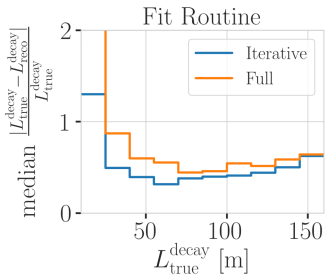

Figure 5.2: Decay length resolution as a function of the true decay length, comparing a full 9 parameters fit to an iterative approach where first the energies and the decay length are fit, while fixing the other 7 parameters and then the full fit is performed.

Fit Routine

The full 9 dimensional likelihood space is very complex and can have many local minima, depending on the specific event and its location in the detector. For this reason, a more sophisticated fit routine than fitting all 9 parameters at once was tested. In a first fit iteration, some parameters are fixed and the resulting best fit point is used to fit all 9 parameters in a second iteration. The effect is shown in Figure 5.2, which shows the median of the absolute, fractional decay length error with respect to the true decay length, for the full fit and an iterative fit routine. It can be seen how a fit split into two consecutive steps, where the first step fits only both cascade energies and the decay length and the second step fits the full 9 parameters, performs better as compared to a single, full 9 parameter fit. The initial seed remains identical for both the routines.

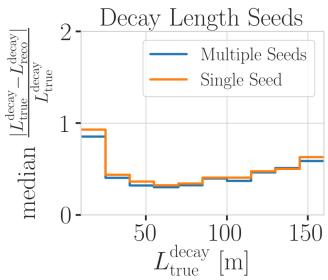

Figure 5.3: Decay length resolution as a function of the true decay length, comparing the same fit routine seeded with just the seed decay length and seeded with a decay length of 5 m, 25 m, 50 m, 100 m, and 200 m on the left.

Decay Length Seeds

From the seed values of the reconstruction, especially the length between the two cascades was found to have a very strong impact on whether the global minimum was found during the minimization. To mitigate this effect, multiple fits are performed, seeding with variations of the input length at different orders of magnitude. The best result is used, selected based on the total likelihood value of the best fit parameter set. A small improvement in the decay length resolution can be found by using this approach as compared to a single length seed. The resolutions for the differnt approaches are shown in Figure 5.3.

Minimizer Settings

To investigate the effect of the minimizer used to find the best fit parameters, the reconstruction was performed using three different minimizers, which were easily accessible within the reconstruction framework. The minimizers used were Minuit1 Simplex, Minuit2 Simplex, and Minuit2 Migrad [137]. As can be seen in Figure 5.4, Minuit1 Simplex performed best and was chosen as the default for the reconstruction. Global minimizers may improve the performance of the reconstruction, but were not available in the framework and would require significant software development.

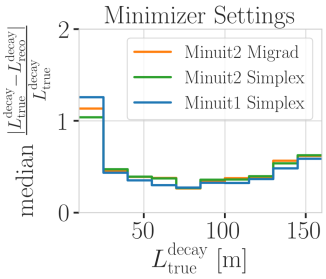

Figure 5.4: Decay length resolution as a function of the true decay length, comparing the same fit routine performed with different minimizers.

[137]: James et al. (1975), "Minuit: A System for Function Minimization and Analysis of the Parameter Errors and Correlations"

5.2.3 Performance

The optimization of the reconstruction was performed using preliminary development versions of the model-dependent HNL simulation. To investigate the effect of the low-energy event selection and the double-cascade reconstruction performance in a generic way, the model-independent simulation introduced in Section 4.1 is used. The important advantage of the model-independent samples is the controllable parameter space, especially in cascade energies and decay length, because the event kinematics are not coupled to the underlying HNL model, but can be chosen freely. This means that some benchmark edge cases can be investigated, and the performance can also be assessed for a realistic scenario in addition to mapping out the effects of the event selection and where the reconstruction breaks down.

The chosen final settings and procedures used for the low-energy double-cascade reconstruction algorithm are summarized in Table 5.1. In the first fit iteration, the number of time bins in Equation 5.1 is set to 1, so just the number of photons and their spatial information is used. In the second step the number of time bins is chosen such that each photon falls into a separate time bin, which means all time information is used. The average runtime per event is ~16 s on a single CPU core, but is very dependent on the number of photons observed in the event, since the likelihood calculation in the second step scales with this number and a table lookup has to be performed for each photon.

Type	Setting
Minimizer	Minuit1 Simplex
L_{decay} seeds	$(0.5, 1.0, 1.5) \cdot L_{\text{seed}}$
Fit routine	Iterative

Table 5.1: Chosen settings for the double-cascade reconstruction algorithm.

Best-Case Events

The best-case scenario to observe an event is to be directly on top of a string with a straight up-going direction. Using the simulation sample introduced in Section 4.1.1 and running the double-cascade reconstruction from Section 5.2 on these events, it is possible to estimate the performance limit of the reconstruction. Figure 5.5 shows one example event view from that sample, where the cascade energies are 2.4 GeV and 4.9 GeV, and the decay length is 65.8 m. It can be seen that despite the low energies, both cascades deposit light in the DOMs and the reconstruction is expected to work.

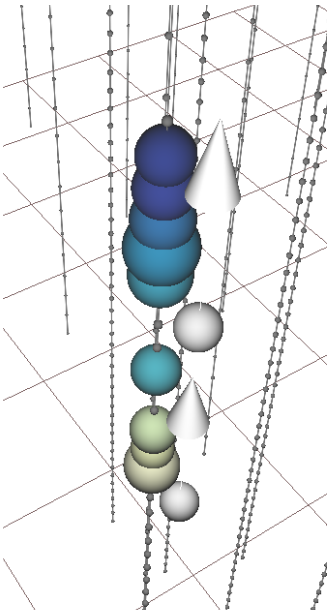

Figure 5.5: Event view of an up-going double-cascade event, with cascade energies of 2.4 GeV and 4.9 GeV, and a decay length of 65.8 m. The colored spheres show the DOMs that have observed light, where the size is proportional to the number of observed photons and the color indicates the time (yellow is early, blue is late). The strings are shown as black lines, with small spheres indicating the DOM positions, and the true cascade vertices and directions are shown as white spheres with white arrows.

The length resolution for events from this sample is shown in Figure 5.6. In the left part, the median resolution is shown to be below 30 % above a true decay length of ~10 m, and decreasing with increasing true length, down to ~10 % at 100 m. In the right part of Figure 5.6, the reconstructed decay length versus the true decay length is shown. The color scale shows the PDF along each (vertical) true decay length slice, which additional

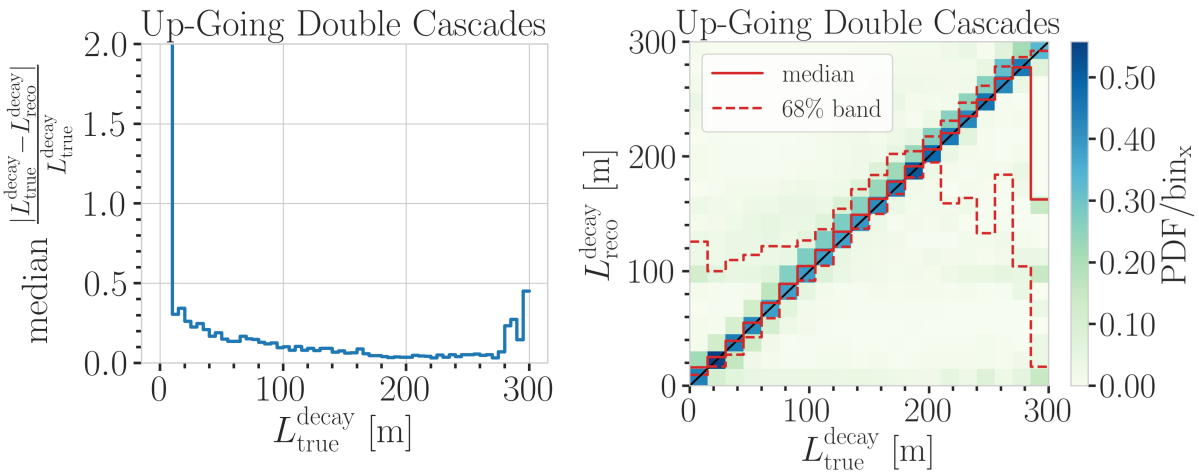

Figure 5.6: Decay length resolution of events from the up-going sample. Shown is the decay length resolution as a function of the true decay length (left) and the reconstructed decay length versus the true decay length (right), where the color scale is normalized per vertical slice and the median and 68 % band are shown in red.

information highlighted by the median and 68 % band shown in red (also per vertical column). The two-dimensional histogram shows that there is no under-estimation of the length up to a true decay length of ~210 m, which shows that if there are DOMs in the region between the two cascades that have not observed any light, the reconstruction is very stable. Considering the underlying Poisson likelihood in Equation 5.1 used for the reconstruction, this makes sense, since DOMs being present, but not observing any light is affecting the light expectation that goes into the likelihood and therefore makes these hypotheses incompatible with the data.

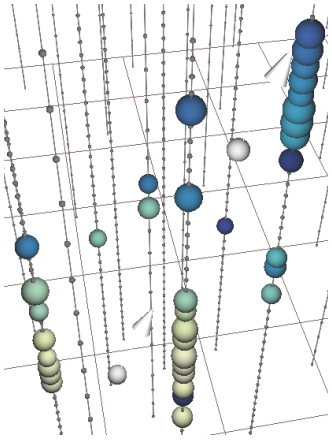

Figure 5.7: Event view of a realistic double-cascade event, with cascade energies of 30.8 GeV and 25.3 GeV, and a decay length of 144.5 m. The colored spheres show the DOMs that have observed light, where the size is proportional to the number of observed photons and the color indicates the time (yellow is early, blue is late). The strings are shown as black lines, with small spheres indicating the DOM positions, and the true cascade vertices and directions are shown as white spheres with white arrows.

Realistic Events

The sample of HNL events introduced in Section 4.1.2, which is a more realistic representation of the expected HNL events, but still offers more controlled energy and length distributions, is used to investigate the selection efficiency, to cross-check the reconstruction performance, and to benchmark the limits where the reconstruction breaks down. An example event view is shown in Figure 5.7, for cascade energies of 30.8 GeV and 25.3 GeV, and a decay length of 144.5 m. Since the size of the colored spheres is proportional to the number of photons observed in the DOMs, it can be seen from the event view that even for these higher energies, only individual or few photons are observed. This makes detecting and reconstructing them significantly more challenging and is purely due to the larger distance of the cascades from the DOMs.

Energy Resolutions: The energy resolutions are inspected by looking at the two-dimensional distributions of reconstructed energy versus the true energy. The results for the energies of the individual cascades are shown in Figure 5.8, where the color scale is again normalized per vertical slice, and the median and 68 % band are shown in red. For both cascades the reconstruction performs well above around 5 GeV to 7 GeV, with the median being on top of the diagonal and the spread being small. Below this energy, the reconstruction is over-estimating the true energy. This is because, on average, those low-energy events, passing the event selection, interact closer

to the DOMs and have an over fluctuation in their light deposition. This results in the observed energy bias. Interestingly, the second cascade energy reconstruction performs slightly worse, although they have the same energy ranges for this sample. This could hint at an asymmetry in the reconstruction process, which might be related to how the two cascades are parameterized, or be due to the different positions and the dominantly up-going direction used in the sampling combined with the DOMs looking down. Towards the higher energies, the statistics are decreasing, wich is due to the underlying energy distribution of the sample, which were shown in Figure 4.2.

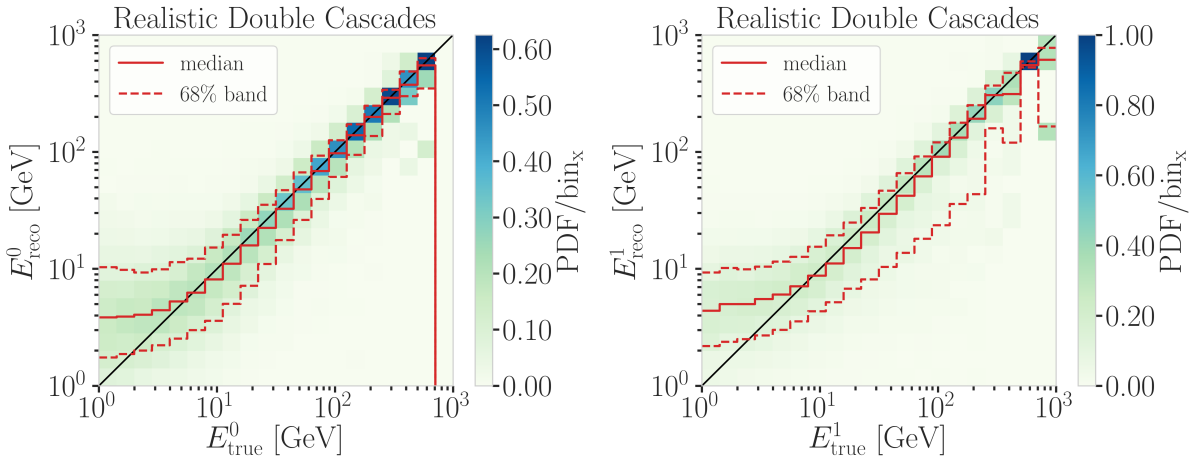

Figure 5.8: Energy resolutions of the realistic, model-independent simulation sample. Shown is the reconstructed energy versus the true energy for both cascades, where the color scale is normalized per vertical slice and the median and 68 % band are shown in red.

Decay Length Resolutions: The reconstructed decay length versus the true decay length is shown for all events in the left part of Figure 5.9. For short true decay lengths the reconstruction is over-estimating the length, while for long true decay lengths the reconstruction is strongly under-estimating the length. There is a region between true decay lengths of 15 m and 80 m where the median reconstruction is almost unbiased, but the 68 % interquartile range is wide with a lot of outliers towards short reconstructed lengths. Below 15 m the reconstructed lengths are always over-estimating the true length and above 80 m a population of events with short reconstructed length starts to dominate.

The over-estimation at small true decay lengths can be explained by multiple factors, one being that the shortest DOM spacing is ~7 m, vertically for DeepCore strings, but mostly larger than that, so resolving lengths below that is very challenging. The reconstruction tends to be biased towards estimating the length around where the light was observed. Additionally, approaching a length of 0.0, the reconstructed length will of course always be a one-sided distribution, because the lengths have to be positive.

The under-estimation at large true decay lengths is more puzzling. It seems like the distribution becomes bimodal in the reconstructed lengths. There is one well reconstructed population around the diagonal, and another badly reconstructed population at very short reconstructed lengths. Above 150 m the badly reconstructed population starts to dominate, and the median resolution drops off strongly. For these events, only one cascade was observed with enough light to be reconstructed, and the reconstruction describes the one observed cascade in two parts, separated by a short distance. The

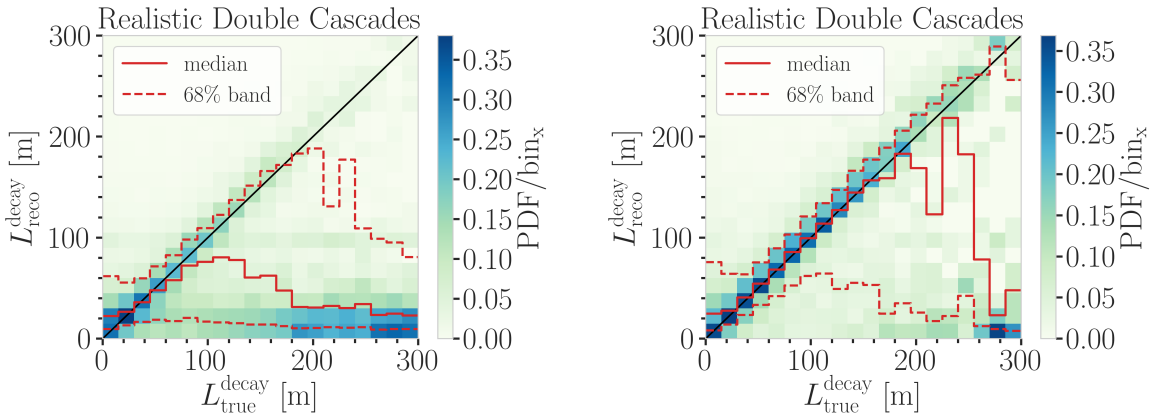

Figure 5.9: Length resolution of the realistic, model-independent simulation sample. Shown is the two-dimensional histograms of the reconstructed length versus the true length for all events (left) and for events with reconstructed cascade energies larger than 10 GeV (right), where the color scale is normalized per vertical slice and the median and 68 % band are shown in red.

result of applying a minimum energy cut on the reconstructed cascade energies ($E^0, E^1 \geq 10\,\text{GeV}$) is shown in the right part of Figure 5.9. It can be seen that the median resolution improves significantly, now aligning with the expectation between 15 m and 160 m. The spread also improves, but is still biased towards short reconstructed lengths and above 200 m the badly reconstructed population starts to dominate again.

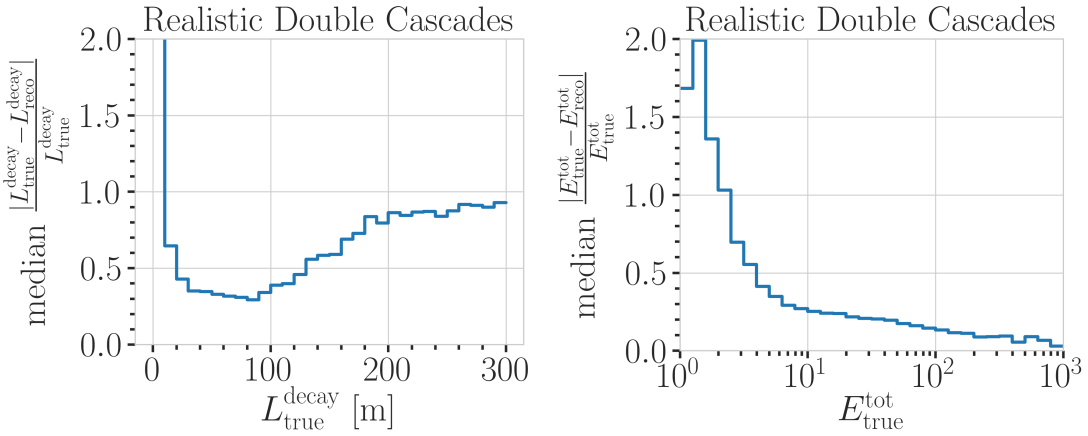

Figure 5.10: Decay length and total energy resolution of events from the realistic sample. Shown is the decay length resolution as a function of the true decay length (left) and the total energy resolution as a function of the true total energy (right).

Resolution Benchmarks: The left part of Figure 5.10 shows the median resolutions of the decay length as a function of the true decay length. It falls below 65 % above a true decay length of ~10 m, and starts to increase again with increasing true length around 100 m, where it is at 40 %. For larger true decay length, where the badly reconstructed population dominates, the resolution is large, stabilizing at around 90 % at 200 m. This is a significantly worse behavior than the performance found for the best-case event types shown in the left part of Figure 5.6. The total energy resolution versus the true total energy is shown in the right part of Figure 5.10. Above 4 GeV it is good and constantly improving with the true total energy. It falls below 30 % at 10 GeV and reaches 15 % at 100 GeV.

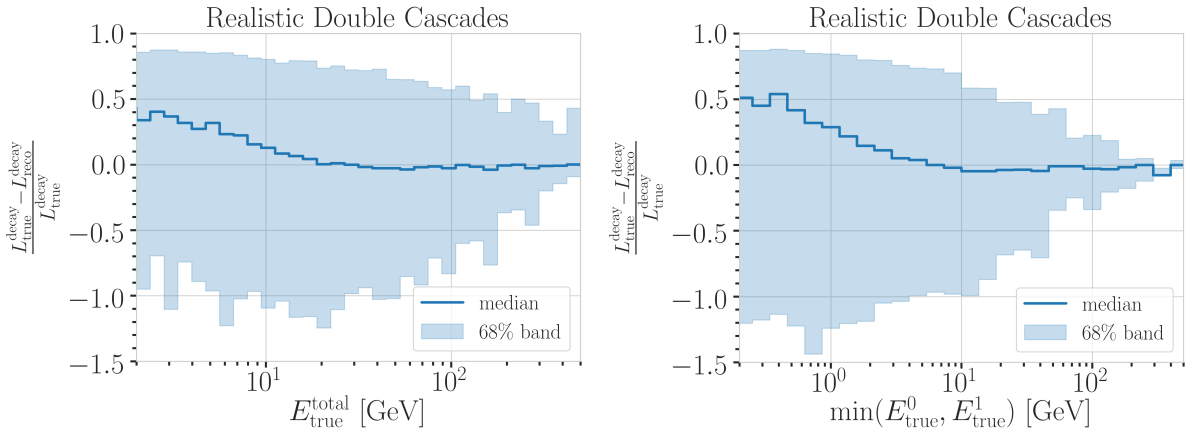

Figure 5.11: Decay length resolution of events from the realistic sample. Shown is the decay length resolution as a function of the true total energy (left) and as a function of the minimum true energy of the cascades (right).

To get an estimate of what minimum energies are necessary for the reconstruction to perform reasonably well, the fractional decay length resolution is shown as a function of the total true energy and the minimum energy of both individual cascades in Figure 5.11. In the left part it can be seen that the median of the decay length resolution stabilizes around 0 for a total energy above 20 GeV, but the spread of the distribution is still quite large with a 68 % band of 80 % to 100 %, decreasing down to ~60 % at 100 GeV. The right part of the figure shows the decay length resolution as a function of the minimum true energy of the cascades. The decay length resolution starts to be unbiased for a minimum energy of any cascade of 7 GeV, with an equivalently large spread. A rough takeaway from this is that the decay length reconstruction is not reliable for events with one cascade energy below 7 GeV and with a total energy below 20 GeV. Above these values the median resolution is roughly unbiased, but the spread is still large, decreasing with increasing energy.

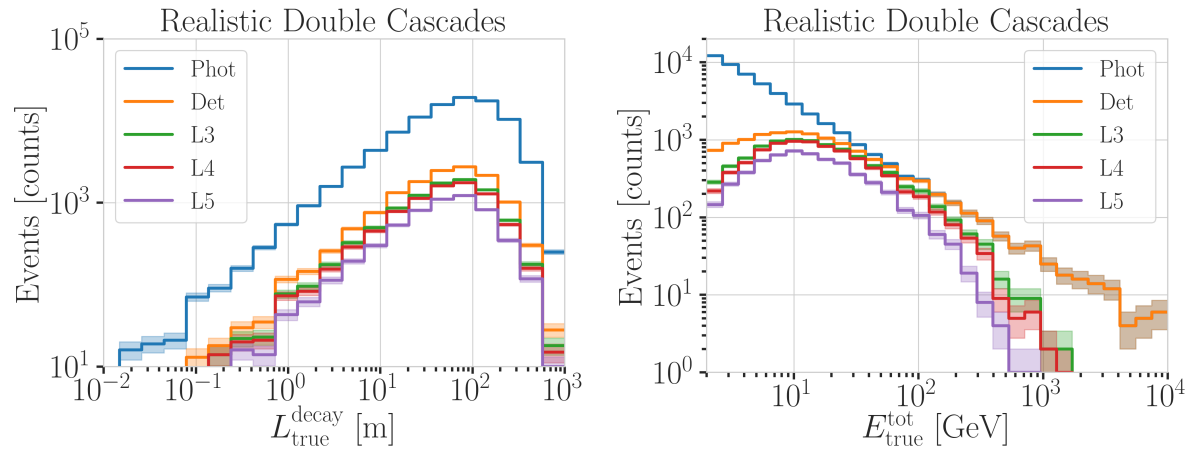

Figure 5.12: Selection efficiency of the realistic double-cascade sample. Shown is the true decay length distribution across the different selection levels (left) and the true energy distribution across the different selection levels (right).

Selection Efficiency: To assess the efficiency of the low-energy event selection for double-cascade events, the true energy and true decay length distributions are shown across the different selection levels in Figure 5.12.

The two detector simulation steps explained in Section 4.4 are also included, where the application of the detector response simulation (Det), reduces the events significantly at low energies, because only events with sufficient photons observed in the DOMs are kept. The L3 selection, which includes the DeepCore SMT-3 trigger, reduced both the low-energy region further, while also affecting the high-energy region. L4 and L5 reduce the overall number of events, without showing a specific energy dependence. The full selection appears to be independent of the true decay length, as the distributions reduces uniformly across the decay length range. Similar to the efficiency for SM neutrinos, the total selection efficiency from the online filter to L5 is around 40 %.

Model-Dependent Sample

After optimizing the double-cascade reconstruction and benchmarking how it performs using the model-independent sample, the resolutions are investigated with the model-dependent HNL simulation. A preliminary sample of HNL events is used which contains masses between 0.1 GeV and 3.0 GeV and lab frame decay lengths in the range from 1 m to 1000 m, sampled from an inverse distribution.

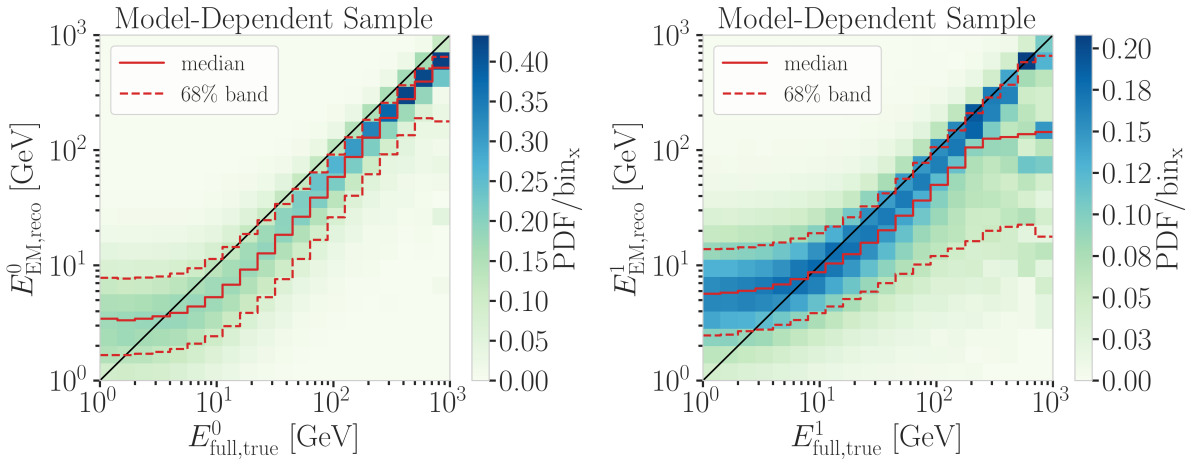

Figure 5.13: Reconstructed (EM) energy versus true energy (full) energy for the first cascade (left) and second cascade (right) for a preliminary version of the model-dependent sample, where the color scale is normalized per vertical slice and the median and 68 % band are shown in red.

The reconstructed energy versus the true energy is shown in Figure 5.13. The reconstructed energy is only the energy that was deposited as light in the detector. The true energies however, are the total cascade energies, including contributions that go into neutral particles that do not produce any light. It is therefore expected that the reconstructed energy is lower than the true and the median is offset with respect to the diagonal.

Apart from this expected bias, the behavior is similar to the results observed for the realistic, model-independent sample shown in Figure 5.8. The performance appears to be worse for the second cascade, but for this sample, the energy distributions of the cascades are very different. Due to the kinematics of HNL production and decay introduced in Section 2.3.4, the energy distribution of the second cascade is shifted to lower energies with respect to the energy distribution of the first cascade. Figure 5.14 shows the energy distributions of both cascades for the same events shown in Figure

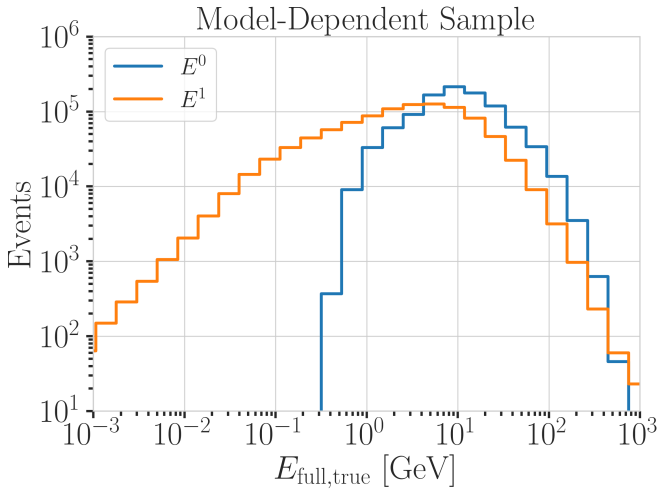

Figure 5.14: True energy distributions of both cascades for a preliminary version of the model-dependent sample. The shown energies are the full energy of the cascades, including components that go into invisible particles.

5.13. The energies of the first cascade peak around 10 GeV and the lowest values are at the order of 0.3 GeV, while for the second cascade, the peak of the distribution at ~4 GeV and the lower end of the distribution extends multiple orders of magnitude below that. Note here, that these are again the true, total energies of the cascades, including the contributions that go into invisible particles. The true deposited energies are therefore lower.

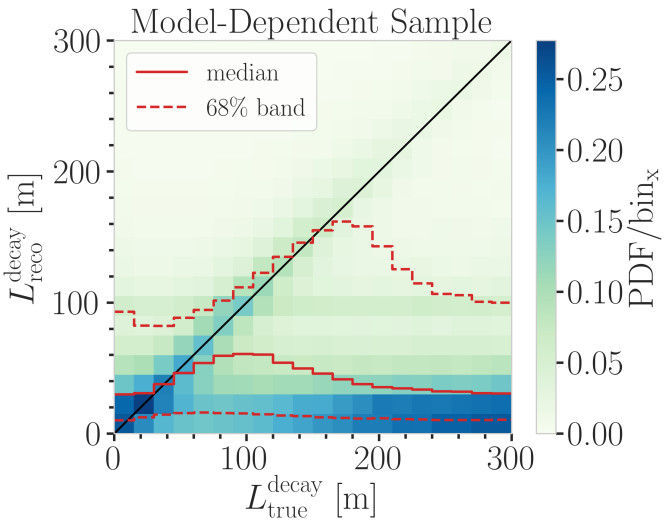

Figure 5.15: Reconstructed decay length versus true decay length for a preliminary version of the model-dependent sample, where the color scale is normalized per vertical slice and the median and 68 % band are shown in red.

The reconstructed decay length versus the true decay length is shown in Figure 5.15. The same behavior as observed for the realistic, model-independent sample shown in Figure 5.9 is seen. For short true decay lengths the reconstruction is over-estimating the length, while for long true decay lengths the reconstruction is strongly under-estimating the length and a population of badly reconstructed events is dominating at long true decay lengths.

Summary and Outlook

A double-cascade reconstruction was optimized for low-energy HNL events inside the DeepCore volume. A thorough investigation of the performance revealed a number of difficulties in reconstructing these events. The most

challenging cause is the missing information for the reconstruction due to the low light depositions. For the simulation using physically accurate models, this was especially bad, because part of the event's energy goes into neutral particles, which produce no light in the detector. From the investigation of the double-cascade reconstruction performance, it can be concluded that the main reason for the bad reconstruction is the low-energy of the second cascade. Other factors, like the position of the cascades in less densely instrumented regions of the detector also contribute at a lower level.

It may be possible to improve the performance through more sophisticated reconstruction techniques. Also, the reduced spacing and segmented directionality of optical modules in the future IceCube Upgrade detector should enhance the light detection of low-energy cascades and should yield a better chance to identify the unique HNL signature. Data taking for this new low-energy extension is expected to begin in 2026.

5.3 Double-Cascade Classification

Despite the failure of the reconstruction for events with low energy depositions, there is still a population of well reconstructed events. The next step is to see how well these can be distinguished from the SM backgrounds. For this purpose a classifier was trained to distinguish between HNL *signal* events and SM neutrino *background* events. To mitigate the poorly reconstructed events, a selection was applied to make sure the classifier is trained on well reconstructed events. The selection criteria require a minimum reconstructed energy of both cascades of 5 GeV and a minimum reconstructed decay length of 40 m. The same criteria are applied to both signal and background events.

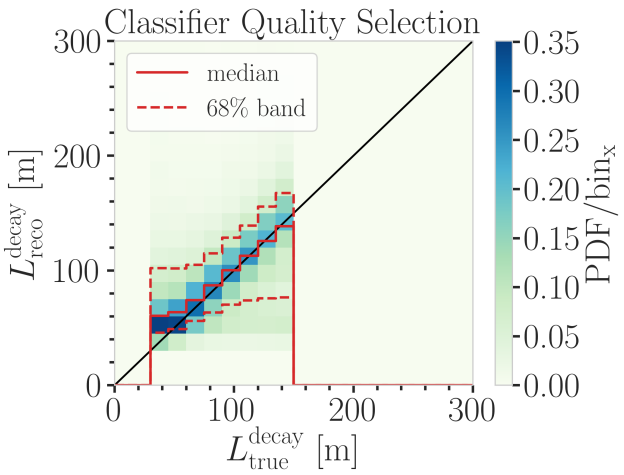

Figure 5.16: Reconstructed decay length versus true decay length for a preliminary version of the model-dependent sample, after the quality selection was applied. The color scale is normalized per vertical slice and the median and 68 % band are shown in red.

Additionally, some requirements on the true energies and decay length were applied for the signal, which are a minimum true energy of both cascades of 5 GeV, and a true decay length between 40 m and 150 m. These were chosen to make sure the HNL events were theoretically double-cascade-like and at a sensible length scale inside DeepCore. Figure 5.16 shows the reconstructed decay length versus the true decay length after the selection was applied.

The classifier used was a BDT from the *scikit-learn (sklearn)* package [138] and the input features are taken from the double-cascade reconstruction explained in Section 5.2 as well as some additional variables from earlier levels of the processing explained in Section 5.1. Figure 5.17 shows the distributions of two example input features, where the left plot shows the output probability of the classifier trained to distinguish track from single-cascade-like events, which is used in the oscillation analysis, and the right plot shows the reconstructed decay length from the double-cascade reconstruction. Shown are the distributions for the signal, the individual track and cascade background components, and the total background. The distributions are normalized to the same area to show their shapes and it can be seen that the signal and total background distributions look very similar, while there is some differences to the background split in track and single-cascade component. For completeness, the selected features and their importances for the results presented in the following are shown in Section B.1.

[138]: Pedregosa et al. (2011), "Scikit-learn: Machine Learning in Python"

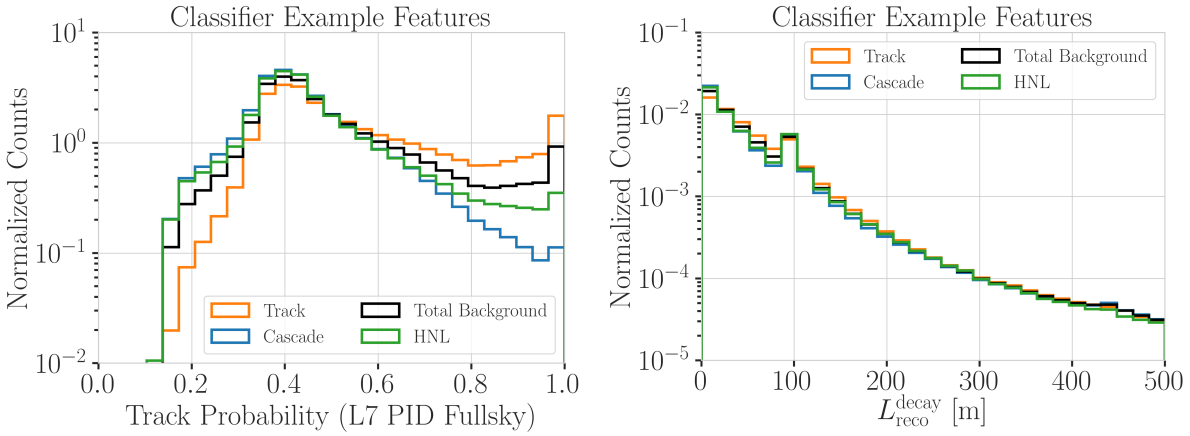

Figure 5.17: Example features used for the double-cascade classification. Shown is the output probability of the classifier trained to distinguish track from cascade-like events (left) and the reconstructed decay length from the double-cascade reconstruction (right) for the different background signatures, the total background, and the signal. Distributions are normalized to.

A *single-classifier* and *double-classifier* approach were tested. For the single-classifier, one BDT classifier was trained to distinguish between signal events and all background events at once. For the double-classifier, two classifiers were trained separately, one to distinguish signal from track-like background, and the other to distinguish signal from cascade-like background. The classifiers were trained with uniform weights, but scaled so that the summed weights for signal and background were equal. Since the SM neutrino events at these energies are either track-like or cascade-like, the double-classifier approach performed better and will be discussed here. Despite the fact that several combinations of features were tested, it was not possible to identify a pure double-cascade region with a single classifier. Since the results did not show a strong classification power, tuning the hyperparameters quickly lead to overtraining and the results here are using the default settings of the BDT classifier.

By applying the two classifiers trained to distinguish signal from track and signal from cascade, it is possible to select a region with only signal events. This is visualized in Figure 5.18, where the probabilities of 1 implies very signal like, and only the regions close to 1 are shown for both outputs, to highlight where a pure HNL sub-sample can be selected. When physical

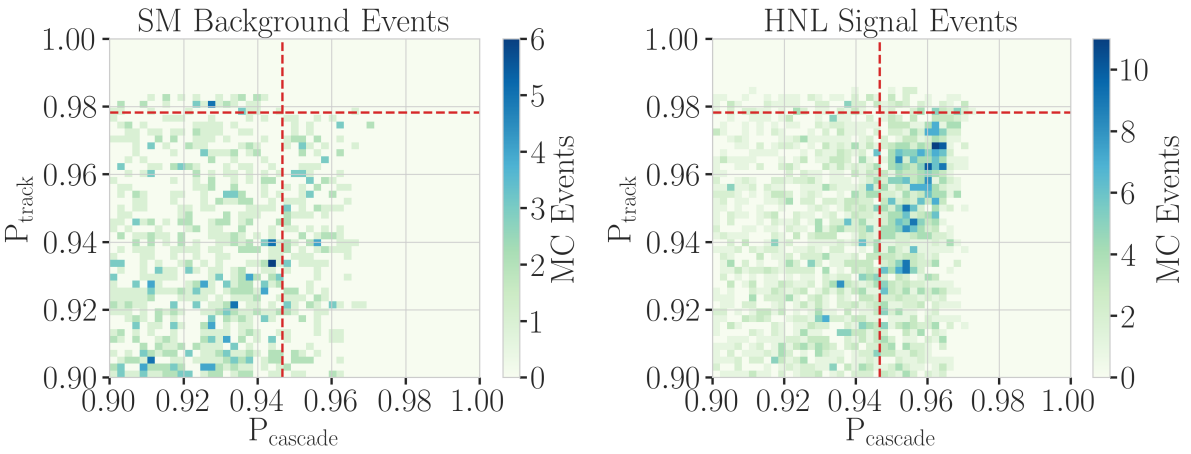

Figure 5.18: Output probabilities of the two classifiers trained to distinguish signal from track-like background and signal from cascade-like background. Shown are the MC event counts in the probability region close to 1, which means more signal like.

weights are applied to those signal events however, the expected event rate is very low, and even by assuming a highly optimistic mixing of 1, it would take more than 20 years of data taking to observe a single event. Applying a weaker signal selection criterion will contain a large amount of background events, which dominate over the signal at $\sim$ 2 orders of magnitude for a mixing of 0.1. With the current selection and reconstruction chain and a classical BDT, it is not possible to distinguish double-cascade events from the SM background.

5.4 Analysis Reconstruction

The reconstruction algorithm used in this work is a method that applies a *convolutional neural network (CNN)*. It is both used to reconstruct the events properties and to determine some discriminating quantities. The latest muon neutrino disappearance result from IceCube [139] is based on this reconstruction.

[139]: Yu et al. (2023), "Recent neutrino oscillation result with the IceCube experiment"

5.4.1 Fast Low-Energy Reconstruction using Convolutional Neural Networks

As the name *Fast Low-Energy Reconstruction using Convolutional Neural Networks (FLERCNN)* already indicates, the FLERCNN reconstruction [140] [141] is a CNN optimized to reconstruct IceCube events at low energies (<100 GeV) in a fast and efficient manner, by leveraging the approximate translational invariance of event patterns within the detector. The architecture of the network is very similar to the preexisting IceCube CNN event reconstruction [142], but optimized on low-energy events and specifically tailored to include the DeepCore sub-array. Only the eight DeepCore strings and the central 19 IceCube strings are used for the reconstruction (compare to Figure 3.4). Because of the different z-positions of the DeepCore and IceCube DOMs, they are divided into two networks that are combined in the final layer of the network. The full architecture is shown in Figure 5.19. The first dimension of the network is the string index, while the second dimension is the order of the DOMs along the vertical axis. The horizontal position of the DOMs is not

[140]: Yu et al. (2021), "Direction reconstruction using a CNN for GeV-scale neutrinos in IceCube"

[142]: Huennefeld (2017), "Deep Learning in Physics exemplified by the Reconstruction of Muon-Neutrino Events in IceCube"

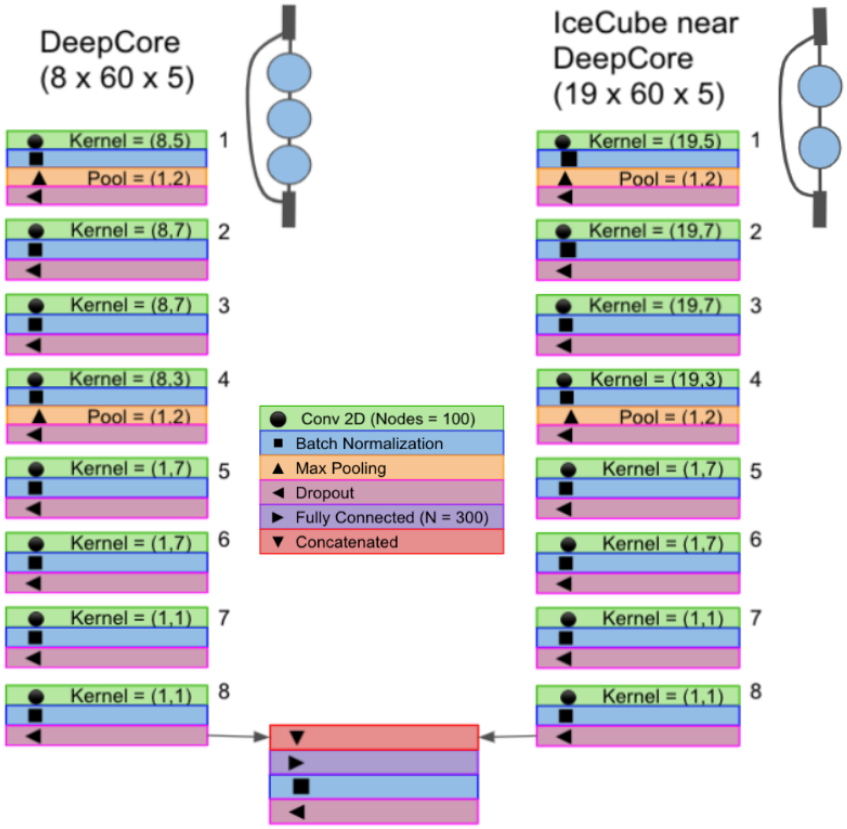

Figure 5.19: Architecture of the FLERCNN neural networks, taken from [140].

used, since the strings are arranged in an irregular pattern. The information from the DOM hits is summarized into five charge and time variables, which make up the last dimension of the input layer. The variables are the total summed charge, the time of the first hit, the charge weighted mean time of the hits, the time of the last hit, and the charge weighted standard deviation of the hit times.

Five different networks are trained using this architecture. Three networks do the regression of the events' energy, cosine of the zenith angle, and the starting vertex (x, y, z position), while two of them are used for classification. One is trained to predict the probability of the event being a ν_μ-CC event and the other to predict the probability of the event being an atmospheric muon. Each network is trained with a MC sample modified to have a flat distribution in the target variable, to be unbiased for that variable and ideally extending outside the target reconstruction region. For the classification tasks the loss function is the *binary cross entropy* and the activation function is a *sigmoid*. To perform the regression of zenith and vertex position, the loss function is the *mean squared error (MSE)*, while for the energy it is the *mean absolute percentage error*. The activation for all regression tasks is *linear*.

Figure 5.20 shows the energy resolution of the FLERCNN reconstruction for muon neutrinos, compared to the performance of a classical, likelihood based reconstruction. It can be seen that the CNN based reconstruction is less biased and performs better up to ~70 GeV. The resolution for electron neutrinos is shown in Section B.2.

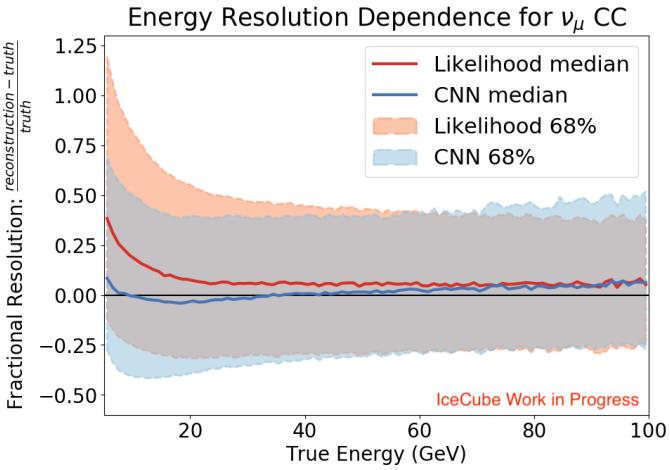

Figure 5.20: Energy resolution of the FLERCNN reconstruction for muon neutrinos, compared to the performance of a classical, likelihood based reconstruction. Shown is the median fractional energy resolution and the 68 % band as a function of the true energy.

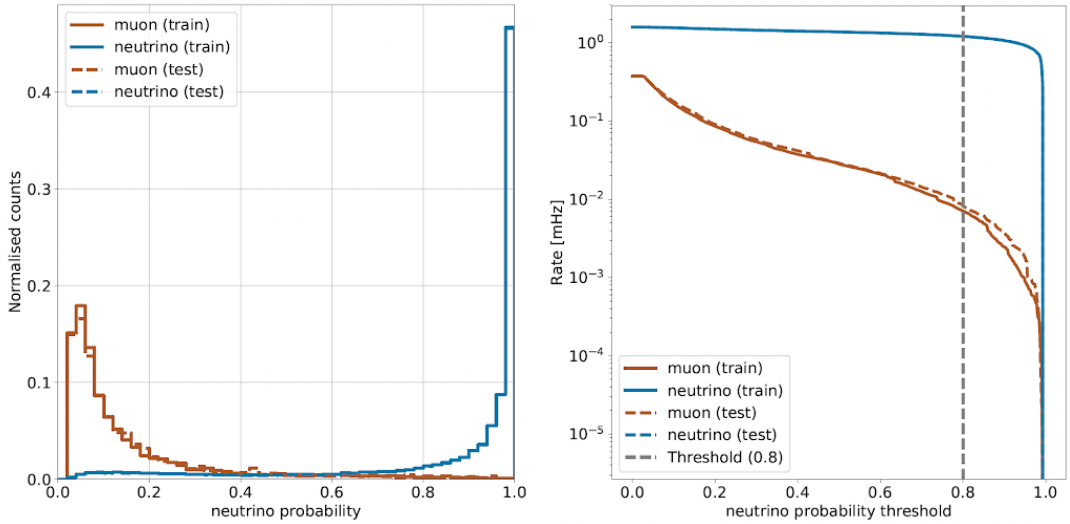

Figure 5.21: FLERCNN muon classifier output score (left) and rate of neutrinos and muons as function of muon classifier cut (right).

5.4.2 Analysis Selection

After the FLERCNN reconstruction is applied, a BDT classifier is used to further reduce the muon background for the final sample. The BDT is trained on five high level variables, where three are FLERCNN reconstruction variables (vertex z, ρ_{36}[3], and muon probability), and two are lower level variables (L4 muon classifier output and L5 corridor cut variable). To train the BDT, the FLERCNN nominal simulation set is used, only using events with $\cos(\theta) \leq 0.3$. The output of the BDT is the neutrino probability and a cut at 0.8 is applied to reject events with a high probability of being a muon. Figure 5.21 shows the output of the BDT classifier, where the neutrinos in both training and testing sets are gathered at 1 and muons are around 0, which shows great classification power. Since the probabilities for training and test sets are very similar, the BDT is not overtrained. The rate of neutrinos and muons as a function of the muon classifier probability threshold is shown in the right plot of Figure 5.21, where it can be seen that at the chosen value of 0.8, the neutrino rate is two orders of magnitude above the muon rate.

To get the final, pure sample of well reconstructed neutrinos a final selection is

3: A radial variable that is often used in IceCube, is the horizontal distance to string 36 called ρ_{36}, which is basically the distance to the center of IceCube.

applied. Parts of it are aiming to reject events with poor reconstruction quality, by requiring the events to fall into the DeepCore volume, where the denser, better instrumented detector leads to enhanced resolution. Conditions are applied on the vertex z and ρ_{36} and are listed in Table 5.2. The FLERCNN reconstruction was optimized for atmospheric neutrino analyses which are mainly in the region below 100 GeV and there are very few events with energies below 5 GeV, so the reconstructed energy is required to be in that range. Additionally, rejecting events with fewer than seven hits in the selected DOMs used for FLERCNN showed to increase the resolution.

Parts of this selection are applied to make sure the agreement between data and MC is good. To remove coincident muon and neutrino events, the number of hits in the top 15 layers of IceCube DOMs and the number of hits in the outermost IceCube strings are required to be above 0.5 and 7.5, respectively. Coincident random noise events are removed by requiring more than three hit DOMs from direct photons[4] [136]. Neither of the two coincident event types are simulated, which can be seen as bad agreement between data and MC. Lastly, the cosine of the reconstructed zenith angle is required to be smaller than 0.04 to reject down-going muons.

4: *Direct photons* are photons that were not scattered on their way from the interaction vertex to the DOM.

Table 5.2: Selection criteria for the final analysis sample. They are partly aiming to increase the data/MC agreement, while others are rejecting events with poor reconstruction quality.

Variable	**Threshold**	**Removed**
Number of hit DOMs	≥ 7	1.05 %
Radial distance	< 200 m	0.09 %
Vertical position	-495 m $< z < -225$ m	5.48 %
Energy	5 GeV $< E <$ 100 GeV	20.70 %
Cosine of zenith angle	< 0.04	19.66 %
Number of direct hits	> 2.5	10.50 %
Number of hits in top layers	< 0.5	0.03 %
Number of hits in outer layer	< 7.5	0.001 %
Muon classifier score	≥ 0.8	23.90 %

Search for Tau Neutrino Induced Heavy Neutral Lepton Events

6

This chapter describes the search for HNL events using 10 years of IceCube DeepCore data. The expected number of HNL events in the data sample depends on the mass of the additional heavy state, m_4, and the mixing element $|U^2_{\alpha 4}|$, with $\alpha = e, \mu, \tau$, between the SM flavors and the new mass state. As discussed in Section 2.3, this work focuses on the mixing to the tau sector, $|U^2_{\tau 4}|$, which has the weakest constraints to date. Since the mass itself influences the production and decay kinematics of the event and the accessible decay modes, individual mass samples were produced as described in Section 4.2. The mass influences the decay length and energy distributions, while the mixing both changes the overall expected rate of the HNL events and the shape in energy and length. We perform three independent searches for each mass sample, where the mixing is measured in each of the fits.

The analysis itself is performed by comparing the MC distributions to the observed data. To produce the physically expected distributions, the MC events are weighted given a specific choice of physics and nuisance parameters. By binning them and calculating a loss function comparing the bin expectations to the data, the physics and nuisance parameters, that best correspond to the observed data, are estimated by minimizing this loss function.

6.1 Final Level Sample

The final level simulation sample of this analysis consists of one of the three HNL samples explained in Section 4.2 and the neutrino and muon MC introduced in Section 4.3, while the data are the events measured in 10 years of IceCube DeepCore data taking. All simulation and the data are processed through the full event selection chain described in Section 5.1 and Section 5.4 leading to the final level sample. Event triggers consisting purely of random coincidences induced by noise in the DOMs have been reduced to a negligible rate, and will not be discussed further.

To get the neutrino expectation, the MC events are weighted according to their generation weight introduced in Section 4.3.1, multiplied by the total lifetime, and the expected neutrino flux. For the correct expectation at the detector, the events have to be weighted by the oscillation probability, depending on their energy and their distance traveled from the atmosphere to the detector. The oscillation probabilities are calculated using a python implementation of the calculations from [143], which use the matter profile of the Earth following the *Preliminary Reference Earth Model (PREM)* [144] as input. Apart from the energy and the distance, the two relevant parameters defining the oscillation probabilities are the atmospheric neutrino oscillation parameters θ_{23} and Δm^2_{31}. Since the HNL events originate from the tau neutrinos that were produced as muon neutrinos in the atmosphere and then oscillated into ν_τ, this weighting is also applied to the HNL events, in

[143]: Barger et al. (1980), "Matter effects on three-neutrino oscillations"
[144]: Dziewonski et al. (1981), "Preliminary reference Earth model"

addition to the specific weighting scheme described in Section 4.2.3, which itself is defined by the mixing $|U_{\tau 4}^2|$.

6.1.1 Expected Rates/Events

The rates and the expected number of events for the SM background are shown in Table 6.1 with around 175000 total events expected in the 10 years. Only data marked as good is used for the analysis, where *good* refers to measurement time with the correct physics run configuration and without other known issues. The resulting good detector livetime in this data taking period was 9.28 years. The rates are calculated by summing the weights of all events in the final level sample, while the uncertainties are calculated by taking the square root of the sum of the weights squared. The expected number of events is calculated by multiplying the rate with the livetime. The individual fractions show that this sample is neutrino dominated where the majority of events are ν_μ-CC events.

Table 6.1: Final level rates and event expectation of the SM background particle types.

Type	**Rate** [mHz]	**Events** (9.28 years)	**Fraction** [%]
ν_μ^{CC}	0.3531	103321 ± 113	58.9
ν_e^{CC}	0.1418	41490 ± 69	23.7
ν^{NC}	0.0666	19491 ± 47	11.1
ν_τ^{CC}	0.0345	10094 ± 22	5.8
μ_{atm}	0.0032	936 ± 15	0.5
total	0.5992	175332 ± 143	100.0

Table 6.2 shows the rates and expected number of events for the HNL samples. The expectation depends on the mass and the mixing and shown here are two example mixings for all the three masses that are being tested in this work. A mixing of 0.0 would result in no HNL events at all. It can already be seen that for the smaller mixing of $|U_{\tau 4}|^2 = 10^{-3}$ the expected number of events is very low, while at the larger mixing of $|U_{\tau 4}|^2 = 10^{-1}$ the number is comparable to the amount of atmospheric muons in the background sample.

Table 6.2: Final level rates and event expectations of the HNL signal for all three masses and two example mixing values.

HNL mass	**Rate** [μHz]	**Events (in** 9.28 years**)**
$\lvert U_{\tau 4}\rvert^2 = 10^{-1}$		
0.3 GeV	3.3	975 ± 2
0.6 GeV	3.1	895 ± 2
1.0 GeV	2.5	731 ± 2
$\lvert U_{\tau 4}\rvert^2 = 10^{-3}$		
0.3 GeV	0.006	1.67 ± 0.01
0.6 GeV	0.022	6.44 ± 0.01
1.0 GeV	0.025	7.27 ± 0.01

6.1.2 Analysis Binning

Table 6.3: Three-dimensional binning used in the analysis. All variables are from the FLERCNN reconstruction explained in Section 5.4.

Variable	N_{bins}	**Edges**	**Spacing**
P_ν	3	[0.00, 0.25, 0.55, 1.00]	linear
E	12	[5.00, 100.00]	logarithmic
$\cos(\theta)$	8	[-1.00, 0.04]	linear

An identical binning to the analysis performed in [139] is used. In total, there are three bins in PID (cascade-like, mixed, and track-like), 12 bins in reconstructed energy, and 8 bins in cosine of the reconstructed zenith angle as specified in Table 6.3.

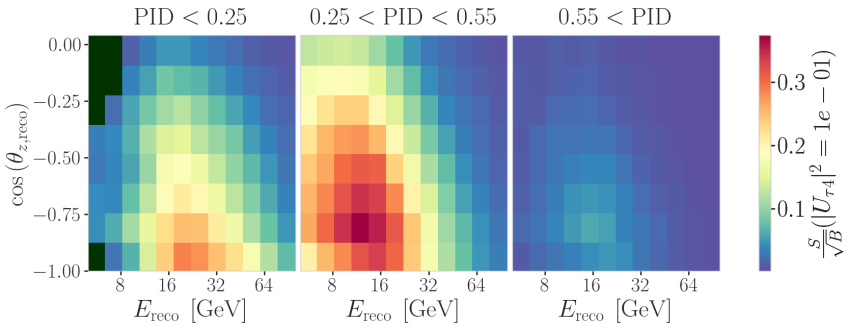

Figure 6.1: Signal over square root of background expectation in 9.28 years for the 1.0 GeV mass sample at a mixing of 0.1, while all other parameters are at their nominal values.

Extending the binning towards lower energies or increasing the number of bins in energy or cosine of the zenith angle did not improve the HNL sensitivities significantly, because the dominant signal region is already covered with a sufficiently fine binning to observe the shape and magnitude of the HNL events on top of the SM background. This can be seen in the middle panel of Figure 6.1, which shows the expected signal events divided by the square root of the expected background events for every bin used in the analysis. The signal expectation is of the 1.0 GeV mass sample at a reference mixing of 0.1, with the corresponding three-dimensional histogram shown in Figure C.1. Both the nominal background expectation used to calculate the signal to square root of background ratio and the detector data can be seen in Figure 6.2.

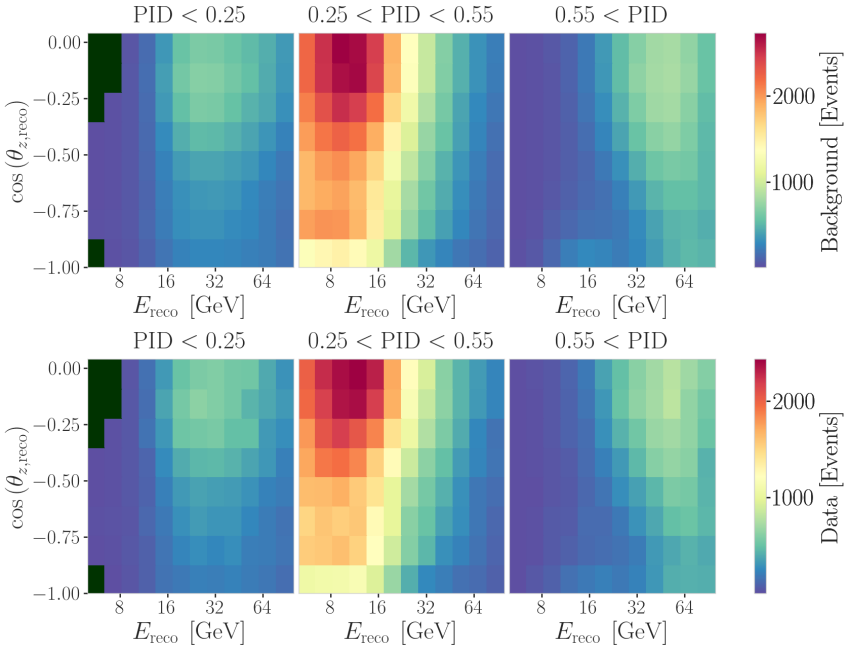

Figure 6.2: Background expectation in 9.28 years for all other parameters are at their nominal values (top) and observed data (bottom).

Some low energy bins in the cascade-like region have very low MC expectations (<1 event) and are therefore not taken into account in the analysis, to prevent unwanted behavior in the fit. Those are shown in dark green in the three-dimensional histograms, and both background and data histograms show a strong decrease of events towards low energies in the cascade-like bin. This background expectation is not necessarily supposed to agree with the

data, because these distributions are assuming nominal parameter values, before performing the fit to find the parameters that describe the data best.

6.2 Statistical Analysis

6.2.1 Test Statistic

The measurements are performed by comparing the weighted MC to the data. Through variation of the nuisance and physics parameters that govern the weights, the best matching set of parameters can be found, by optimizing a fit metric. The comparison is done using a modified χ^2, defined as

$$\chi^2_{\text{mod}} = \sum_{i \in \text{bins}} \frac{(N_i^{\text{exp}} - N_i^{\text{obs}})^2}{N_i^{\text{exp}} + (\sigma_i^{\nu})^2 + (\sigma_i^{\mu})^2 + (\sigma_i^{\text{HNL}})^2} + \sum_{j \in \text{syst}} \frac{(s_j - \hat{s_j})^2}{\sigma^2_{s_j}} \,, \tag{6.1}$$

as the fit metric. It is designed such that taking the difference between a free fit and a fit with fixed parameters based on a chosen hypothesis, $\Delta\chi^2_{\text{mod}}$, can directly be used as a *test statistic (TS)* for hypothesis testing, due to its asymptotic behavior. The total event expectation is $N_i^{\text{exp}} = N_i^{\nu} + N_i^{\mu} + N_i^{\text{HNL}}$, where N_i^{ν}, N_i^{μ}, and N_i^{HNL} are the expected number of events in bin i from neutrinos, atmospheric muons, and HNLs, while N_i^{obs} is the observed number of events in the bin. The expected number of events from each particle type is calculated by summing the weights of all events in the bin $N_i^{\text{type}} = \sum_i^{\text{type}} \omega_i$, with the statistical uncertainty being $(\sigma_i^{\text{type}})^2 = \sum_i^{\text{type}} \omega_i^2$. The additional term in Equation 6.1 is included to apply a penalty term for prior knowledge of the systematic uncertainties of the parameters where they are known. s_j are the systematic parameters that are varied in the fit, while $\hat{s_j}$ are their nominal values and σ_{s_j} are the known uncertainties.

6.2.2 Physics Parameters

The variable physics parameter in this analysis is the mixing between the HNL and the SM τ sector, $|U_{\tau 4}|^2$. It is varied continuously in the range of [0.0 , 1.0] by applying the weighting scheme described in Section 4.2.3. The fit is initialized at an off-nominal value of 0.1. The other physics parameter, the mass m_4 of the HNL, is implicitly fixed to one of the three discrete masses to be tested, by using the corresponding sample of the HNL simulation described in Section 4.2.

6.2.3 Nuisance Parameters

There are multiple sources of systematic uncertainties related to the event generation and detector simulation explained in Chapter 4. All uncertainties considered in this work need to be implemented with parameters that can be varied continuously so that a simultaneous fit of the physics and systematic parameters can be performed. Where possible, a correct model of the effect is used, but in many cases the variations are captured by effective parameters. Uncertainties that solely scale the total event rate are not included individually, since the analysis only uses the relative distribution of events

and a single scaling parameter N_ν is used to scale the total neutrino rate instead.

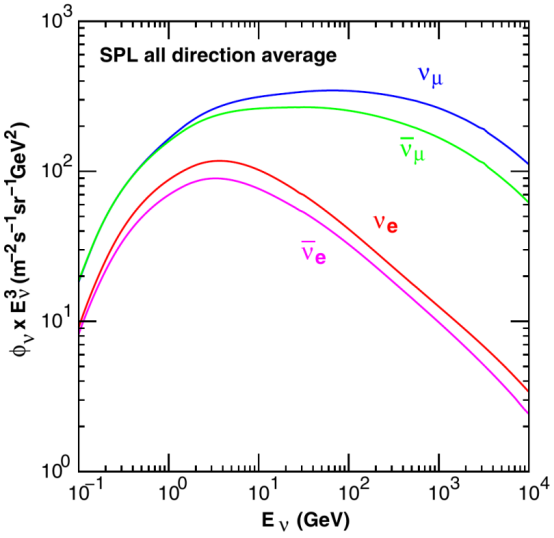

Figure 6.3: Atmospheric neutrino flux computed at the South Pole. Shown are the neutrino and antineutrino flux for ν_e and ν_μ. Taken from [82].

Atmospheric Flux Uncertainties

The flux of atmospheric neutrinos is influenced by multiple factors, the spectrum and composition of primary CRs, the atmospheric conditions, and the hadronic interaction model used to describe the air showers development. Uncertainties of the neutrino flux are therefore dictated by the uncertainties on these components, where the variations in atmospheric conditions were found to have negligible effect [132]. The baseline neutrino flux used in this thesis is taken from [82]. Figure 6.3 shows the flux for neutrinos and antineutrinos, computed at the South Pole.

[132]: Abbasi et al. (2023), "Measurement of atmospheric neutrino mixing with improved IceCube DeepCore calibration and data processing"

[82]: Honda et al. (2015), "Atmospheric neutrino flux calculation using the NRLMSISE-00 atmospheric model"

Cosmic ray flux: The selected sample of atmospheric neutrinos lies around energies of up to 100 GeV. The initial primary particles in the CR flux can have 100 times larger energies and therefore the CR flux between 10 GeV and 10 TeV is important, which dominantly consists of hydrogen and helium nuclei [145]. The uncertainty in this CR flux component can be described as a power law correction [146, 147]

$$\Phi'_\nu = \Phi_\nu \left(\frac{E}{E^\star} \right)^{\Delta\gamma} , \tag{6.2}$$

where $E^\star$ is the pivot energy and $\Delta\gamma$ is the correction to the power law exponent. This modification propagates into the neutrino flux, which is therefore corrected in the same way. $E^\star$ was chosen to be 24 GeV as to minimize the dependence of the overall flux scale on $\Delta\gamma$ [132].

[145]: Dembinski et al. (2017), "Data-driven model of the cosmic-ray flux and mass composition from 10 GeV to 10^{11} GeV"

[146]: Barr et al. (2006), "Uncertainties in atmospheric neutrino fluxes"

[147]: Evans et al. (2017), "Uncertainties in atmospheric muon-neutrino fluxes arising from cosmic-ray primaries"

Hadronic interaction model: Neutrinos are produced from the decaying hadrons (dominantly pions and kaons) in CR air shower, spanning a large parameter space that is sparsely evaluated by experimental data. To include uncertainties based on energy, direction, and neutrino flavor, the MCEq package [148] is used to compute the distribution of atmospheric leptons and to estimate the impact of varying their contributions. The calculations

result in the change in flux $\mathrm{d}\Phi_\mathrm{l}/\mathrm{d}B$ for a variation $\mathrm{d}B$ of some parameter B. Scaling this variation by some value b, the modified total flux, s is then given by

$$\Phi'_\mathrm{l} = \Phi_\mathrm{l} + \left(b \cdot \frac{\mathrm{d}\Phi_\mathrm{l}}{\mathrm{d}B} \right) . \tag{6.3}$$

Matching the work in [149], the parameter space is divided in regions of the primary energy, E_i, and the energy fraction of the secondary meson, x_lab, with varying uncertainties, derived from fixed target experiment data. The Sibyll2.3c [150] hadronic interaction model and the GSF cosmic ray flux [145] were used to calculate the related flux changes[1] for the different regions in E_i and x_lab, resulting in 17 variables, encoding the possible changes. Figure 6.4 shows the selected regions of the parameter space and the names given to the uncertainties. At the energies relevant for this work, the flux is dominantly affected by the pion uncertainties. The variational term in Equation 6.3 is applied for each of these parameters and the total variation is the sum of all individual variations.

[149]: Barr et al. (2006), "Uncertainties in Atmospheric Neutrino Fluxes"

[150]: Riehn et al. (2020), "Hadronic interaction model sibyll 2.3d and extensive air showers"

[145]: Dembinski et al. (2017), "Data-driven model of the cosmic-ray flux and mass composition from 10 GeV to 10^{11} GeV"

1: The choice of flux and hadronic interaction model have negligible impact on the variations.

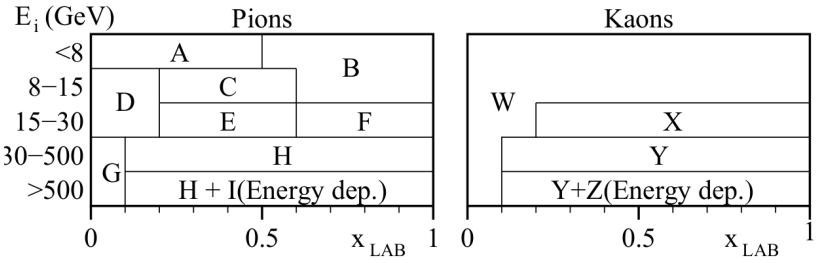

Figure 6.4: Flux uncertainty regions of the hadronic interaction model in the phase space of the primary energy E_i and the energy fraction of the secondary meson x_lab. Taken from [149].

Cross-Section Uncertainties

The uncertainties related to the cross-sections are split into low and high energy components, since there is no coherent model to explain both regimes. Below 20 GeV, *charged current resonance production (CCRES)* and *charged current quasi elastic scattering (CCQE)* interactions with the nucleons as a whole are important, while above 20 GeV DIS interactions are the dominant processes. Three parameters are included to account for all relevant cross-section uncertainties.

At low energies two parameters are included to account for uncertainties in form factors of CCQE and CCRES events. These uncertainties are due to uncertainties in the *axial mass* M_A, which enters the form factor as in

$$F(Q^2) \sim \frac{1}{(1 - (\frac{Q}{M_\mathrm{A}})^2)^2} , \tag{6.4}$$

where Q^2 is the momentum transfer squared. The axial mass can be determined experimentally and to include uncertainties on the values of $M_\mathrm{A}^\mathrm{CCQE}$ and $M_\mathrm{A}^\mathrm{CCRES}$, the cross-sections are computed for each event, where the form factors are calculated varying the axial mass by $\pm 20\%(1\sigma)/\pm 40\%(1\sigma)$ around the nominal value. This is an approximation of the recommended uncertainties by the GENIE collaboration, which are −15%, +25% for $M_\mathrm{A}^\mathrm{CCQE}$ and ±20% for $M_\mathrm{A}^\mathrm{CCRES}$ [116]. To apply a continuous uncertainty variation of the axial mass in a fit, the total cross-section is fit with a quadratic function

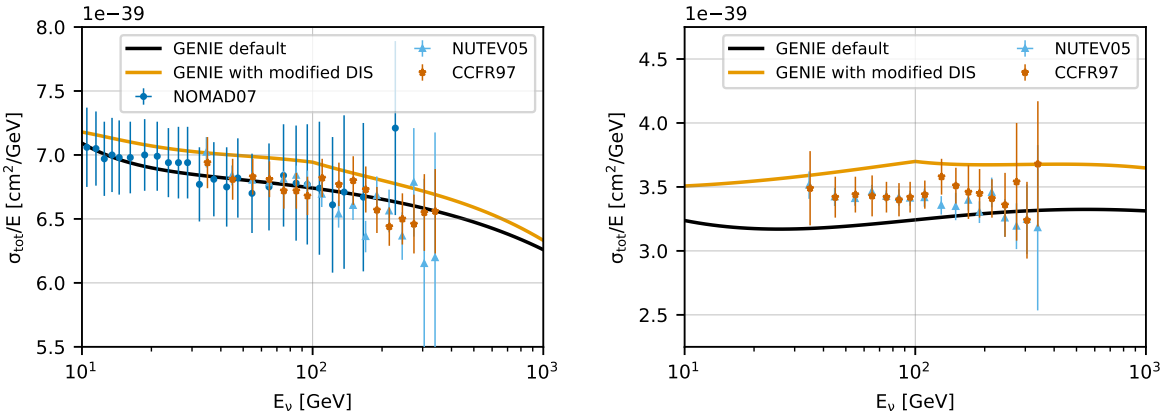

Figure 6.5: Inclusive total neutrino-nucleon cross-sections on an isoscalar target (black) for neutrinos (left) and antineutrinos (right) calculated with GENIE, comparing to measurements from NOMAD [151], NUTEV [152], and CCFR [153]. The scaled GENIE cross-section (orange) is also shown. Taken from [132].

to interpolate between the cross-sections computed with the different axial masses.

Even though the DIS interactions can be calculated very precisely, there are still uncertainties in the input PDF, describing the probability of finding a specific parton (quark) with a specific momentum fraction x inside a nucleon. To account for differences between the used method and more sophisticated methods using newer PDFs seen at high energies, an uncertainty parameter is introduced. The parameter is based on the discrepancy between the cross-sections computed with GENIE and the ones computed with CSMS [154] above 100 GeV. The included parameter scales the cross-section from the GENIE values to the CSMS values, which are considered more accurate above 100 GeV. The scaling is done as a function of energy and inelasticity and to guarantee continuity, the scaling is extrapolated linearly[2] below 100 GeV. The parameter is designed such that a value of 0.0 corresponds to the GENIE cross-sections and a value of 1.0 gives an approximation of the CSMS cross-sections. A comparison of the total cross-sections GENIE (scaled/unscaled) with the data is shown in Figure 6.5.

[154]: Cooper-Sarkar et al. (2011), "The high energy neutrino cross-section in the Standard Model and its uncertainty"

2: Multiple functional extrapolations were tested, but the choice was found to have negligible impact.

Detector Calibration Uncertainties

The detection process of neutrinos in IceCube has several sources of uncertainties, where the effects of the properties of the ice itself and the optical efficiency of the DOMs are dominant for this analysis. None of these uncertainties can be described by an analytic expression, so instead their effects are estimated using MC simulation. This is done by producing additional simulation samples at discrete values of those parameters. The five relevant uncertainty parameters are the absolute efficiency of the DOMs, a global scaling of ice scattering and absorption lengths, and variations of the relative angular acceptance due to hole ice variations in two parameters. To perform the fit, continuous variations with respect to these parameters will be derived with a method explained in the following.

Relative DOM efficiency: As was already mentioned in Section 3.1.1, the absolute efficiency of the DOMs, ϵ_{DOM}, is calibrated using minimum ionizing

muons from air showers, due to the lack of a calibrated light source in the detector. Using the muons as a steady, controlled source of light, the efficiency can be estimated by comparing simulated muon data sets with varied DOM response to the measured data. Since the uncertainties found in multiple iterations of this study [93, 94] are at the order of 10 %, this systematic is highly relevant and is included in the analysis.

[93]: Feintzeig (2014), "Searches for Point-like Sources of Astrophysical Neutrinos with the IceCube Neutrino Observatory"
[94]: Kulacz (2019), "In Situ Measurement of the IceCube DOM Efficiency Factor Using Atmospheric Minimum Ionizing Muons"

Ice scattering and absorption: Absorption and scattering length are the most important properties that govern the propagation of photons through the ice. The simulation principle and how the depth dependent absorption and scattering coefficients are used was already explained in Section 4.4.1. To account for uncertainties on this model of the ice coefficients, a global scaling for each of the two parameters is applied.

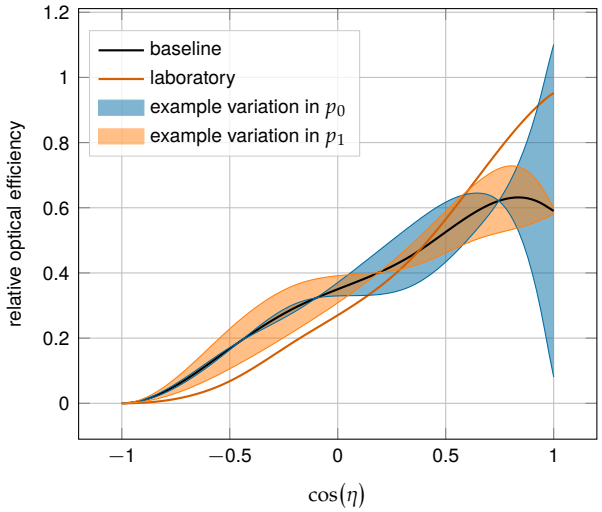

Figure 6.6: Relative angular acceptance modification due to hole ice. Shown is the current baseline model, the variations from changing p_0 and p_1, and a laboratory measurement. Modified from [19].

Hole ice angular acceptance: Due to bubble formation in the re-freezing process of the boreholes, the hole ice is less transparent in the center of the columns [155]. This effectively decreases the chance of photons hitting the DOMs directly from below, which can be described as an additional angular modification of the DOM acceptance. The modification is parameterized by a two-dimensional, normalized[3] function, where the two dominant of the parameters (p_0, p_1), dictating its form, are enough to describe all past and the current hole ice models from both *in-situ* and laboratory measurements. Figure 6.6 shows the acceptance modification as a function of the incident photon angle $\cos(\eta)$. The current baseline model, the variations achieved through modifying p_0 and p_1, and a laboratory measurement can be seen.

[155]: Rongen, Martin (2016), "Measuring the optical properties of IceCube drill holes"

3: The hole ice angular acceptance modification is normalized so that it does not affect the total charge.

Ice Model: The ice model used in IceCube is continuously improved, and the recent models incorporate the birefringent polycriystalline microstructure [156] into the ice properties. To account for the uncertainty, due to this un-modeled effect in the ice model used for the simulation production, an additional simulation sample is produced using the newer version of the ice model, that incorporates the *birefringence (BFR)* effect.

[156]: Abbasi et al. (2024), "In situ estimation of ice crystal properties at the South Pole using LED calibration data from the IceCube Neutrino Observatory"

Treatment of Detector Systematic Uncertainties: Since the variations related to the detector calibration uncertainties are estimated by simulating

MC at discrete values of the systematic parameters, a method to derive continuous variations is needed to perform the fit. The method applied here was initially introduced in [157] and first used in the low energy sterile neutrino search in [19] (section 7.4.3). Using a *likelihood-free inference* technique, re-weighting factors are found for every event in the nominal MC sample, given a specific choice of detector systematic parameters. These factors quantify how much more or less likely the event would be for the corresponding change in detector response from the nominal parameters.

[157]: Fischer et al. (2023), "Treating detector systematics via a likelihood free inference method"
[19]: Trettin (2023), "Search for eV-scale sterile neutrinos with IceCube DeepCore"

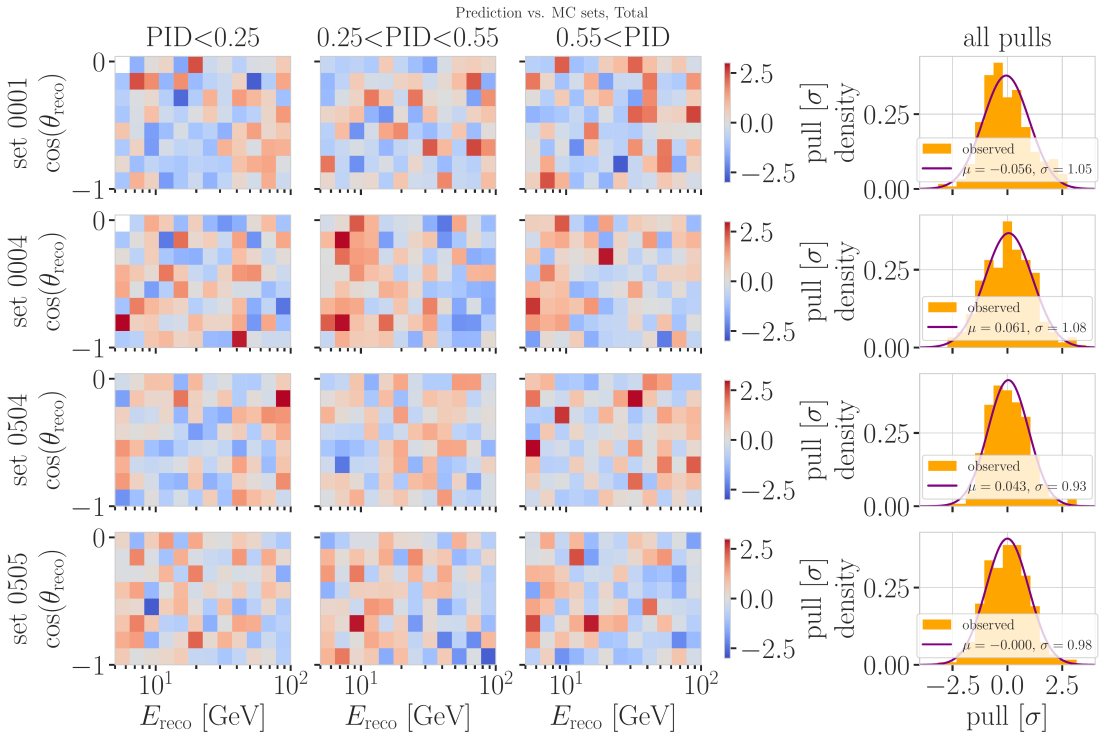

Figure 6.7: Three-dimensional pulls and set-wise pull distributions between the nominal set and the specific systematic sets, after the nominal set was re-weighted to the corresponding systematic parameter value. Set 0001 and 0004 have the DOM efficiency varied by ±10%, while set 0504 and 0505 have the ice absorption varied by ±10%.

Without going into the details of the method, which were already exhaustively discussed in [157] and [19], the performance is assessed here for the HNL signal simulation. In order to do so, the weights are applied to the nominal MC samples, choosing the detector systematic values used to produce the discrete samples and the resulting event expectations are compared to the expectations from the individual, discrete MC samples. The bin counts are compared by calculating the pull defined as

$$p = \frac{N_{\text{reweighted}} - N_{sys}}{\sqrt{\sigma^2_{\text{reweighted}} + \sigma^2_{sys}}}\,, \tag{6.5}$$

where N are the bin-wise event expectations and σ are their MC uncertainty. For the SM BG simulation, the performance was already investigated in [158] (section 7.4.4, appendix B5) and the re-weighted nominal MC was shown to be in agreement with the discrete systematic sets at a sufficient level. Figure 6.7 shows the bin-wise pulls for the 1.0 GeV HNL mass sample at a mixing of 0.1 for a selection of the discrete systematic samples, where the DOM efficiency and the ice absorption were varied by ±10%. As expected, the pull distributions follow a standard normal distribution, without strong

[158]: Lohfink (2023), "Testing non-standard neutrino interaction parameters with IceCube-DeepCore"

clustering or any systematic deviations. A similar performance is found for the additional systematic variations and the detailed figures can be found in Section C.2.

Muon Uncertainties

The muon fraction in the final level selection (see Section 5.4.2) is below 1 %, therefore additional muon systematic uncertainties apart from the spectral index are not implemented, but rather a total muon scaling parameter is added. This total scale is somewhat degenerate with the DOM efficiency, since an increased DOM efficiency leads to better muon rejection. Both the total muon scaling and the muon spectral index have a very small impact on the analysis as will be shown in the following.

Free Parameters

To decide which systematic uncertainties should be included in the fit, we test the potential impact they have on the TS if they are neglected. The test is performed by creating pseudo-data sets from the MC by choosing the nominal nuisance parameters and specific physics parameters, without adding any statistical or systematic fluctuations to it. These so-called *Asimov*[4] data sets are made with the BG simulation and the HNL simulation of the 1.0 GeV mass sample at a mixing value of 0.1, which is chosen as a benchmark physics parameter, but the explicit choice does not have a significant impact on the test. The systematic parameter of interest is set to a value above its nominal expectation, either pulled up by $+1\sigma$ or by an educated estimate for parameters without a well-defined uncertainty. A fit is performed fixing the systematic parameter of interest and leaving all additional parameters free. The resulting TS is the fit metric difference between this fit and a fit with all parameters free, which would result in a fit metric of 0.0 for this Asimov test. This difference is called mis-modeling significance and parameters below a significance of 0.1 σ are fixed. The test is performed in an iterative manner until the final set of free parameters is found.

Figure 6.8 shows the resulting significances of one of these tests. The parameters tested are the systematic parameters introduced in Section 6.2.3 and the atmospheric oscillation parameters mentioned in Section 6.1. In the final selection of free parameters the Barr h_{π^+} parameter was also left free, to sufficiently cover the relevant energy production range of the Pions, as can be seen in Figure 6.4, where both for kaons and pions the uncertainties are included for primary energies above 30 GeV and $x_{\text{lab}} > 0.1$. Additionally, the ice absorption is still kept free, despite showing a small significance, which is done because the ice parameters are not well constrained and are known to have a large impact, which might be concealed in this idealized test, due to correlations with the other parameters. In this test, the effect of correlations is challenging to consider, because only the impact of one parameter is tested at a time, using the overall mis-modeling significance as a measure. The mis-modeling could be reduced by a correlated parameter capturing the effect of the parameter of interest. For this reason a very conservative threshold of 0.1 σ is chosen and some parameters below the threshold are still left free in the fit.

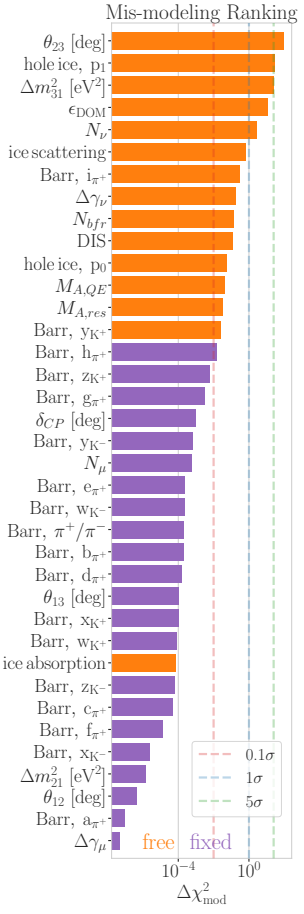

Figure 6.8: Mis-modeling impact ranking of the systematic parameters. The mis-modeling is calculated as the fit metric difference between a fit with the parameter fixed at its nominal value and a fit with the parameter pulled up by $+1\sigma$. The test was performed using Asimov data of the 1.0 GeV mass sample at a reference mixing of 0.1.

4: A pseudo-data set without statistical fluctuations is called Asimov data set.

Parameter	Nominal	Range	Prior
$\theta_{23}[^\circ]$	47.5047	[0.0, 90.0]	-
$\Delta m^2_{31}[\text{eV}^2]$	0.002475	[0.001, 0.004]	-
N_ν	1.0	[0.1, 2.0]	-
$\Delta\gamma_\nu$	0.0	[-0.5, 0.5]	0.1
Barr h_{π^+}	0.0	[-0.75, 0.75]	0.15
Barr i_{π^+}	0.0	[-3.05, 3.05]	0.61
Barr y_{K^+}	0.0	[-1.5, 1.5]	0.3
DIS	0.0	[-0.5, 1.5]	1.0
$M_{\text{A,QE}}$	0.0	[-2.0, 2.0]	1.0
$M_{\text{A,res}}$	0.0	[-2.0, 2.0]	1.0
ϵ_{DOM}	1.0	[0.8, 1.2]	0.1
hole ice p_0	0.101569	[-0.6, 0.5]	-
hole ice p_1	-0.049344	[-0.2, 0.2]	-
ice absorption	1.0	[0.85, 1.15]	-
ice scattering	1.05	[0.9, 1.2]	-
N_{bfr}	0.0	[-0.2, 1.2]	-

Table 6.4: Systematic uncertainty parameters that are left free to float in the fit. Their allowed fit ranges are shown with the nominal value and the Gaussian prior width if applicable.

All nuisance parameters that are left free in the fit are summarized in Table 6.4, showing their nominal values, the allowed fit ranges, and their Gaussian prior, if applicable. The scaling parameter N_ν is included to account for the overall normalization of the neutrino rate, and it has the identical effect on the neutrino events and the HNL events, because they both originate from the same neutrino flux. Despite being known to ~5 % in this energy range [82], there is no prior applied to this parameter, because the fit itself is able to constrain it well, which can be seen by the large impact it shows in Figure 6.8. Concerning the atmospheric neutrino flux, the CR power law flux correction factor $\Delta\gamma_\nu$ introduced in Section 6.2.3 is included with nominal value of 0.0 which corresponds to the baseline flux model. A slightly conservative prior of 0.1 is applied to the parameter, while latest measurements show an uncertainty of 0.05 [147]. The Barr parameters are constrained by a Gaussian prior, taken from [149]. All the detector systematic uncertainties are included in the fit. The DOM efficiency is constrained by a Gaussian prior with a width of 0.1, which is a conservative estimate based on the studies of the optical efficiency using minimum ionizing muons from [93, 94]. The two atmospheric neutrino oscillation parameters θ_{23} and Δm^2_{31} are also included in the fit with nominal values of 47.5° and $2.48 \times 10^{-3}\,\text{eV}^2$ [139], respectively. Since they govern the shape and the strength of the tau neutrino flux, by defining the oscillation from ν_μ to ν_τ, they are also relevant for the HNL signal shape.

[147]: Evans et al. (2017), "Uncertainties in atmospheric muon-neutrino fluxes arising from cosmic-ray primaries"

6.2.4 Low Energy Analysis Framework

[159]: Aartsen et al. (2020), "Computational techniques for the analysis of small signals in high-statistics neutrino oscillation experiments"

The analysis is performed using the PISA [159] [160] software framework, which was developed to perform analyses of small signals in high-statistics neutrino oscillation experiments. It is used to generate the expected event distributions from several MC samples, which can then be compared to the observed data. The expectation for each MC sample is calculated by applying physics and nuisance parameter effects in a stage-wise manner, before combining them to the final expectation.

6.3 Analysis Checks

Fitting to data is performed in a *blind* manner, where the analyzer does not immediately see the fitted physics and nuisance parameter values, but first checks that a set of pre-defined *goodness of fit (GOF)* criteria are fulfilled. This is done to circumvent the so-called *confirmation bias* [161], where the analyzer might be tempted to construct the analysis in a way that confirms their expectation. After the GOF criteria are met to satisfaction, the fit results are unblinded and the full result can be revealed. Before these blind fits to data are performed, the robustness of the analysis method is tested using pseudo-data that is generated from the MC.

[161]: Nickerson (1998), "Confirmation Bias: A Ubiquitous Phenomenon in Many Guises"

6.3.1 Minimization Robustness

To find the set of parameters that best describes the data, a staged minimization routine is used. In the first stage, a fit with coarse minimizer settings is performed to find a rough estimate of the *best fit point (BFP)*. In the second stage, the fit is performed again in both octants[5] of θ_{23}, starting from the BFP of the coarse fit. For each individual fit the *MIGRAD* routine of IMINUIT [162] is used to minimize the χ^2_{mod} fit metric defined in Equation 6.1. Iminuit is a fast, python compatible minimizer based on the Minuit2 C++ library [137]. The individual minimizer settings for both stages are shown in Table 6.5.

5: There is a degeneracy between the lower octant ($\theta_{23} < 45°$) and the upper octant ($\theta_{23} > 45°$), which can lead to fit metric minima (local and global) at two positions that are mirrored around 45° in θ_{23}.

[162]: Dembinski et al. (2022), *scikit-hep/iminuit: v2.17.0*

Fit	Err.	Prec.	Tol.
Coarse	1e-1	1e-8	1e-1
Fine	1e-5	1e-14	1e-5

Table 6.5: Migrad settings for the two stages in the minimization routine. *Err.* are the step size for the numerical gradient estimation, *Prec.* is the precision with which the LLH is calculated, and *Tol.* is the tolerance for the minimization.

To test the minimization routine and to make sure it consistently recovers any physics parameters, Asimov data sets are produced and then fit back with the full analysis chain. This type of test is called *Asimov inject/recover test*. A set of mixing values between 10^{-3} and 10^{0} is injected and without fluctuations the fit is expected to always recover the injected parameters (both physics and nuisance parameters). The fitted mixing values from the Asimov inject/recover tests are compared to the true injected values in Figure 6.9 for all three mass samples. As desired, the fit is always able to recover the injected physics parameter and the nuisance parameters within the statistical uncertainty or at an insignificant fit metric difference.

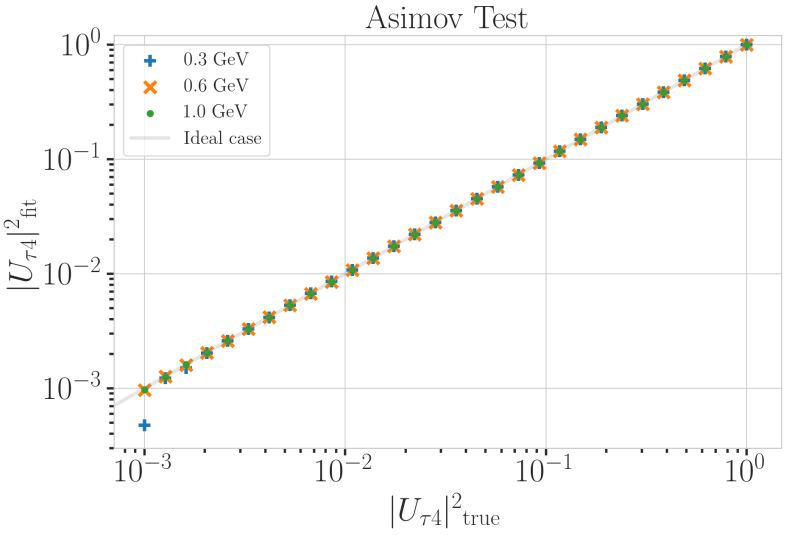

Figure 6.9: Asimov inject/recover test results for all three mass samples. Mixing values between 10^{-3} and 10^{0} are injected and fit back with the full analysis chain. The injected parameter is always recovered within the statistical uncertainty or at an insignificant fit metric difference.

6.3.2 Goodness of Fit

To estimate the GOF of the three data fits, pseudo-data is generated from the MC by injecting the BFP parameters as true parameters and then fluctuating the expected bin counts to account for MC uncertainty and Poisson fluctuations in data. First, the expectation value of each bin is drawn from a Gaussian distribution centered at the nominal expectation value with a standard deviation corresponding to the MC uncertainty of the bin. Based on this sampled expectation value, each bin count is drawn from a Poisson distribution, independently, to get the final pseudo-data set. These pseudo-data sets are analysed with the same analysis chain as the real data, resulting in a final fit metric value for each pseudo-data set. By comparing the distribution of fit metric values from this *ensemble* of pseudo-data trials to the fit metric of the fit to real data, a p-value can be calculated. The p-value is the probability of finding a value of the fit metric at least as large as the one from the data fit. Figure 6.10 shows the distribution from the ensemble tests for for all three mass samples and the observed value from the fit, resulting in p-values of 28.3 %, 28.7 % and 26.0 %. Based on this test, it is concluded that the fit result is compatible with the expectation from the ensemble of pseudo-data trials.

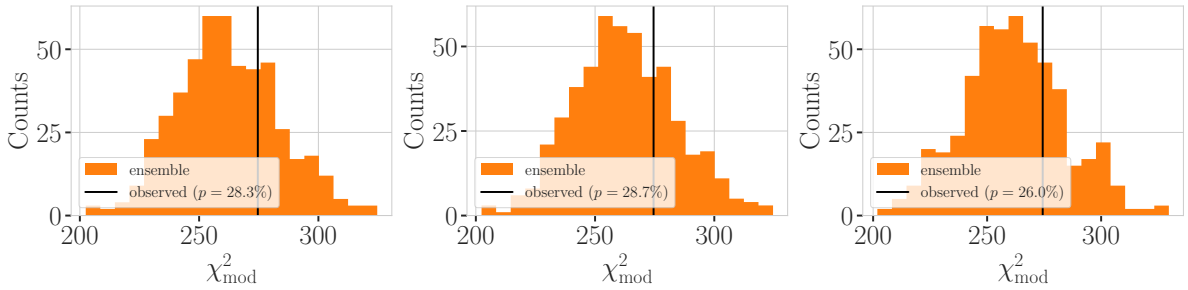

Figure 6.10: Observed fit metric (data fit) and fit metric distribution from pseudo-data ensemble generated around the best fit point. Shown are the results for all three mass samples, with the ensemble distribution on orange, the observed value in black, and the p-value in the legend.

6.3.3 Data/MC Agreement

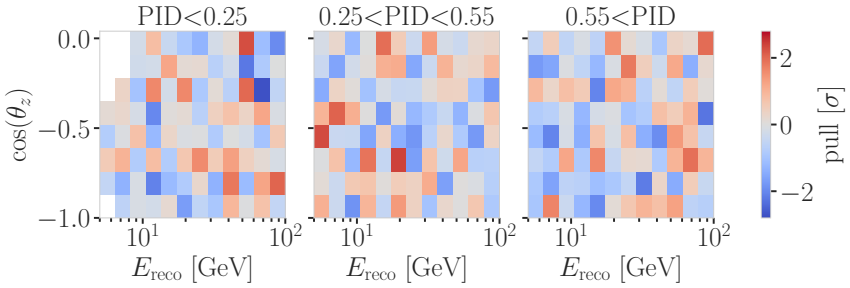

Figure 6.11: Three-dimensional binwise pulls between data and simulation at the best fit point of the 1.0 GeV mass sample fit.

At the BFP, the agreement between the data and simulation is probed by comparing both the one-dimensional analysis distributions for PID, energy, and cosine of the zenith angle as well as the full three-dimensional distributions. Figure 6.11 shows the three-dimensional pull distribution between data and the total MC expectation for the 1.0 GeV mass sample at the BFP. The pulls are evenly spaced and show no strong clustering. In Figure 6.12 the reconstructed energy distributions is shown for the 1.0 GeV mass sample. The data is compared to the total MC expectation, which is

also split up into individual components for illustration. Note here that the HNL events are shown as part of the ν_{NC} events, since they originate from the ν_τ-NC flux. Good agreement can be observed between the distributions, which was quantified by a reduced χ^2, which is close to 1.0 The distributions of the other two analysis variables are shown in Section C.3.

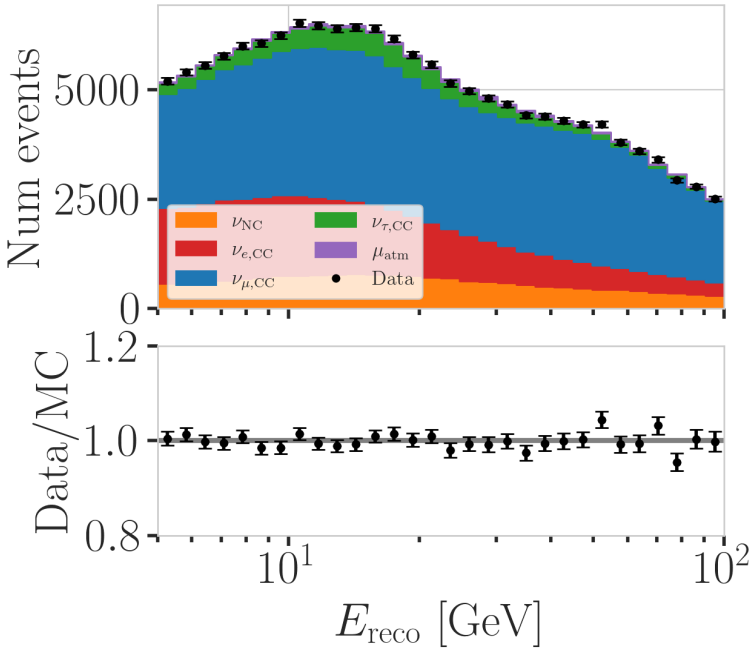

Figure 6.12: Data/MC comparison of the reconstructed energy for the 1.0 GeV mass sample. The data is compared to the total MC expectation, which is also split up into individual components for illustration. The HNL events are shown as part of the ν_{NC} component.

6.4 Results

6.4.1 Best Fit Nuisance Parameters

The resulting nuisance parameter values from the fits are illustrated in Figure 6.13, where the differences to the nominal values are shown, normalized by the distance to the closest boundary. The results from all three fits are shown in the same plot and the fits prefer values of the same size for all three mass samples. For parameters that have a Gaussian prior, the 1 σ range is also displayed. As was already confirmed during the blind fit procedure, all fitted parameters are within this range. The effective ice model parameter, N_{bfr}, prefers a value of ~0.74 , indicating that the data fits better to an ice model that includes real birefringence effects [156]. For completeness, the explicit results are listed in Table C.1. There, the nominal values and the absolute differences to the best fit value are also presented.

6.4.2 Agreement with Standard Model Three-Flavor Oscillation Measurement

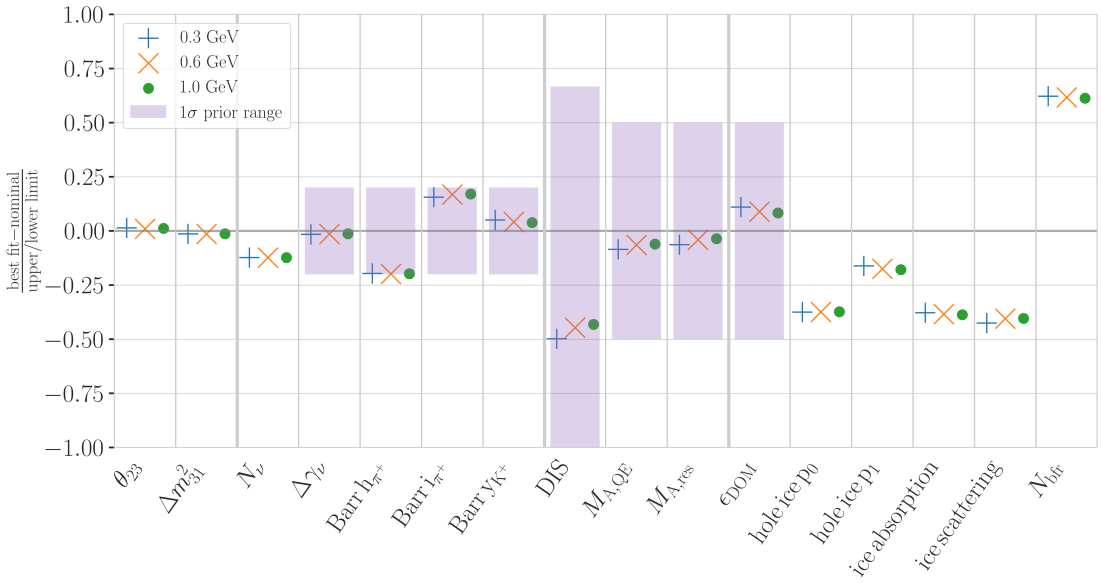

Figure 6.13: Best fit nuisance parameter distances to the nominal values, normalized by the distance to the closest boundary. For parameters with a Gaussian prior, the +1 σ range is also shown.

The recently performed atmospheric neutrino oscillation measurement by the IceCube collaboration resulted in a best fit point of $\sin^2\theta_{23} = 0.544^{+0.030}_{-0.096}$ and $\Delta m^2_{32} = 2.40^{+0.03}_{-0.06} \times 10^{-3}\text{eV}^2$ [139]. The result used the identical 10 years of data at the same final level selection. The differences to this analysis are the choice of fit metric and the use of the previous treatment of detector systematic uncertainties. Both the choice of the fit metric and the detector systematic uncertainty treatment should not influence the best fit values and a naive comparison of the results to the results from this work is done, to validate this is the case. The best fit values of this work are listed in Table 6.6 and are all compatible with the IceCube result within the uncertainties. Since they are statistically fully dependent, a more rigorous quantitative comparison would be more involved and is not performed here. The agreement is still interpreted as a first validation of the new detector systematics treatment.

m_4	$\sin^2\theta_{23}$	Δm^2_{32} [eV^2]
0.3 GeV	0.554	0.0238
0.6 GeV	0.551	0.0238
1.0 GeV	0.553	0.0238

Table 6.6: Best fit oscillation parameters from the three mass sample fits. The values are compatible with the IceCube result within the uncertainties.

[139]: Yu et al. (2023), "Recent neutrino oscillation result with the IceCube experiment"

6.4.3 Best Fit Parameters and Limits

The fitted mixing values are

$$|U_{\tau 4}|^2(0.3\,\text{GeV}) = 0.003^{+0.084}\,,$$
$$|U_{\tau 4}|^2(0.6\,\text{GeV}) = 0.080^{+0.134}\,,\text{and}$$
$$|U_{\tau 4}|^2(1.0\,\text{GeV}) = 0.106^{+0.132}\,,$$

with their +1 σ uncertainty. All of them are compatible with the null hypothesis of 0.0 mixing, although the 0.6 GeV and 1.0 GeV fits indicate a mixing value of 0.08 and 0.106 , respectively. The best fit mixing values and the corresponding upper limits at 68 % and 90 % *confidence level (CL)* are listed in Table 6.7, also showing the p-value to reject the null hypothesis. The CLs and p-value are estimated by assuming that *Wilks' theorem* [163] holds, meaning that the TS follows a χ^2 distribution with one degree of freedom.

[163]: Wilks (1938), "The Large-Sample Distribution of the Likelihood Ratio for Testing Composite Hypotheses"

Figure 6.14 shows the observed TS profiles as a function of $|U_{\tau 4}|^2$ for all three

Table 6.7: Best fit mixing values and the corresponding upper limits at 68 % and 90 % confidence level, as well as the p-value to reject the null hypothesis, estimated by assuming that Wilks' theorem holds.

HNL mass	$\lvert U_{\tau 4}\rvert^2$	68 % CL	90 % CL	NH p-value
0.3 GeV	0.003	0.09	0.19	0.97
0.6 GeV	0.080	0.21	0.36	0.79
1.0 GeV	0.106	0.24	0.40	0.63

fits. The TS profile is the difference in χ^2_{mod} between the free fit and a fit where the mixing is fixed to a specific value. Also shown is the expected TS profile, based on 100 pseudo-data trials, produced at the BFP and then fluctuated using both Poisson and Gaussian fluctuations, to include the data and the MC uncertainty as was explained in Section 6.3.2. The Asimov expectation and the 68 % and 90 % bands are shown and the observed TS profiles lie within the 68 % band for all three, confirming that they are compatible with statistical fluctuations of the observed data. For the 0.3 GeV fit, the observed contour is slightly tighter than the Asimov expectation, meaning that the observed upper limits in $|U_{\tau 4}|^2$ are slightly stronger than expected. For the 0.6 GeV the opposite is the case and the observed upper limit is therefore slightly weaker than expected. For the 1.0 GeV fit, the observed upper limit is very close to the Asimov expectation in the region where the 68 % and 90 % CLs thresholds are crossed. The observed upper limits are also shown in Table 6.7.

6.5 Summary and Outlook

A measurement of the mixing parameter $|U_{\tau 4}|^2$ for HNLs with masses 0.3 GeV, 0.6 GeV, and 1.0 GeV is performed through a binned, maximum likelihood fit, using ten years of IceCube DeepCore data. No significant signal of HNLs is found, and the best fit mixing values obtained are consistent with the null hypothesis of no mixing. The fits constrain the mixing parameter to $|U_{\tau 4}|^2 < 0.19$ ($m_4 = 0.3$ GeV), $|U_{\tau 4}|^2 < 0.36$ ($m_4 = 0.6$ GeV), and $|U_{\tau 4}|^2 < 0.40$ ($m_4 = 1.0$ GeV) at 90 % confidence level. Despite these limits being several orders of magnitude below the current leading limits on $|U_{\tau 4}|^2$, this initial result serves as a successful proof of concept for HNL searches both in IceCube and using atmospheric neutrinos in general.

The analysis is expected improve in the future, and a few key aspects of potential future HNL searches are discussed here. This work applied the low-energy, atmospheric neutrino event selection, which was designed to reduce muons and noise and results in a neutrino dominated sample, and in Section 5.2.3 it was shown that the selection has a similar efficiency for HNLs as for neutrinos. The analysis in its current form is only possible through this strong reduction of muons and noise, but a targeted event selection, aiming for an analysis distinguishing HNLs from SM background could improve the sensitivity significantly.

In the current analysis setup, the HNL signal is treated as a cascade signature, which is true for most of the events, but not all of them. Extending the binning to include dimensions aiming to discriminate between unique HNL event signatures and the SM events, could improve the sensitivity. Additionally, the event sample could be extended to include HNL events that were produced outside the detector and decay inside or vice versa. This would give a more realistic estimate of the expected number of single-cascade events. The current event generator is targeted for both production and decay of the

HNL inside the detector and therefore only provides a conservative estimate of the expected single-cascade event rate.

Since the atmospheric neutrino flux also contains large numbers of muon neutrinos and smaller contributions from electron neutrinos, both the mixing $|U_{e4}|^2$ and $|U_{\mu 4}|^2$ could be probed using the same data. This would require further development on the event generator, as additional decay modes have to be added. On top of that, the current experimental limits for these parameters are much stronger than for $|U_{\tau 4}|^2$ and significant improvements are required to perform a competitive analysis. For any of the three flavors, additional BSM coupling processes, like the dipole coupling, could also be investigated, but would require a dedicated study to understand the potentially different event signatures.

Lastly, the future low-energy extension IceCube upgrade will provide a significant improvement in the sensitivity to low-energy events through a reduced spacing and a segmented directionality of the optical modules. This enhances the light detection and should yield a better chance to identify the unique HNL signature. The data taking is expected to begin in 2026.

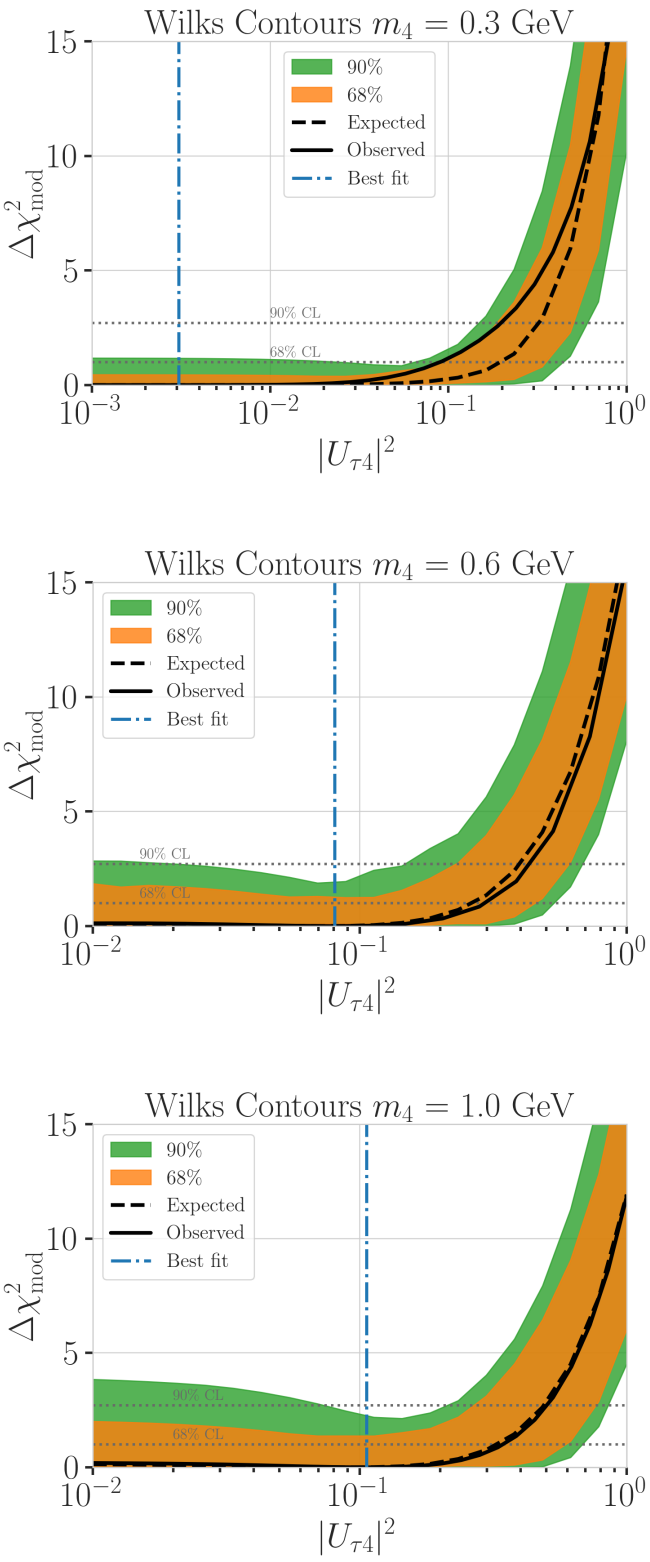

Figure 6.14: Best fit point TS profiles as a function of $|U_{\tau 4}|^2$ for the 0.3 GeV, 0.6 GeV, and 1.0 GeV mass samples. Shown are the observed profiles, the Asimov expectation at the best fit point, and the 68 % and 90 % bands, based on 100 pseudo-data trials. Also indicated are the 68 % and 90 % CL levels assuming Wilks' theorem.

7 Conclusion

The standard model description of neutrinos as three flavors of purely left-handed chiral particles fails to explain the observed experimental evidence of their existing, non-zero masses. The phenomenon of neutrino oscillations can be explained by extending the picture to include three neutrino mass eigenstates, which make up the flavor eigenstates through a superposition. If at least two of the three mass eigenstates have a non-zero mass, the observed oscillations can be described, yet the origin of the neutrino masses remains unknown.

Extending the model to include right-handed neutrinos and additional heavy mass states is one viable explanation to this dilemma. A small mixing between the standard model neutrinos and the additional heavy mass states could explain the observed neutrino masses and their smallness. With large masses ($\gg$eV) these states are called heavy neutral leptons and the small mixing with the standard model particles allows them to participate in weak interactions, which makes experimental searches for these particles possible.

In this work, the first search for GeV-scale heavy neutral leptons using atmospheric neutrinos is presented. The standard three flavor neutrino model is extended by a fourth mass state, allowing mixing with the third lepton generation via a non-zero mixing parameter $|U_{\tau 4}|^2$. The strength of this mixing is measured using ten years of IceCube DeepCore data, by performing a binned, maximum likelihood fit, comparing the observed data to the expected events from atmospheric neutrinos and heavy neutral leptons. Three discrete mass values, m_4, of 0.3 GeV, 0.6 GeV, and 1.0 GeV are tested, constraining the mixing parameter to $|U_{\tau 4}|^2 < 0.19$ ($m_4 = 0.3$ GeV), $|U_{\tau 4}|^2 < 0.36$ ($m_4 = 0.6$ GeV), and $|U_{\tau 4}|^2 < 0.40$ ($m_4 = 1.0$ GeV) at 90 % confidence level. No significant signal of heavy neutral leptons is observed.

Additionally, the potential of IceCube to observe the unique signatures of heavy neutral leptons is investigated. If both the production and the subsequent decay of the heavy neutral lepton happens inside the detector, a double-cascade signature is expected at low energies. After optimizing a double-cascade reconstruction for low-energy events inside the DeepCore volume, the performance of the reconstruction is investigated in detail. This revealed a number of difficulties, where the most challenging difficulty is the low light depositions of these events. It can be concluded that the main reason for the bad reconstruction performance is the low-energy of the second cascade.

Both the first search for heavy neutral leptons and the investigation of the potential to observe their unique signatures lays the fundamental groundwork for future searches for heavy neutral leptons in IceCube. Despite the observed limits being several orders of magnitude below the current leading limits on $|U_{\tau 4}|^2$, this initial result serves as a proof of concept for HNL searches using atmospheric neutrinos. The analysis is expected improve in the future through more sophisticated reconstruction techniques and a targeted event selection. Additionally, the future IceCube Upgrade detector, which is expected to start data taking in 2026, will significantly enhance the

light detection of low-energy cascades and should yield a better chance to identify the unique HNL signature.

Appendix

A

Double-Cascade Event Generation

A.1 Model-Independent Simulation Distributions

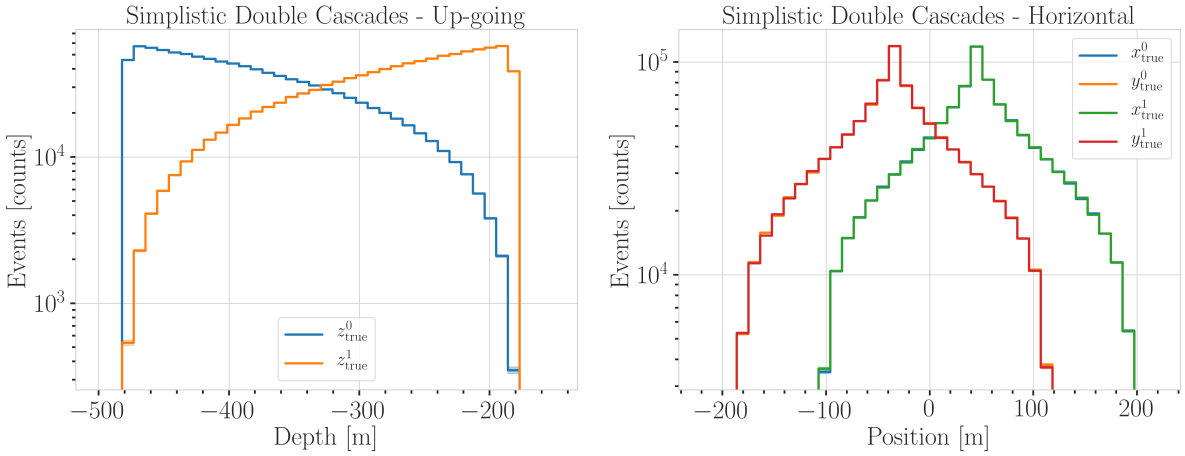

Figure A.1: Generation level distributions of the simplistic simulation sets. Vertical positions of the cascades in the up-going sample (left) and horizontal positions of the cascades in the horizontal sample (right).

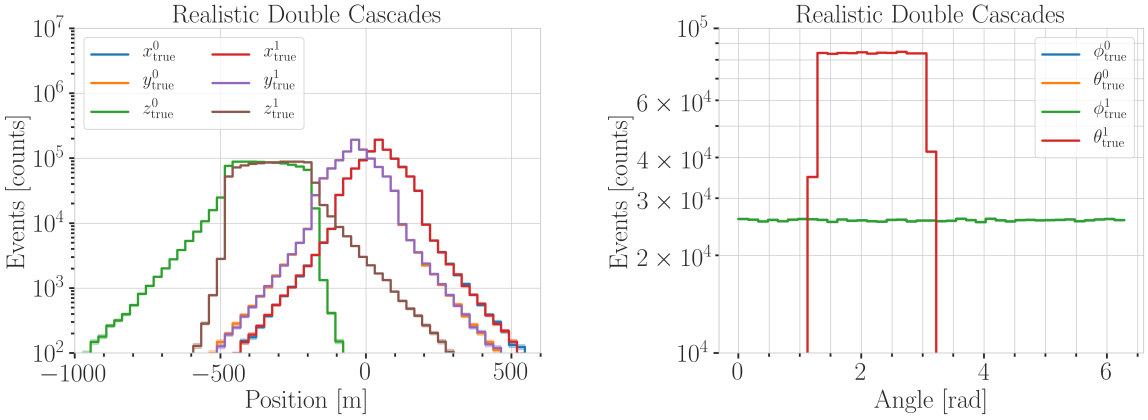

Figure A.2: Generation level distributions of the realistic simulation set. Shown are the cascade x, y, z positions (left) and the cascade direction angles (right).

A.2 Model-Dependent Simulation Distributions

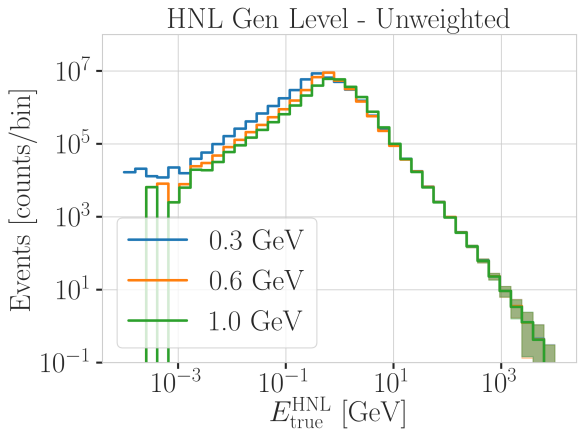

(a) HNL energy

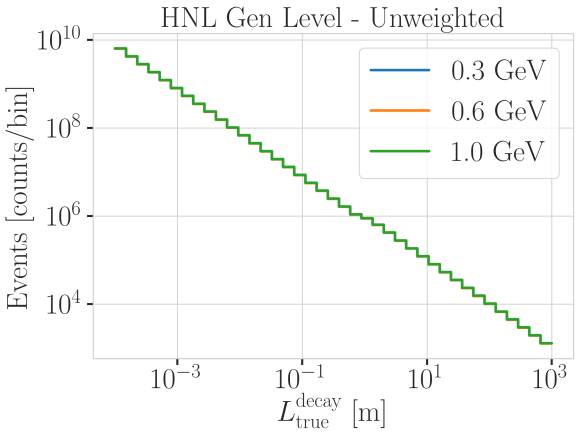

(b) Decay length

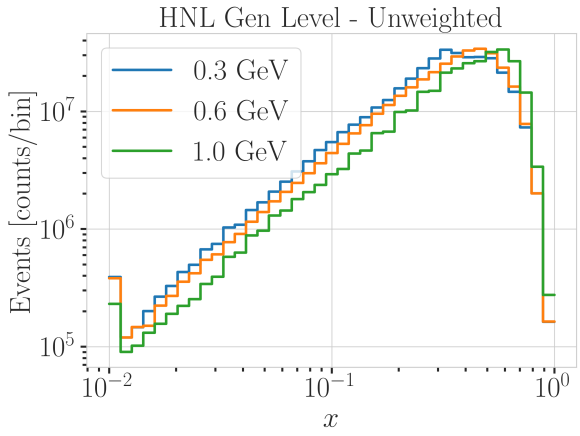

(c) Bjorken x

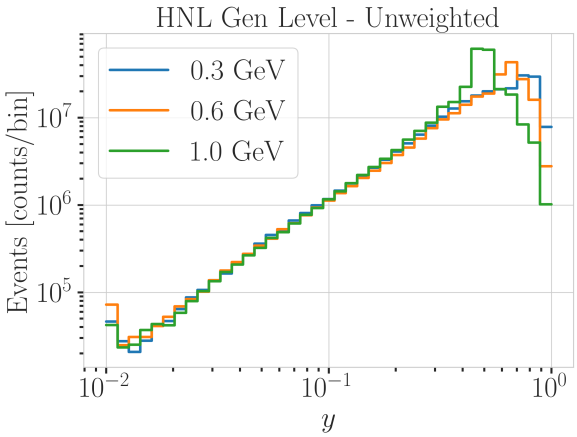

(d) Bjorken y

Figure A.3: Generation level distributions of the model dependent simulation.

B

Event Processing and Reconstruction

B.1 Double-Cascade Classifier Features

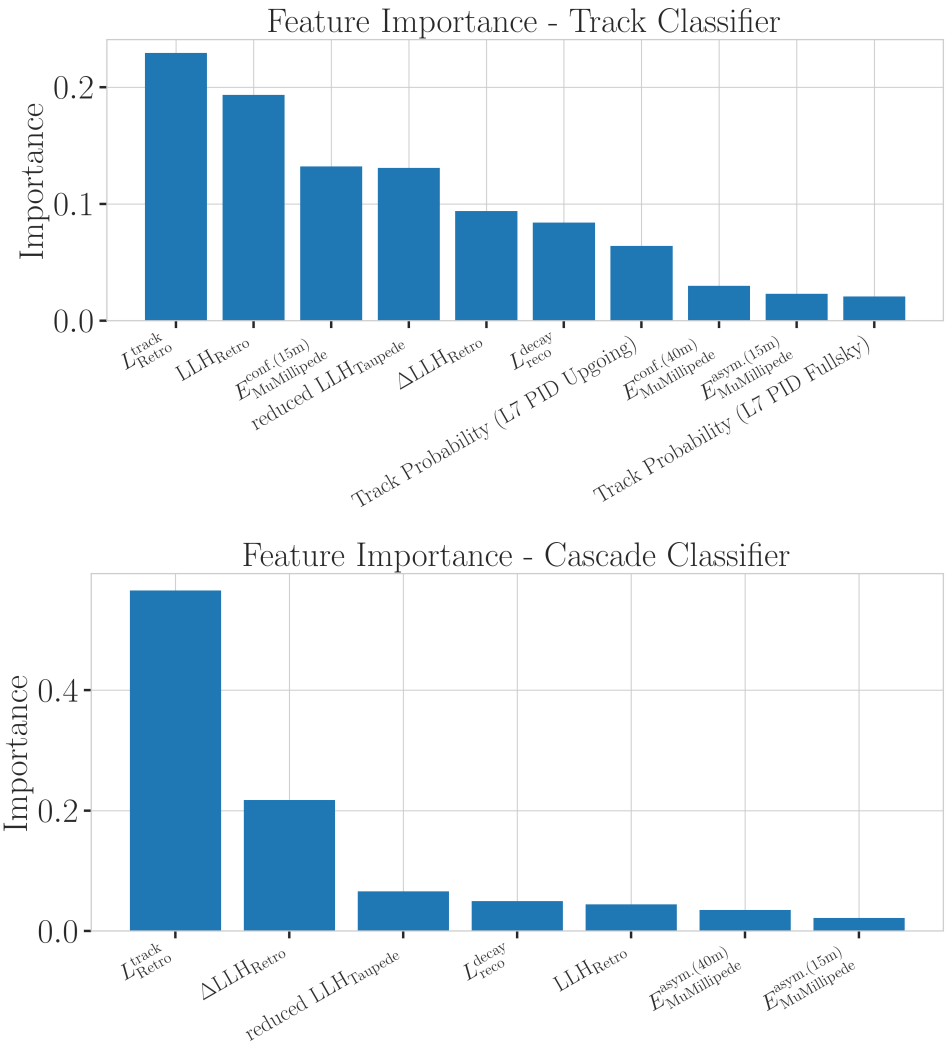

Figure B.1: Feature importances of the classifiers trained to distinguish double-cascades from tracks (top) and from cascades (bottom).

B.2 FLERCNN Resolutions

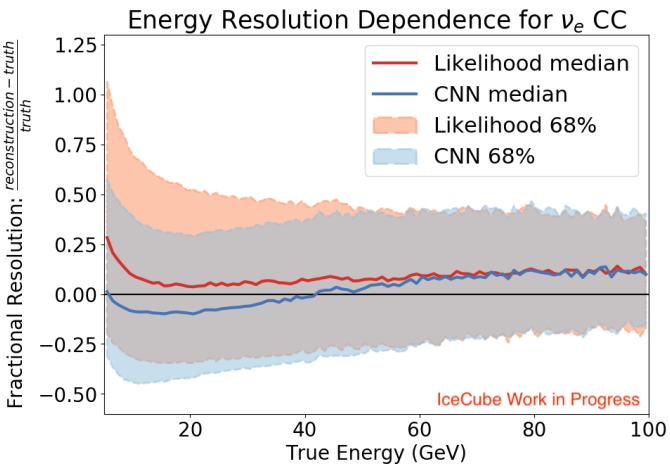

Figure B.2: Energy resolution of the FLERCNN reconstruction for electron neutrinos, compared to the performance of a classical, likelihood based reconstruction. Shown is the median fractional energy resolution and the 68 % band as a function of the true energy.

C

Analysis Results

C.1 Final Level Simulation Distributions

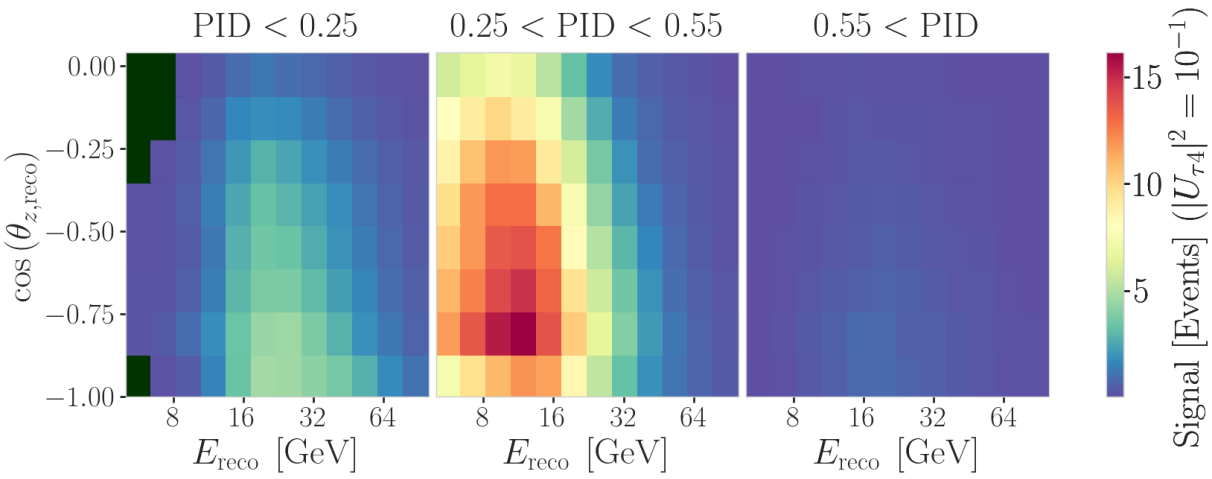

Figure C.1: Signal expectation in 9.28 years for the 1.0 GeV mass sample at a mixing of 0.1, while all other parameters are at their nominal values (top) and observed data (bottom).

C.2 Treatment of Detector Systematic Uncertainties

Shown is the performance of the detector systematic uncertainty treatment. The systematic set 0001 and 0004 have the DOM efficiency varied by ±10%, while set 0504 and 0505 have the ice absorption varied by ±10%. Set 0506 and 0507 have the ice scattering varied by ±10%, and set 1122 is the set with the new ice model, including the birefringence effect. The sets 0301, 0309, 190, 1901, 1902, and 1903 have variations of the hole ice p0 and p1 parameters, covering a wide range.

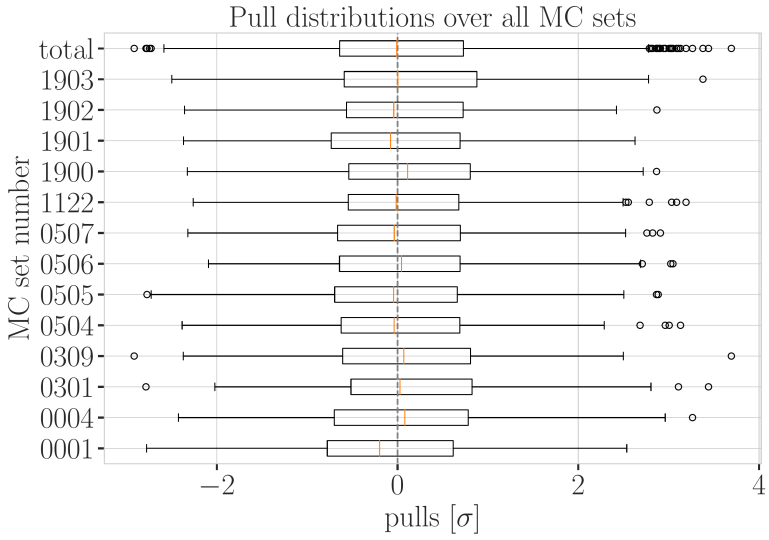

Figure C.2: Overall performance of the detector systematic uncertainty treatment. Shown are the pull distributions of the three-dimensional pulls shown in Figure 6.7 and Figure C.3 between the nominal set and the specific systematic set, after the nominal set was re-weighted to the corresponding systematic parameter value.

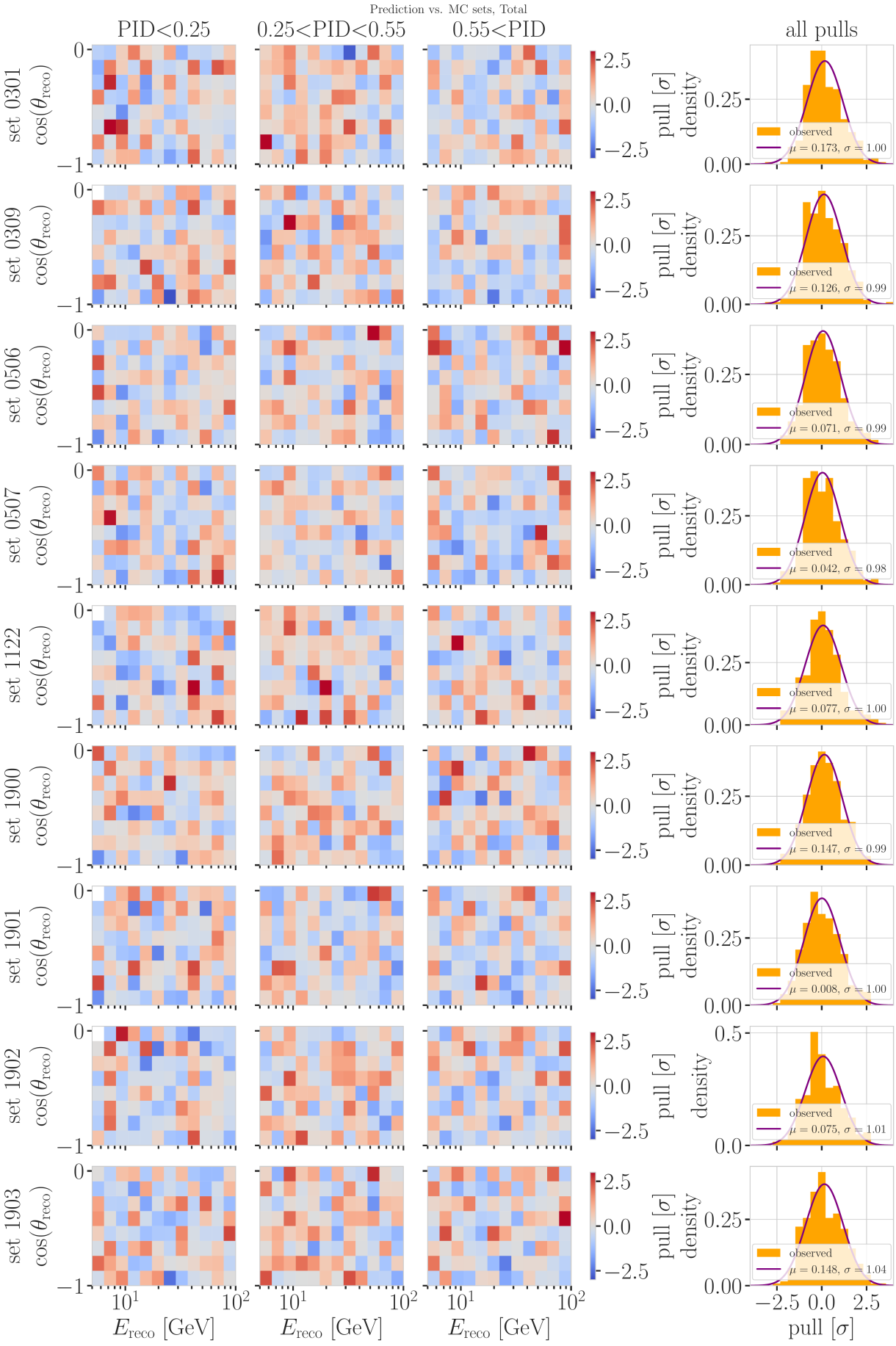

Figure C.3: Three-dimensional pulls and set-wise pull distributions between the nominal set and the specific systematic sets, after the nominal set was re-weighted to the corresponding systematic parameter value.

C.3 Data/MC Agreement

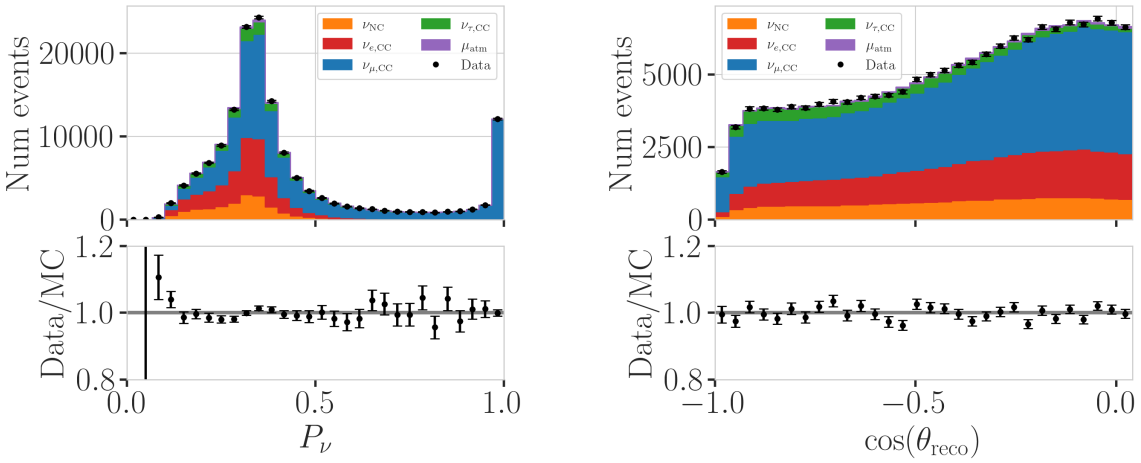

Figure C.4: Data/MC comparison of the PID (top) and cosine of the zenith angle (bottom) for the 0.6 GeV mass sample. The data is compared to the total MC expectation, which is also split up into individual components for illustration. The HNL events are shown as part of the ν_{NC} component.

C.4 Best Fit Nuisance Parameters

Table C.1: Best fit nuisance parameters for the three mass samples. Also shown is the nominal value and the difference between the nominal and the best fit.

Parameter	Nominal	Best Fit			Nominal - Best Fit		
		0.3 GeV	0.6 GeV	1.0 GeV	0.3 GeV	0.6 GeV	1.0 GeV
$\theta_{23}[°]$	47.5047	48.117185	47.918758	48.010986	−0.612485	−0.414058	−0.506286
$\Delta m^2_{31}[\text{eV}^2]$	0.002475	0.002454	0.002454	0.002455	0.000020	0.000021	0.000019
N_ν	1.0	0.889149	0.889055	0.889559	0.110851	0.110945	0.110441
$\Delta\gamma_\nu$	0.0	−0.007926	−0.006692	−0.006596	0.007926	0.006692	0.006596
Barr h_{π^+}	0.0	−0.147475	−0.148481	−0.148059	0.147475	0.148481	0.148059
Barr i_{π^+}	0.0	0.475448	0.513393	0.521626	−0.475448	−0.513393	−0.521626
Barr y_{K^+}	0.0	0.076176	0.062893	0.057548	−0.076176	−0.062893	−0.057548
DIS	0.0	−0.248709	−0.223302	−0.215666	0.248709	0.223302	0.215666
$M_{A,QE}$	0.0	−0.170528	−0.128150	−0.120345	0.170528	0.128150	0.120345
$M_{A,res}$	0.0	−0.125855	−0.080875	−0.070716	0.125855	0.080875	0.070716
ϵ_{DOM}	1.0	1.021984	1.017789	1.016689	−0.021984	−0.017789	−0.016689
hole ice p_0	0.101569	−0.161341	−0.161051	−0.160129	0.262910	0.262620	0.261698
hole ice p_1	−0.049344	−0.073701	−0.075596	−0.076261	0.024357	0.026252	0.026917
ice absorption	1.00	0.943261	0.942463	0.942000	0.056739	0.057537	0.058000
ice scattering	1.05	0.986152	0.989289	0.989438	0.063848	0.060711	0.060562
N_{bfr}	0.0	0.746684	0.740255	0.736215	−0.746684	−0.740255	−0.736215

List of Figures

List of Tables

Bibliography

Here are the references in citation order.

[1] W. Pauli. "Dear radioactive ladies and gentlemen". In: *Phys. Today* 31N9 (1978), p. 27 (cited on page 1).

[2] C. L. Cowan et al. "Detection of the Free Neutrino: a Confirmation". In: *Science* 124.3212 (1956), pp. 103–104. DOI: 10.1126/science.124.3212.103 (cited on page 1).

[3] G. Danby et al. "Observation of High-Energy Neutrino Reactions and the Existence of Two Kinds of Neutrinos". In: *Phys. Rev. Lett.* 9 (1 July 1962), pp. 36–44. DOI: 10.1103/PhysRevLett.9.36 (cited on page 1).

[4] K. Kodama et al. "Observation of tau neutrino interactions". In: *Physics Letters B* 504.3 (2001), pp. 218–224. DOI: https://doi.org/10.1016/S0370-2693(01)00307-0 (cited on page 1).

[5] R. Davis, D. S. Harmer, and K. C. Hoffman. "Search for Neutrinos from the Sun". In: *Phys. Rev. Lett.* 20 (21 May 1968), pp. 1205–1209. DOI: 10.1103/PhysRevLett.20.1205 (cited on pages 1, 6).

[6] M. G. Aartsen et al. "The IceCube Neutrino Observatory: instrumentation and online systems". In: *Journal of Instrumentation* 12.3 (Mar. 2017), P03012. DOI: 10.1088/1748-0221/12/03/P03012 (cited on pages 1, 21–23, 46).

[7] C. N. Yang and R. L. Mills. "Conservation of Isotopic Spin and Isotopic Gauge Invariance". In: *Physical Review* 96.1 (Oct. 1954), pp. 191–195. DOI: 10.1103/PhysRev.96.191 (cited on page 3).

[8] S. Weinberg. "A Model of Leptons". In: *Phys. Rev. Lett.* 19 (21 Nov. 1967), pp. 1264–1266. DOI: 10.1103/PhysRevLett.19.1264 (cited on page 3).

[9] S. L. Glashow. "Partial-symmetries of weak interactions". In: *Nuclear Physics* 22.4 (Feb. 1961), pp. 579–588. DOI: 10.1016/0029-5582(61)90469-2 (cited on page 3).

[10] R. Jackiw. "Physical Formulations: Elementary Particle Theory. Relativistic Groups and Analyticity. Proceedings of the eighth Nobel Symposium, Aspenäsgården, Lerum, Sweden, May 1968. Nils Svartholm, Ed. Interscience (Wiley), New York, and Almqvist and Wiksell, Stockholm, 1969. 400 pp., illus. $31.75." In: *Science* 168.3936 (1970), pp. 1196–1197. DOI: 10.1126/science.168.3936.1196.b (cited on page 3).

[11] P. Higgs. "Broken symmetries, massless particles and gauge fields". In: *Physics Letters* 12.2 (1964), pp. 132–133. DOI: https://doi.org/10.1016/0031-9163(64)91136-9 (cited on page 3).

[12] S. Chatrchyan et al. "Observation of a New Boson at a Mass of 125 GeV with the CMS Experiment at the LHC". In: *Phys. Lett. B* 716 (2012), pp. 30–61. DOI: 10.1016/j.physletb.2012.08.021 (cited on page 3).

[13] G. Aad et al. "Observation of a new particle in the search for the Standard Model Higgs boson with the ATLAS detector at the LHC". In: *Phys. Lett. B* 716 (2012), pp. 1–29. DOI: 10.1016/j.physletb.2012.08.020 (cited on page 3).

[14] M. Gell-Mann. "A Schematic Model of Baryons and Mesons". In: *Resonance* 24 (1964), pp. 923–925 (cited on page 3).

[15] G. Zweig. "An SU(3) model for strong interaction symmetry and its breaking. Version 2". In: *DEVELOPMENTS IN THE QUARK THEORY OF HADRONS. VOL. 1. 1964 - 1978.* Ed. by D. B. Lichtenberg and S. P. Rosen. Feb. 1964, pp. 22–101 (cited on page 3).

[16] D. J. Gross and F. Wilczek. "Ultraviolet Behavior of Non-Abelian Gauge Theories". In: *PRL* 30.26 (June 1973), pp. 1343–1346. DOI: 10.1103/PhysRevLett.30.1343 (cited on page 3).

[17] C. Giunti and C. W. Kim. *Fundamentals of Neutrino Physics and Astrophysics*. Oxford University Press, Mar. 2007 (cited on page 3).

[18] M. D. Schwartz. *Quantum Field Theory and the Standard Model*. Cambridge University Press, 2013 (cited on page 3).

[19] A. Trettin. "Search for eV-scale sterile neutrinos with IceCube DeepCore". PhD thesis. Berlin, Germany: Humboldt-Universität zu Berlin, Mathematisch-Naturwissenschaftliche Fakultät, 2023. DOI: https://github.com/atrettin/PhD-Thesis (cited on pages 5, 9, 27, 43, 72, 73).

[20] N. Deruelle, J.-P. Uzan, and P. de Forcrand-Millard. *Relativity in Modern Physics*. Oxford University Press, Aug. 2018 (cited on page 6).

[21] R. L. Workman et al. "Review of Particle Physics". In: *Progress of Theoretical and Experimental Physics* 2022.8 (Aug. 2022), p. 083C01. DOI: 10.1093/ptep/ptac097 (cited on pages 6, 25, 26, 38).

[22] J. D. Simon. "The Faintest Dwarf Galaxies". In: *Annual Review of Astronomy and Astrophysics* 57 (Aug. 2019), pp. 375–415. DOI: 10.1146/annurev-astro-091918-104453 (cited on page 6).

[23] S. W. Allen, A. E. Evrard, and A. B. Mantz. "Cosmological Parameters from Observations of Galaxy Clusters". In: *Annual Review of Astronomy and Astrophysics* 49.1 (Sept. 2011), pp. 409–470. DOI: 10.1146/annurev-astro-081710-102514 (cited on page 6).

[24] M. Fukugita and T. Yanagida. "Barygenesis without grand unification". In: *Physics Letters B* 174.1 (1986), pp. 45–47. DOI: https://doi.org/10.1016/0370-2693(86)91126-3 (cited on page 6).

[25] Y. Fukuda et al. "Evidence for Oscillation of Atmospheric Neutrinos". In: *Phys. Rev. Lett.* 81 (8 Aug. 1998), pp. 1562–1567. DOI: 10.1103/PhysRevLett.81.1562 (cited on page 6).

[26] Q. R. Ahmad and other. "Direct Evidence for Neutrino Flavor Transformation from Neutral-Current Interactions in the Sudbury Neutrino Observatory". In: *Phys. Rev. Lett.* 89 (1 June 2002), p. 011301. DOI: 10.1103/PhysRevLett.89.011301 (cited on page 6).

[27] S. Alam et al. "Completed SDSS-IV extended Baryon Oscillation Spectroscopic Survey: Cosmological implications from two decades of spectroscopic surveys at the Apache Point Observatory". In: *Phys. Rev. D* 103 (8 Apr. 2021), p. 083533. DOI: 10.1103/PhysRevD.103.083533 (cited on page 6).

[28] N. Aghanim et al. "Planck2018 results: VI. Cosmological parameters". In: *Astronomy & Astrophysics* 641 (Sept. 2020), A6. DOI: 10.1051/0004-6361/201833910 (cited on page 6).

[29] M. Aker et al. "Direct neutrino-mass measurement with sub-electronvolt sensitivity". In: *Nature Phys.* 18.2 (2022), pp. 160–166. DOI: 10.1038/s41567-021-01463-1 (cited on page 6).

[30] T. Asaka, S. Blanchet, and M. Shaposhnikov. "The nuMSM, dark matter and neutrino masses". In: *Phys. Lett. B* 631 (2005), pp. 151–156. DOI: 10.1016/j.physletb.2005.09.070 (cited on page 8).

[31] T. Asaka and M. Shaposhnikov. "The νMSM, dark matter and baryon asymmetry of the universe". In: *Phys. Lett. B* 620 (2005), pp. 17–26. DOI: 10.1016/j.physletb.2005.06.020 (cited on page 8).

[32] V. A. Rubakov and M. E. Shaposhnikov. "Electroweak baryon number nonconservation in the early universe and in high-energy collisions". In: *Usp. Fiz. Nauk* 166 (1996), pp. 493–537. DOI: 10.1070/PU1996v039n05ABEH000145 (cited on page 8).

[33] L. Canetti, M. Drewes, and M. Shaposhnikov. "Sterile Neutrinos as the Origin of Dark and Baryonic Matter". In: *Phys. Rev. Lett.* 110.6 (2013), p. 061801. DOI: 10.1103/PhysRevLett.110.061801 (cited on page 8).

[34] P. Minkowski. "$\mu \to e\,\gamma$ at a rate of one out of 10^9 muon decays?" In: *Physics Letters B* 67.4 (Apr. 1977), pp. 421–428. DOI: 10.1016/0370-2693(77)90435-X (cited on page 8).

[35] T. Yanagida. "Horizontal Symmetry and Masses of Neutrinos". In: *Progress of Theoretical Physics* 64.3 (Sept. 1980), pp. 1103–1105. DOI: 10.1143/PTP.64.1103 (cited on page 8).

[36] S. L. Glashow. "The Future of Elementary Particle Physics". In: *NATO Sci. Ser. B* 61 (1980), p. 687. DOI: 10.1007/978-1-4684-7197-7_15 (cited on page 8).

[37] M. Gell-Mann, P. Ramond, and R. Slansky. "Complex Spinors and Unified Theories". In: *Conf. Proc. C* 790927 (1979), pp. 315–321 (cited on page 8).

[38] R. N. Mohapatra and G. Senjanovi ć. "Neutrino Mass and Spontaneous Parity Nonconservation". In: *Phys. Rev. Lett.* 44 (14 Apr. 1980), pp. 912–915. DOI: 10.1103/PhysRevLett.44.912 (cited on page 8).

[39] M. G. Aartsen et al. "eV-Scale Sterile Neutrino Search Using Eight Years of Atmospheric Muon Neutrino Data from the IceCube Neutrino Observatory". In: *Phys. Rev. Lett.* 125.14 (2020), p. 141801. DOI: 10.1103/PhysRevLett.125.141801 (cited on page 9).

[40] J.-L. Tastet, O. Ruchayskiy, and I. Timiryasov. "Reinterpreting the ATLAS bounds on heavy neutral leptons in a realistic neutrino oscillation model". In: *JHEP* 12 (2021), p. 182. DOI: 10.1007/JHEP12(2021)182 (cited on page 9).

[41] D. A. Bryman and R. Shrock. "Constraints on Sterile Neutrinos in the MeV to GeV Mass Range". In: *Phys. Rev. D* 100 (2019), p. 073011. DOI: 10.1103/PhysRevD.100.073011 (cited on pages 10, 11).

[42] A. Aguilar-Arevalo et al. "Improved search for heavy neutrinos in the decay $\pi \to e\nu$". In: *Phys. Rev. D* 97.7 (2018), p. 072012. DOI: 10.1103/PhysRevD.97.072012 (cited on page 10).

[43] G. Bellini et al. "New limits on heavy sterile neutrino mixing in B8 decay obtained with the Borexino detector". In: *Phys. Rev. D* 88.7 (2013), p. 072010. DOI: 10.1103/PhysRevD.88.072010 (cited on pages 10, 13).

[44] D. Britton et al. "Improved search for massive neutrinos in π + →e + ν decay". In: *Physical Review D* 46 (1992) (cited on page 10).

[45] C. J. Parkinson et al. "Search for heavy neutral lepton production at the NA62 experiment". In: *PoS* EPS-HEP2021 (2022), p. 686. DOI: 10.22323/1.398.0686 (cited on pages 10, 11).

[46] K. Abe et al. "Search for heavy neutrinos with the T2K near detector ND280". In: *Phys. Rev. D* 100.5 (2019), p. 052006. DOI: 10.1103/PhysRevD.100.052006 (cited on pages 10, 11).

[47] P. Abreu et al. "Search for neutral heavy leptons produced in Z decays". In: *Z. Phys. C* 74 (1997). [Erratum: Z.Phys.C 75, 580 (1997)], pp. 57–71. DOI: 10.1007/s002880050370 (cited on pages 10, 12).

[48] R. Barouki, G. Marocco, and S. Sarkar. "Blast from the past II: Constraints on heavy neutral leptons from the BEBC WA66 beam dump experiment". In: *SciPost Phys.* 13 (2022), p. 118. DOI: 10.21468/SciPostPhys.13.5.118 (cited on pages 10–12).

[49] D. Liventsev et al. "Search for heavy neutrinos at Belle". In: *Phys. Rev. D* 87.7 (2013). [Erratum: Phys.Rev.D 95, 099903 (2017)], p. 071102. DOI: 10.1103/PhysRevD.87.071102 (cited on page 10).

[50] P. Achard et al. "Search for heavy isosinglet neutrino in e^+e^- annihilation at LEP". In: *Phys. Lett. B* 517 (2001), pp. 67–74. DOI: 10.1016/S0370-2693(01)00993-5 (cited on page 10).

[51] F. Bergsma et al. "A Search for Decays of Heavy Neutrinos". In: *Phys. Lett. B* 128 (1983). Ed. by J. Tran Thanh Van, p. 361. DOI: 10.1016/0370-2693(83)90275-7 (cited on page 10).

[52] G. Aad et al. "Search for heavy neutral leptons in decays of W bosons produced in 13 TeV pp collisions using prompt and displaced signatures with the ATLAS detector". In: *JHEP* 10 (2019), p. 265. DOI: 10.1007/JHEP10(2019)265 (cited on pages 10, 11).

[53] G. Aad et al. "Search for Heavy Neutral Leptons in Decays of W Bosons Using a Dilepton Displaced Vertex in $\sqrt{s}$ = 13TeV pp Collisions with the ATLAS Detector". In: *Phys. Rev. Lett.* 131 (6 Aug. 2023), p. 061803. DOI: 10.1103/PhysRevLett.131.061803 (cited on pages 10, 11).

[54] A. M. Sirunyan et al. "Search for heavy neutral leptons in events with three charged leptons in proton-proton collisions at $\sqrt{s}$ = 13 TeV". In: *Phys. Rev. Lett.* 120.22 (2018), p. 221801. DOI: 10.1103/PhysRevLett.120.221801 (cited on pages 10, 11).

[55] A. Tumasyan et al. "Search for long-lived heavy neutral leptons with displaced vertices in proton-proton collisions at $\sqrt{s}$ =13 TeV". In: *JHEP* 07 (2022), p. 081. DOI: 10.1007/JHEP07(2022)081 (cited on pages 10, 11).

[56] A. Vaitaitis et al. "Search for neutral heavy leptons in a high-energy neutrino beam". In: *Phys. Rev. Lett.* 83 (1999), pp. 4943–4946. DOI: 10.1103/PhysRevLett.83.4943 (cited on pages 10, 11).

[57] E. Fernandez-Martinez et al. "Effective portals to heavy neutral leptons". In: *JHEP* 09 (2023), p. 001. DOI: 10.1007/JHEP09(2023)001 (cited on pages 10–12).

[58] G. Bernardi et al. "Search for Neutrino Decay". In: *Phys. Lett. B* 166 (1986), pp. 479–483. DOI: 10.1016/0370-2693(86)91602-3 (cited on page 10).

[59] M. Daum et al. "Search for Admixtures of Massive Neutrinos in the Decay $\pi^+ \to \mu^+$ Neutrino". In: *Phys. Rev. D* 36 (1987), p. 2624. DOI: 10.1103/PhysRevD.36.2624 (cited on pages 10, 11).

[60] A. V. Artamonov et al. "Search for heavy neutrinos in $K^+ \to \mu^+ \nu_H$ decays". In: *Phys. Rev. D* 91.5 (2015). [Erratum: Phys.Rev.D 91, 059903 (2015)], p. 052001. DOI: 10.1103/PhysRevD.91.052001 (cited on pages 10, 11).

[61] P. Astier et al. "Search for heavy neutrinos mixing with tau neutrinos". In: *Phys. Lett. B* 506 (2001), pp. 27–38. DOI: 10.1016/S0370-2693(01)00362-8 (cited on page 11).

[62] J. Orloff, A. N. Rozanov, and C. Santoni. "Limits on the mixing of tau neutrino to heavy neutrinos". In: *Phys. Lett. B* 550 (2002), pp. 8–15. DOI: 10.1016/S0370-2693(02)02769-7 (cited on pages 11, 12).

[63] I. Boiarska et al. "Constraints from the CHARM experiment on heavy neutral leptons with tau mixing". In: *Phys. Rev. D* 104.9 (2021), p. 095019. DOI: 10.1103/PhysRevD.104.095019 (cited on pages 11, 12).

[64] P. Abratenko et al. "Search for Heavy Neutral Leptons in Electron-Positron and Neutral-Pion Final States with the MicroBooNE Detector". In: *Phys. Rev. Lett.* 132.4 (2024), p. 041801. DOI: 10.1103/PhysRevLett.132.041801 (cited on page 11).

[65] Y. Ema et al. "Heavy Neutral Leptons from Stopped Muons and Pions". In: *JHEP* 08 (2023), p. 169. DOI: 10.1007/JHEP08(2023)169 (cited on page 11).

[66] A. Cooper-Sarkar et al. "Search for heavy neutrino decays in the BEBC beam dump experiment". In: *Physics Letters B* 160.1 (1985), pp. 207–211. DOI: https://doi.org/10.1016/0370-2693(85)91493-5 (cited on page 11).

[67] J. Badier et al. "Mass and Lifetime Limits on New Longlived Particles in 300-GeV/$c\pi^-$ Interactions". In: *Z. Phys. C* 31 (1986), p. 21. DOI: 10.1007/BF01559588 (cited on page 11).

[68] B. Shuve and M. E. Peskin. "Revision of the LHCb Limit on Majorana Neutrinos". In: *Phys. Rev. D* 94.11 (2016), p. 113007. DOI: 10.1103/PhysRevD.94.113007 (cited on page 11).

[69] R. Aaij et al. "Search for heavy neutral leptons in $W^+ \to \mu^+\mu^\pm$jet decays". In: *Eur. Phys. J. C* 81.3 (2021), p. 248. DOI: 10.1140/epjc/s10052-021-08973-5 (cited on page 11).

[70] R. Plestid. "Luminous solar neutrinos I: Dipole portals". In: *Phys. Rev. D* 104 (2021), p. 075027. DOI: 10.1103/PhysRevD.104.075027 (cited on pages 12, 13).

[71] S. Mertens et al. "A novel detector system for KATRIN to search for keV-scale sterile neutrinos". In: *Journal of Physics G: Nuclear and Particle Physics* 46.6 (2019), p. 065203. DOI: 10.1088/1361-6471/ab12fe (cited on page 12).

[72] M. Aker et al. "Search for keV-scale sterile neutrinos with the first KATRIN data". In: *Eur. Phys. J. C* 83.8 (2023), p. 763. DOI: 10.1140/epjc/s10052-023-11818-y (cited on page 12).

[73] B. Abi et al. "Deep Underground Neutrino Experiment (DUNE), Far Detector Technical Design Report, Volume II: DUNE Physics". In: (Feb. 2020) (cited on page 12).

[74] S. Friedrich et al. "Limits on the Existence of sub-MeV Sterile Neutrinos from the Decay of ^{7}Be in Superconducting Quantum Sensors". In: *Phys. Rev. Lett.* 126.2 (2021), p. 021803. DOI: 10.1103/PhysRevLett.126.021803 (cited on page 13).

[75] C. Hagner et al. "Experimental search for the neutrino decay v3+vj+e++e- and limits on neutrino mixing". English. In: 52.3 (1995), pp. 1343–1352. DOI: 10.1103/PhysRevD.52.1343 (cited on page 13).

[76] R. Plestid. "Luminous solar neutrinos II: Mass-mixing portals". In: *Phys. Rev. D* 104 (2021). [Erratum: Phys.Rev.D 105, 099901 (2022)], p. 075028. DOI: 10.1103/PhysRevD.104.075028 (cited on page 13).

[77] P. Coloma et al. "Double-Cascade Events from New Physics in Icecube". In: *Phys. Rev. Lett.* 119.20 (2017), p. 201804. DOI: 10.1103/PhysRevLett.119.201804 (cited on page 13).

[78] P. Coloma. "Icecube/DeepCore tests for novel explanations of the MiniBooNE anomaly". In: *Eur. Phys. J. C* 79.9 (2019), p. 748. DOI: 10.1140/epjc/s10052-019-7256-8 (cited on page 13).

[79] M. Atkinson et al. "Heavy Neutrino Searches through Double-Bang Events at Super-Kamiokande, DUNE, and Hyper-Kamiokande". In: *JHEP* 04 (2022), p. 174. DOI: 10.1007/JHEP04(2022)174 (cited on page 13).

[80] P. Coloma et al. “GeV-scale neutrinos: interactions with mesons and DUNE sensitivity”. In: *Eur. Phys. J. C* 81.1 (2021), p. 78. DOI: 10.1140/epjc/s10052-021-08861-y (cited on pages 13, 35, 37, 39).

[81] M. Tanabashi et al. “Review of Particle Physics”. In: *Phys. Rev. D* 98 (3 Aug. 2018), p. 030001. DOI: 10.1103/PhysRevD.98.030001 (cited on pages 14, 16, 26).

[82] M. Honda et al. “Atmospheric neutrino flux calculation using the NRLMSISE-00 atmospheric model”. In: *Phys. Rev. D* 92 (2 July 2015), p. 023004. DOI: 10.1103/PhysRevD.92.023004 (cited on pages 14, 41, 69, 75).

[83] A. Fedynitch et al. “Calculation of conventional and prompt lepton fluxes at very high energy”. In: *European Physical Journal Web of Conferences*. Vol. 99. European Physical Journal Web of Conferences. Aug. 2015, p. 08001. DOI: 10.1051/epjconf/20159908001 (cited on page 15).

[84] P. A. M. Dirac. “The Quantum Theory of the Emission and Absorption of Radiation”. In: *Proceedings of the Royal Society of London Series A* 114.767 (Mar. 1927), pp. 243–265. DOI: 10.1098/rspa.1927.0039 (cited on page 15).

[85] I. Esteban et al. “The fate of hints: updated global analysis of three-flavor neutrino oscillations”. In: *JHEP* 09 (2020), p. 178. DOI: 10.1007/JHEP09(2020)178 (cited on pages 16, 17).

[86] A. Terliuk. “Measurement of atmospheric neutrino oscillations and search for sterile neutrino mixing with IceCube DeepCore”. PhD thesis. Berlin, Germany: Humboldt-Universität zu Berlin, Mathematisch-Naturwissenschaftliche Fakultät, 2018. DOI: 10.18452/19304 (cited on pages 17, 28).

[87] J. A. Formaggio and G. P. Zeller. “From eV to EeV: Neutrino cross sections across energy scales”. In: *Rev. Mod. Phys.* 84 (3 Sept. 2012), pp. 1307–1341. DOI: 10.1103/RevModPhys.84.1307 (cited on page 18).

[88] P. B. Price, K. Woschnagg, and D. Chirkin. “Age vs depth of glacial ice at South Pole”. In: *Geophysical Research Letters* 27.14 (2000), pp. 2129–2132. DOI: https://doi.org/10.1029/2000GL011351 (cited on page 22).

[89] M. Ackermann et al. “Optical properties of deep glacial ice at the South Pole”. In: *Journal of Geophysical Research: Atmospheres* 111.D13 (2006). DOI: https://doi.org/10.1029/2005JD006687 (cited on page 22).

[90] R. Abbasi et al. “In-situ estimation of ice crystal properties at the South Pole using LED calibration data from the IceCube Neutrino Observatory”. In: *The Cryosphere Discussions* 2022 (2022), pp. 1–48. DOI: 10.5194/tc-2022-174 (cited on pages 22, 43).

[91] R. Abbasi et al. “The IceCube data acquisition system: Signal capture, digitization, and timestamping”. In: *Nuclear Instruments and Methods in Physics Research Section A: Accelerators, Spectrometers, Detectors and Associated Equipment* 601.3 (2009), pp. 294–316. DOI: https://doi.org/10.1016/j.nima.2009.01.001 (cited on pages 22, 23, 46).

[92] M. G. Aartsen et al. “Energy Reconstruction Methods in the IceCube Neutrino Telescope”. In: *JINST* 9 (2014), P03009. DOI: 10.1088/1748-0221/9/03/P03009 (cited on pages 23, 49).

[93] J. Feintzeig. “Searches for Point-like Sources of Astrophysical Neutrinos with the IceCube Neutrino Observatory”. PhD thesis. University of Wisconsin, Madison, Jan. 2014 (cited on pages 23, 72, 75).

[94] N. Kulacz. “In Situ Measurement of the IceCube DOM Efficiency Factor Using Atmospheric Minimum Ionizing Muons”. MA thesis. University of Alberta, 2019 (cited on pages 23, 72, 75).

[95] R. Abbasi et al. “The design and performance of IceCube DeepCore”. In: *Astropart. Phys.* 35.10 (2012), pp. 615–624. DOI: 10.1016/j.astropartphys.2012.01.004 (cited on page 24).

[96] P. A. Cherenkov. “Visible Radiation Produced by Electrons Moving in a Medium with Velocities Exceeding that of Light”. In: *Phys. Rev.* 52 (4 Aug. 1937), pp. 378–379. DOI: 10.1103/PhysRev.52.378 (cited on page 25).

[97] V. F. Petrenko and R. W. Whitworth. “214Optical and electronic properties”. In: *Physics of Ice*. Oxford University Press, Jan. 2002. DOI: 10.1093/acprof:oso/9780198518945.003.0009 (cited on page 25).

[98] I. Frank and I. Tamm. “Coherent visible radiation from fast electrons passing through matter”. In: *C. R. Acad. Sci. USSR* 14 (1937), pp. 109–114 (cited on page 25).

[99] I. Tamm. "Radiation Emitted by Uniformly Moving Electrons". In: *Selected Papers*. Ed. by B. M. Bolotovskii, V. Y. Frenkel, and R. Peierls. Berlin, Heidelberg: Springer Berlin Heidelberg, 1991, pp. 37–53. DOI: 10.1007/978-3-642-74626-0_3 (cited on page 25).

[100] L. Rädel and C. Wiebusch. "Calculation of the Cherenkov light yield from low energetic secondary particles accompanying high-energy muons in ice and water with Geant4 simulations". In: *Astroparticle Physics* 38 (Oct. 2012), pp. 53–67. DOI: 10.1016/j.astropartphys.2012.09.008 (cited on pages 25, 35).

[101] D. Chirkin and W. Rhode. "Propagating leptons through matter with Muon Monte Carlo (MMC)". In: (July 2004) (cited on page 26).

[102] L. Raedel. "Simulation Studies of the Cherenkov Light Yield from Relativistic Particles in High-Energy Neutrino Telescopes with Geant4". MA thesis. Aachen, Germany: Rheinisch-Westfälischen Technischen Hochschule, 2012 (cited on pages 26, 27).

[103] E. Longo and I. Sestili. "Monte Carlo Calculation of Photon Initiated Electromagnetic Showers in Lead Glass". In: *Nucl. Instrum. Meth.* 128 (1975). [Erratum: Nucl.Instrum.Meth. 135, 587 (1976)], p. 283. DOI: 10.1016/0029-554X(75)90679-5 (cited on page 26).

[104] S. Agostinelli et al. "Geant4—a simulation toolkit". In: *Nucl. Instr. Meth. Phys. Res.* 506.3 (July 2003), pp. 250–303. DOI: 10.1016/s0168-9002(03)01368-8 (cited on pages 26, 35).

[105] T. Gabriel et al. "Energy dependence of hadronic activity". In: *Nuclear Instruments and Methods in Physics Research Section A: Accelerators, Spectrometers, Detectors and Associated Equipment* 338.2 (1994), pp. 336–347. DOI: https://doi.org/10.1016/0168-9002(94)91317-X (cited on page 27).

[106] L. Fischer. https://github.com/LeanderFischer/icetray_double_cascade_generator_functions (cited on page 31).

[107] R. Abbasi et al. "LeptonInjector and LeptonWeighter: A neutrino event generator and weighter for neutrino observatories". In: *Comput. Phys. Commun.* 266 (2021), p. 108018. DOI: 10.1016/j.cpc.2021.108018 (cited on page 34).

[108] https://launchpad.net/mg5amcnlo/3.0/3.3.x (cited on page 35).

[109] J.-H. Koehne et al. "PROPOSAL: A tool for propagation of charged leptons". In: *Computer Physics Communications* 184.9 (2013), pp. 2070–2090. DOI: https://doi.org/10.1016/j.cpc.2013.04.001 (cited on page 35).

[110] C. Argüelles. https://github.com/arguelles/NuXSSplMkr (cited on page 36).

[111] N. Whitehorn, J. van Santen, and S. Lafebre. "Penalized splines for smooth representation of high-dimensional Monte Carlo datasets". In: *Computer Physics Communications* 184.9 (2013), pp. 2214–2220. DOI: https://doi.org/10.1016/j.cpc.2013.04.008 (cited on pages 36, 49).

[112] J.-M. Levy. "Cross-section and polarization of neutrino-produced tau's made simple". In: *J. Phys. G* 36 (2009), p. 055002. DOI: 10.1088/0954-3899/36/5/055002 (cited on page 36).

[113] M. Glück, E. Reya, and A. Vogt. "Dynamical parton distributions revisited". In: *The European Physical Journal C* 5 (Sept. 1998), pp. 461–470. DOI: 10.1007/s100529800978 (cited on page 36).

[114] E. Tiesinga et al. "CODATA recommended values of the fundamental physical constants: 2018". In: *Rev. Mod. Phys.* 93 (2 July 2021), p. 025010. DOI: 10.1103/RevModPhys.93.025010 (cited on page 38).

[115] A. Alloul et al. "FeynRules 2.0 - A complete toolbox for tree-level phenomenology". In: *Comput. Phys. Commun.* 185 (2014), pp. 2250–2300. DOI: 10.1016/j.cpc.2014.04.012 (cited on page 39).

[116] C. Andreopoulos et al. "The GENIE Neutrino Monte Carlo Generator: Physics and User Manual". In: (2015) (cited on pages 41, 70).

[117] Y. Becherini et al. "A parameterisation of single and multiple muons in the deep water or ice". In: *Astroparticle Physics* 25.1 (2006), pp. 1–13. DOI: https://doi.org/10.1016/j.astropartphys.2005.10.005 (cited on page 42).

[118] D. Heck et al. "CORSIKA: A Monte Carlo code to simulate extensive air showers". In: (Feb. 1998) (cited on page 42).

[119] T. K. Gaisser. "Spectrum of cosmic-ray nucleons, kaon production, and the atmospheric muon charge ratio". In: *Astropart. Phys.* 35 (2012), pp. 801–806. DOI: 10.1016/j.astropartphys.2012.02.010 (cited on page 42).

[120] R. Engel et al. "The hadronic interaction model Sibyll – past, present and future". In: *EPJ Web Conf.* 145 (2017). Ed. by B. Pattison, p. 08001. DOI: 10.1051/epjconf/201614508001 (cited on page 42).

[121] C. Kopper et al. https://github.com/claudiok/clsim (cited on page 43).

[122] D. Chirkin et al. "Photon Propagation using GPUs by the IceCube Neutrino Observatory". In: *2019 15th International Conference on eScience (eScience)*. 2019, pp. 388–393. DOI: 10.1109/eScience.2019.00050 (cited on page 43).

[123] M. G. Aartsen et al. "Measurement of South Pole ice transparency with the IceCube LED calibration system". In: *Nucl. Instrum. Meth. A* 711 (2013), pp. 73–89. DOI: 10.1016/j.nima.2013.01.054 (cited on page 43).

[124] G. Mie. "Beiträge zur Optik trüber Medien, speziell kolloidaler Metallösungen". In: *Annalen der Physik* 330.3 (1908), pp. 377–445. DOI: https://doi.org/10.1002/andp.19083300302 (cited on page 43).

[125] L. G. Henyey and J. L. Greenstein. "Diffuse radiation in the Galaxy." In: *apj* 93 (Jan. 1941), pp. 70–83. DOI: 10.1086/144246 (cited on page 43).

[126] S. Fiedlschuster. "The Effect of Hole Ice on the Propagation and Detection of Light in IceCube". In: (Apr. 2019) (cited on page 44).

[127] M. G. Aartsen et al. "In-situ calibration of the single-photoelectron charge response of the IceCube photomultiplier tubes". In: *Journal of Instrumentation* 15.6 (June 2020), P06032. DOI: 10.1088/1748-0221/15/06/P06032 (cited on page 44).

[128] M. Larson. "Simulation and Identification of Non-Poissonian Noise Triggers in the IceCube Neutrino Detector". Available at https://ir.ua.edu/handle/123456789/1927. MA thesis. University of Alabama, Tuscaloosa, AL, USA, 2013 (cited on page 44).

[129] M. Larson. "A Search for Tau Neutrino Appearance with IceCube-DeepCore". available at https://discoverycenter.nbi.ku.dk/teaching/thesis_page/mjlarson_thesis.pdf. PhD thesis. University of Copenhagen, Denmark, 2018 (cited on page 44).

[130] M. G. Aartsen et al. "The IceCube Neutrino Observatory: Instrumentation and Online Systems". In: *JINST* 12.03 (2017), P03012. DOI: 10.1088/1748-0221/12/03/P03012 (cited on page 45).

[131] J. H. Friedman. "Stochastic gradient boosting". In: *Computational Statistics & Data Analysis* 38 (2002), pp. 367–378 (cited on page 47).

[132] R. Abbasi et al. "Measurement of atmospheric neutrino mixing with improved IceCube DeepCore calibration and data processing". In: *Phys. Rev. D* 108 (1 July 2023), p. 012014. DOI: 10.1103/PhysRevD.108.012014 (cited on pages 48, 69, 71).

[133] R. Abbasi et al. "Measurement of Astrophysical Tau Neutrinos in IceCube's High-Energy Starting Events". In: *arXiv e-prints* (Nov. 2020) (cited on page 49).

[134] P. Hallen. "On the Measurement of High-Energy Tau Neutrinos with IceCube". MA thesis. Aachen, Germany: RWTH Aachen University, 2013 (cited on page 49).

[135] M. Usner. "Search for Astrophysical Tau-Neutrinos in Six Years of High-Energy Starting Events in the IceCube Detector". PhD thesis. Berlin, Germany: Humboldt-Universität zu Berlin, Mathematisch-Naturwissenschaftliche Fakultät, 2018. DOI: 10.18452/19458 (cited on page 49).

[136] R. Abbasi et al. "Low energy event reconstruction in IceCube DeepCore". In: *Eur. Phys. J. C* 82.9 (2022), p. 807. DOI: 10.1140/epjc/s10052-022-10721-2 (cited on pages 50, 63).

[137] F. James and M. Roos. "Minuit: A System for Function Minimization and Analysis of the Parameter Errors and Correlations". In: *Comput. Phys. Commun.* 10 (1975), pp. 343–367. DOI: 10.1016/0010-4655(75)90039-9 (cited on pages 51, 76).

[138] F. Pedregosa et al. "Scikit-learn: Machine Learning in Python". In: *Journal of Machine Learning Research* 12 (2011), pp. 2825–2830 (cited on page 59).

[139] S. Yu and J. Micallef. "Recent neutrino oscillation result with the IceCube experiment". In: *38th International Cosmic Ray Conference*. July 2023 (cited on pages 60, 67, 75, 79).

[140] S. Yu and on behalf of the IceCube collaboration. "Direction reconstruction using a CNN for GeV-scale neutrinos in IceCube". In: *Journal of Instrumentation* 16.11 (Nov. 2021), p. C11001. DOI: 10.1088/1748-0221/16/11/C11001 (cited on pages 60, 61).

[141] J. Micallef. https://github.com/jessimic/LowEnergyNeuralNetwork (cited on page 60).

[142] M. Huennefeld. "Deep Learning in Physics exemplified by the Reconstruction of Muon-Neutrino Events in IceCube". In: *PoS* ICRC2017 (2017), p. 1057. DOI: 10.22323/1.301.1057 (cited on page 60).

[143] V. Barger et al. "Matter effects on three-neutrino oscillations". In: *Phys. Rev. D* 22 (11 Dec. 1980), pp. 2718–2726. DOI: 10.1103/PhysRevD.22.2718 (cited on page 65).

[144] A. M. Dziewonski and D. L. Anderson. "Preliminary reference Earth model". In: *Physics of the Earth and Planetary Interiors* 25.4 (1981), pp. 297–356. DOI: https://doi.org/10.1016/0031-9201(81)90046-7 (cited on page 65).

[145] H. Dembinski et al. "Data-driven model of the cosmic-ray flux and mass composition from 10 GeV to 10^{11} GeV". In: *PoS* ICRC2017 (2017), p. 533. DOI: 10.22323/1.301.0533 (cited on pages 69, 70).

[146] G. D. Barr et al. "Uncertainties in atmospheric neutrino fluxes". In: *Phys. Rev. D* 74 (9 Nov. 2006), p. 094009. DOI: 10.1103/PhysRevD.74.094009 (cited on page 69).

[147] J. Evans et al. "Uncertainties in atmospheric muon-neutrino fluxes arising from cosmic-ray primaries". In: *Phys. Rev. D* 95 (2 Jan. 2017), p. 023012. DOI: 10.1103/PhysRevD.95.023012 (cited on pages 69, 75).

[148] A. Fedynitch et al. https://github.com/afedynitch/MCEq (cited on page 69).

[149] G. D. Barr et al. "Uncertainties in Atmospheric Neutrino Fluxes". In: *Phys. Rev. D* 74 (2006), p. 094009. DOI: 10.1103/PhysRevD.74.094009 (cited on pages 70, 75).

[150] F. Riehn et al. "Hadronic interaction model sibyll 2.3d and extensive air showers". In: *Phys. Rev. D* 102 (6 Sept. 2020), p. 063002. DOI: 10.1103/PhysRevD.102.063002 (cited on page 70).

[151] Q. Wu et al. "A precise measurement of the muon neutrino–nucleon inclusive charged current cross section off an isoscalar target in the energy range 2.5<E<40 GeV by NOMAD". In: *Physics Letters B* 660.1 (2008), pp. 19–25. DOI: https://doi.org/10.1016/j.physletb.2007.12.027 (cited on page 71).

[152] M. M. Tzanov. "Precise measurement of neutrino and anti-neutrino differential cross sections on iron". PhD thesis. University of Pittsburgh, Pennsylvania, Jan. 2005 (cited on page 71).

[153] W. G. Seligman. "A next-to-leading-order QCD analysis of neutrino-iron structure functions at the Tevatron". PhD thesis. Columbia University, New York, Aug. 1997 (cited on page 71).

[154] A. Cooper-Sarkar, P. Mertsch, and S. Sarkar. "The high energy neutrino cross-section in the Standard Model and its uncertainty". In: *JHEP* 08 (2011), p. 042. DOI: 10.1007/JHEP08(2011)042 (cited on page 71).

[155] Rongen, Martin. "Measuring the optical properties of IceCube drill holes". In: *EPJ Web of Conferences* 116 (2016), p. 06011. DOI: 10.1051/epjconf/201611606011 (cited on page 72).

[156] R. Abbasi et al. "In situ estimation of ice crystal properties at the South Pole using LED calibration data from the IceCube Neutrino Observatory". In: *The Cryosphere* 18.1 (2024), pp. 75–102. DOI: 10.5194/tc-18-75-2024 (cited on pages 72, 78).

[157] L. Fischer, R. Naab, and A. Trettin. "Treating detector systematics via a likelihood free inference method". In: *Journal of Instrumentation* 18.10 (2023), P10019. DOI: 10.1088/1748-0221/18/10/P10019 (cited on page 73).

[158] E. Lohfink. "Testing nonstandard neutrino interaction parameters with IceCube-DeepCore". PhD thesis. Mainz, Germany: Johannes Gutenberg-Universität Mainz, Fachbereich für Physik, Mathematik und Informatik, 2023. DOI: http://doi.org/10.25358/openscience-9288 (cited on page 73).

[159] M. G. Aartsen et al. "Computational techniques for the analysis of small signals in high-statistics neutrino oscillation experiments". In: *Nucl. Instrum. Meth. A* 977 (2020), p. 164332. DOI: 10.1016/j.nima.2020.164332 (cited on page 75).

[160] https://github.com/icecube/pisa (cited on page 75).

[161] R. S. Nickerson. "Confirmation Bias: A Ubiquitous Phenomenon in Many Guises". In: *Review of General Psychology* 2 (1998), pp. 175–220 (cited on page 76).

[162] H. Dembinski et al. *scikit-hep/iminuit: v2.17.0*. Version v2.17.0. Sept. 2022. DOI: 10.5281/zenodo.7115916 (cited on page 76).

[163] S. S. Wilks. "The Large-Sample Distribution of the Likelihood Ratio for Testing Composite Hypotheses". In: *The Annals of Mathematical Statistics* 9.1 (1938), pp. 60–62. DOI: 10.1214/aoms/1177732360 (cited on page 79).